UNIVERSITÀ DEGLI STUDI DI NAPOLI FEDERICO II

INGEGNERIA STRUTTURALE, GEOTECNICA E RISCHIO SISMICO

Dottorato di ricerca

In

INGEGNERIA STRUTTURALE, GEOTECNICA E RISCHIO SISMICO

XXXII CICLO

Toward the Next Generation of the Earthquake Early Warning System

Sahar Nazeri

Relatore
Prof. Aldo Zollo

Correlatrice
Dott.ssa Simona Colombelli
Dott. Antonio Scala

Coordinatore
Prof. Luciano Rosati

Reviewers
Prof. Jean Virieux
Prof. Stefano Parolai

Acknowledgements

Graduating this PhD has been a frankly life-changing experience for me, and it would not have been possible to do without the guidance and support of many people.
First, I am pleased to express my sincere gratitude to my supervisor Prof. Aldo Zollo for the continuous supports and encouragements he gave me during my Ph.D. study and related research. His patience, motivation, constant feedback and immense knowledge are greatly appreciated. His guidance always assisted me during this research and in my master's thesis, as well. Apart from scientific view, he had a leading role in my life, I learned a lot from him.
I am extremely grateful to Prof. Maurizio Fedi who encouraged me to apply for Ph.D. program in Naples Federico II University. He supported me in various situations.
Many thanks to my advisors, Simona Colombelli and Antonio Scala who spent a lot of time to help me to progress my PhD thesis. Simona's precious advices for my master's thesis is also appreciated, surely her support improved the conclusion of the thesis.
Besides appreciation to Prof. Luciano Rosati as a coordinator, I wish to thank Prof. Jean Virieux and Stefano Parolai as the reviewers of this thesis, for their insightful comments, and deep questions which was incentive for me to widen my research from various perspectives.
I would like to thank the rest of my thesis committee: Dr. Matteo Picozzi, Prof. Gaetano Festa, Dr. Antonio Emolo and Dr. Guido Russo for their helps and encouragements.
I am also very grateful to Guido Celentano. He was always very kind and provided me with his assistance throughout any official and non-official problems I faced.
A very special thanks to Amir Ismail who was not only my friend but also like a member of my close family. Also, thanks to my friends, colleagues, and all RISSC-Lab members for making this period as a wonderful time to me; Ortensia Amoroso, Alessandro Caruso, Stefania Tarantino, Yuan Wang, Antonio Giovanni Iaccarino, Basak Bayraktar, Marcello Serra, Mariano Supino, Sergio Gammaldi, Grazia De Landro, Piero Brondi, Luca Elia, Rosario Riccio, Francesco Carotenuto and Sonia Sorrentino. In particular, I am grateful to Guido Maria Adinolfi for his close collaboration to finish ISCHIA project.
I would like to thank my family: my parents and my brothers. They always encourage me to follow my dreams.

Finally, a heartfelt appreciation to my husband, Jamaledin Baniamerian, for his continuously strong motivations and invaluable advice. He was always so supportive of my career and my life in general. Through our frequent discussions about the concerning issues, he helped me to progress in my research projects. He advised me in all steps of the thesis from beginning to end.

Contents

Introduction

Which kind of disasters can affect human life and how can science help to reduce the consequence of tragedy? Indeed, there is a range of challenges including technological or man-made hazards and natural hazards. Here in this thesis, one of the very critical natural hazards which has a major impact on human living *i.e.*, earthquake hazards, is investigated. Population growth and patterns of economic development are two important issues directly affected by an earthquake occurrence and induced impacts, leading to dramatic disaster situations.

The main aim of this thesis is to discuss how science can help to reduce the effect of the earthquake on human life. To human knowledge, precise earthquake prediction *i.e.*, specification of the time, location, and magnitude of future earthquakes are almost impossible. Moreover, earthquake prediction is sometimes distinguished from earthquake forecasting, which can be defined as the probabilistic assessment of general earthquake hazards, including the magnitude and frequency of damaging earthquakes in a given area over the years or decades. Both earthquake prediction and forecasting are also different from earthquake warning systems, in which the latter can provide a warning to neighboring regions that might be affected for an ongoing earthquake.

The Earthquake Early Warning (EEW) systems rapidly provide in-advanced warnings of impending strong ground motion in real-time as soon as detection of the ongoing earthquakes and before the impact of the ground vibrations. The initial part of the primary waves which is typically low-amplitude ground motion waveform *i.e.*, P-waves is normally used to estimate the potentially large-amplitude ground motion. Note that issuing and transmitting the alarms information using telecommunication is faster than seismic wave propagation speed, thus, the early warnings may arrive at a target site before the strong shaking itself, thereby providing invaluable time for both people and automated systems to take actions to mitigate earthquake-related injury and losses. These actions might range from complex automated procedures as stopping high-speed trains to simple procedures as warning people to get themselves to a safe location.

History of implementation of the first EEW system backs to 1991 (SASMEX) in Mexico City [*Espinosa-Aranda, et al*., 2009]. Nowadays, there is a significant improvement of EEW systems throughout the world which are operating in many parts of the world to provide warnings at high seismic hazard regions. Japan Meteorological Agency (JMA) and ShakeAlert EEW systems are two important examples developed in Japan and the west coast of the United States, respectively. In addition, EEW systems are being tested in other countries as Italy, Taiwan, Romania, China, South Korea, Turkey, and Switzerland.

EEW standard approaches estimate the location and magnitude of an earthquake, the key ingredients among the other parameters which are used in a ground motion prediction equation (GMPE) to calculate expected ground shaking. If the expected ground motion is greater than a manually specified threshold, the user is alerted. For instance, the JMA system provides alarms to subprefectures whenever ground motions are expected to exceed JMA intensity 4 within that subprefecture. The JMA system has released hundreds of alerts, including alerts sent to several million people during the 2011 M9.0 Tohoku earthquake [*Fujinawa and Noda*, 2013].

Although nowadays EEWS is one of the various important challenges in seismology and that a lot of scientific efforts have been done to develop it, there is still a long way to consider it as a consolidated technology. The physical theory behind EEWS is not fully clear and all parameters measured from early motion with rather non-negligible uncertainty are used to predict the final earthquake characteristics. The main assumption of most models, both the processes and algorithms, used in standard EEWS approaches and induced wave propagation are based on some simplifications to model the earthquake source and wave propagation. Standard approaches for the peak motion prediction in EEW methods are typically based on the point-source approximation and on simple empirical attenuation relationships, depending on the magnitude and hypocentral distance. On average, few portions of the P-waves, 3 seconds are used to the real-time computation of the event magnitude and location, which could be a problem for any estimation of large events in which have a complex rupture process over tens of seconds.

Several efforts are done in the last decade to measure a rupture during its early stages. Here in this thesis, we mainly focus on filling this gap, developing the algorithms to measure rupture characteristics and then consider the refined extended source to generate the shake map. Therefore, the thesis results can open a new research topic in real-time ground-shaking prediction for ongoing seismic events. All these concepts can be considered all together to issue the alarm and they will trigger “the next generation of

EEW systems”. In the framework of SERA infrastructure (Seismology and Earthquake Engineering Research Infrastructure Alliance for Europe, call INFRAIA-01-2016-2017), and JRA 6 (Joint Research Action, “Real-Time earthquake Shaking”), different methodologies are being developed and tested to generate evolutionary ground shaking maps by considering a rupture kinematic description and reliable finite-fault model.

In this regard, we have refined and tested various methodologies to retrieve the earthquake source. Same as the standard EEW approaches, the initial P-wave signals will be explored to identify the best proxies for the rapid source characterization (moment, length and duration). Updated kinematic rupture models (space-time slip function) are inferred by the consideration of progressively enlarged P-wave time windows as they are available at the network probes. The final output is the time-varying predicted-ground motion at the Earth surface at sites of interest in a recurrent manner.

For this purpose, we first, evaluate many possibilities and algorithms in the offline analysis of the initial P-wave signals. In particular, the time evolution of peak amplitude parameters will be used for the rapid prediction of the source magnitude and for estimating and then modeling the moment rate function.

These estimates are used to build simplified kinematic source models. The rupture speed and the rise time are selected accounting for the medium elastic properties and the event magnitude. A single patch slip distribution is imposed: its extension and position with respect to the nucleation are controlled by the moment estimates and by preliminary directivity estimates, respectively. The convolution of these models with pre-computed Green’s functions provides complete wavefield synthetic seismograms and thus early estimates of the expected amplitude vibrations (PGA/PGV) at the EEW target sites. The alert decision scheme is thus defined upon the exceedance of a user-compliant PGA/PGV threshold by the predicted synthetic values.

In addition, the inversion methodology will be implemented and tested on synthetic and real waveforms in off-line acquisition mode. A database of synthetic waveforms will be generated for a variety of case-studies (Ischia and Norcia earthquakes occurred in Italy). The off-line application will be checked, but the main objective is the development, the implementation and validation of efficient algorithms for the real-time signal processing, slip inversion and ground-shaking forecast that will improve the predictive performance of EEWS.

The structure of the thesis is based on four main chapters as follows: The first chapter, as an introduction, describes concepts of the earthquake early warning system from standard approaches to those expected in the next-generation tools. The second chapter illustrates the new model to compute the earthquake source characteristics. In the third chapter, using the source model resulted from the previous chapter, the evolutionary ground shaking prediction considering the Norcia event as a case study is evaluated. Finally, the last chapter is about calculating the source mechanism and rupture model from the inversion of a near-Source record.

CHAPTER 1

Introduction to Earthquake Early Warning System: from Standard Approaches to Next Generation Tools

1.1 Introduction and Main Concept of EEWS

Nowadays, the Earthquake Warning Systems (EWS) along with the Disaster Prevention Systems (DPS) play a significant role in the human life, by dramatically reducing the number of casualties and disasters; some examples are listed below. According to information released by the World Research Center (https://researchcentre.trtworld.com/) and European Commission (https://ec.europa.eu/jrc/en), among all various types of natural hazards, some of them including earthquakes, floods, storms, droughts, fires, heat wave, contagious diseases and landslides are considered as the high-risk events. Considering last 40 years; earthquake affects the highest number of people as the most recurrent and damaging natural hazards, while flood is the most frequent natural disaster (Atlas of the Human Planet, https://ec.europa.eu/jrc/en/publication/eur-scientific-and-technical-research-reports/atlas-human-planet-2017-global-exposure-natural-hazards).
Therefore, the necessity of designing such systems (*i.e.*, EWS and DPS) are fundamental to determine appropriate rapid response to the ongoing events toward contributing the risk mitigation.
Note that delivery of the effective and timely information of the ongoing event, like magnitude, location etc., is one of the main points to better design any kind of alert system and related rescue actions. Although the alert systems can be assigned for different hazards (see the examples listed in Table 1-1), in the present study we focus on earthquakes.
Generally, the earthquake warning systems, those related to manage the social actions, can be described in two main categories: Earthquake Early Warning System (EEWS) including One-site (or single station) and Regional (or network based) and Front detection (which is somehow a regional system based on a line). The front-detection systems are mainly used for those earthquakes located in the subduction zones or at far distance from the targets. For instance, the Mexican Seismic Alert System is a front-detection system which the active seismic region is approximately located 300 km far from the city center. In fact, before issuing the alarm to the impacted zones, there is enough time delay to determine the required parameters such as expected amplitude vibration, magnitude and location of the event enough far-distance. On the other hand, the second type of the earthquake alert systems, EEWS, (*i.e.*, both On-site and Regional) are following more rapid alternative strategies for earthquake risk mitigation, based on very short time scales (a few seconds to tens of seconds) *i.e.* the initial part of the P-waves. EEWS is under

development worldwide, using the real-time information about natural events that is provided by advanced monitoring infrastructures. However, the main conception of the EEWS refers to the optimal use of the few available data on the shortest possible time window to issue target warning several seconds before the arrivals of seismic waves (essentially surface waves) including damages in the target zone.

Table 1-1: Type of hazards and environmental threats [*UNEP*, 2012].

Type of Hazards	**Types of Environmental Threats**
1. Ongoing and rapid/sudden-onset threats	Oil spills, nuclear plant failures, and chemical plant accidents; geological hazards and hydro-meteorological hazards, except for droughts.
2. Slow-onset (or “creeping”) threats	deteriorating air and water quality, soil pollution, acid rain, climate change, droughts, ecosystems change, loss of biodiversity and habitats, land cover/land changes, nitrogen overloading, radioactive waste, coastal erosion, etc.
2.1 Location specific environmental threats	Ecosystem changes, urban growth, transboundary pollutants, loss of wetlands, etc.
2.2 New emerging science	Associated with biofuels, nanotechnology, carbon cycle, climate change, etc.
2.3 Contemporary environmental threats	Electronic waste, bottled water, etc.

In the last two decades, the EEWS have become one of the interesting topics for many seismologists around the world to reduce damage caused by earthquakes. Most of the recent EEWS must work out in few seconds after the earthquake rupture nucleation and before the impact of waves including devastating effect on population and buildings. Indeed, the EEWS represent the practical implementation of Real-Time (RT) Seismology concepts, methods and technologies. Note that a RT system is a protocol based on hardware devices controlled by software tools; it must react to an event before a well-defined deadline. The operational “deadline” of this system is related to the properties of the event being analyzed and characteristics of the recording system. For seismic warning monitoring, the “deadline” is defined based on different quantities such as the length of a data packet in seconds, the minimum trace length required to measure a certain parameter (location, magnitude) in tens/hundreds of seconds, the number of triggered stations and the impact zone among other parameters. On the other hand, in seismic monitoring three concepts are often employed to describe the time efficiency of a system, as they are listed below:

1. Real-Time: the rapid system to react to an event (earthquake) within a given deadline; for instance, the data packet < 1 sec

2. Near Real-Time: the system is fast, but no deadline is set (the system can accumulate delays in special or critical conditions).
3. Off-Line: no constrain is set on the response time of the system.

For the real-time seismic risk mitigation, a useful approach is the development of EEWS which are automatic, real-time information systems able to detect an ongoing earthquake and broad-casting a warning in a target area, before the arrival of the most destructive waves [*Nakamura*, 1984, 1988; *Heaton,* 1985; *Teng et al*., 1997; *Wu et al*., 1998; *Wu and Teng*, 2002; *Allen and Kanamori*, 2003].

1.2 EEWS Applications and Socio-Economic Aspects

If we divide the damage caused by a major earthquake into two categories, “primary” and “secondary”, the use of an EEWS in the potential areas with “secondary damage” is more important. The secondary consequences of the earthquakes occur when ground shakings have other effects in addition to initial casualties, such as landslides, tsunamis, flooding, fire and radioactive material leakage into the environment. For example, some targets like nuclear power plants and oil/gas refineries are more potential places to face the secondary damage. Indeed, in these targets the effect of the earthquakes is not only damaging the buildings and human casualties, but also the leakage of radioactive materials, oil and gas into the environment. Table 1-2 presents some examples of installation of the EEWS in the high potential sites corresponding to the secondary damages in different parts of Europe. Other important targets to install EEWS can be listed as: airports, rail transport systems, especially high-speed trains, hospitals, schools, large factories, highways, bridges and so on.

In the following, the dangerous role of secondary effects is further explained by pointing out of some examples. The first example refers to the disaster that occurred in San Francisco, the United States, in 1906, a massive earthquake with magnitude about 7.8. After the earthquake, there was a huge fire that destroyed more than a quarter of the San Francisco; the earthquake with magnitude 9.0 occurred in 2011 in Japan, the fourth most powerful earthquake in the world since modern record-keeping began in 1900. This event denoted by "Great East Japan Earthquake" is the nuclear crisis caused by the collapse of Fukushima nuclear reactors and related cooling swimming pools and the leakage of radioactive materials into the environment. Most experts mention the Fukushima nuclear disaster as the largest nuclear disaster after the Chernobyl Ukraine disaster [1986].

Moreover, to better understand the necessity of the installation of the EEWS, along with paying attention to the casualties and disasters in a region, it is also very important to have the economic damage statistics. For instance, Manjil-Rudbar (1990) and Bam (2003) earthquakes, the deadliest earthquakes in the recent decades occurred in Iran, have killed nearly 70,000 people in total. The World Bank estimates the corresponding damage of only the Bam earthquake about $1.3 Billion. Unfortunately, Arg-e Bam, the largest adobe building in the world and the World Heritage Site as listed by UNESCO, completely was destroyed after 2003 earthquake.

Table 1-2: Examples of EEWS in different parts of Europe, [*Zollo, Seismology Short-Course*, 2018].

Application	Sites	Status
Nuclear power plant	Switzerland	Implementation
Different industries	Prtegese	Feasibility test
Rail transport systems	South Italy	Feasibility test
Schools	South Italy	Implementation
Oil/gas refineries	Turkey, Istanbul	Implementation
Hospitals	Greece	Implementation
National Seismic Network	Island, Italy	Feasibility test

Furthermore, latest information released by the United States [*Strauss and Allen*, 2016] provides an excellent overview of the significant costs and benefits of an EEWS from the economic point of view. According to this report, the United States spends about $16.1 million per year (one-time costs of installation is also reported about $38 million) to maintain the public warning system for the West Coast of the United States. *Strauss and Allen* [2016], mentioned that by considering all loss estimations, spending this amount of money is negligible. For instance, the loss quantity of M 7 earthquake on the Hayward fault, only the residential and building replacement value, is around $50 billion (*Charles Scawthorn*, after Fires and the Hayward Earthquake Workshop, written communication, October 2014).

1.3 Network- and Station-based EEW Systems

In general, EEWS can be classified into two approaches as “Regional” (or network-based), and “On-site” (or a single station-based) [*Nakamora*, 1988; *Caruso et al*, 2017]. A regional EEWS is a network-based system integrating a dense seismic array deployed around the earthquake source zone. In this approach, the contents of the first few seconds of the P-waves are used to determine magnitude and hypocenter of an earthquake. Certainly, a dense network provides more reliable estimations by integrating different measurements. When a seismic event is detected, a regional system issues an alert for a wide epicentral area. The alert is generally based upon the rapid estimation of the earthquake location and magnitude and previously known ground motion prediction equations (GMPEs) [*e.g.*, *Allen et al*., 2009; *Satriano et al*., 2011, among others], although there are a few regional and/or multiple-station EEW algorithms that predict the ground motion level at target sites bypassing the source parameter estimation [*Hoshiba*, 2013; *Hoshiba and Aoki*, 2015]. The close region to the source area, where the alert cannot be made available before the arrival of the dangerous seismic waves, is called the blind zone, a relative concept depending on RT system. *Stankiewicz et al*., [2015] present that to have a more precise EEW system for events less than 60 km from the target, there should be a combination of both regional and onsite systems.

Conversely, an on-site EEW is a stand-alone system based on a single sensor (or a small array of sensors) located in the proximity of the target to secure. In this configuration, the early P wave amplitudes and/or the characteristic frequency are used to predict the strong shaking associated with the late S and surface wave arrivals at the same site. This approach is particularly useful for sites located within the blind zone of a regional EEW system, allowing for a usable warning before the arrival of strong shaking waves. The P wave-based, on-site approaches use previously determined empirical relations to estimate the maximum ground-shaking amplitude, through the measurement of P-wave amplitude, frequency, integral of squared velocity, and other related quantities [*Kanamori*, 2005; *Wu and Kanamori*, 2008; *Böse et al*., 2009; *Zollo et al*., 2010; *Picozzi*, 2012; *Colombelli et al*., 2015; *Brondi et al.,* 2015].

On the other hand, the maximum ground shaking can be predicted using the initial part of the P-phase amplitude and/or frequency content of each seismic station in on-site method. Thus, precise determination of the magnitude and hypocenter are not needed in an onsite application. In addition to these two main methods, a combination of these approaches is also available in the EEWS [*e.g., Picozzi et al*., 2015].

On-site systems are generally less accurate, in estimating the source parameters when compared to a multiple-station approach (single-station versus multiple-station) [*Zollo et al*., 2014]. But on-site approaches can bypass both the uncertain estimates of source parameters (*e.g.*, earthquake location and magnitude) and the typically large uncertainty in the prediction of the ground-shaking level from regional GMPEs [*Caruso et al.*, 2017]. Another important parameter in EEWS, is the lead time (LT), *i.e.*, the time available for a mitigation action after the alarm which its definition differs for two types of EEW systems (Figure 1-1). In the network-based approach, LT is time difference between the first S-wave arrived at the target and the first P-wave recorded at the network, and it increases with the distance from the source (Figure 1-1). While in the on-site based systems, it is defined by time difference between the first S-wave and P-wave arrived at the target, and it increases with smaller distance comparing that one for the network based EWS (Figure 1-1).

1.4 Basic Methodologies and Output Parameters of an EEWS

1.4.1 P-wave Picking Strategies

In EEWS standard approaches, the automatic phase-picking is the first and a very important step which is also used in the next steps *i.e.*, determination of the location and estimation of the magnitude [*Kanamori*, 2005; *Zollo et al*., 2006; *Satriano et al.*, 2008]. In general, the automatic phase picking algorithms are based on comparing the energy level, frequency content, or any other signal characteristics with respect to the background noise [*Lomax et al*., 2012]. The main objective of all these algorithms is based on reducing the noise or amplifying the signals in the specific frequency bands. For example, one of the standard approaches for automatic phase picking is based on comparing the energy level of the Short-Term Averages (STA) and Long-Term Averages (LTA) of a Characteristic Function (CF) denoted by STA/LTA algorithms.
However, the optimized P-wave picking algorithm implemented in the EEWS is FilterPicker [*Lomax et al*., 2012]. Five configuration parameters control the long- and short-time windows on which a CF is evaluated. Among the configuration parameters, the most relevant are the thresholds for CF picking declaration and the minimum time window after a trigger where the CF must exceed these thresholds, which allows to ignore spikes and glitches of short duration (see *Lomax et al*., [2012] for further details). When a single sensor is used, indeed, the risk for a wrong P-wave detection due to spurious, transient signals (*e.g*. from anthropic sources) is relatively high. Therefore, in order to

avoid the declaration of too many false alarms, the automatic picking algorithm can be configured to be less sensible to spurious transient signals and different criteria to filter and rule-out low-quality data have been implemented.

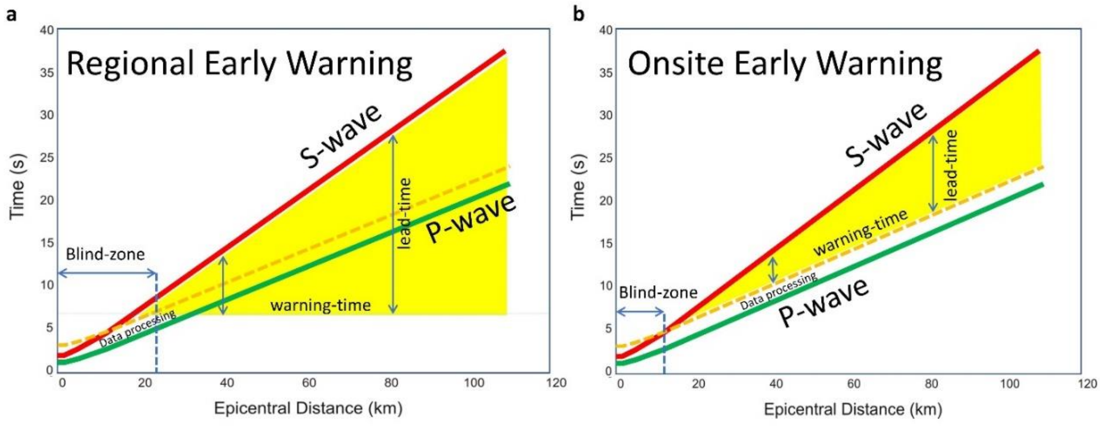

Figure 1-1: Warning- and Lead-time for **a.** network-based **b.** on-site systems. [*Zollo, Seismology Short-Course*, 2018].

The proper setting of FilterPicker parameters is extremely relevant for the onsite early-warning system in order to avoid the issuance of false alarms. The selection of the picker parameters not only depends on the noise level at the site, but also on the magnitude and distance ranges of the expected events, which determine the minimum ground motion level to be detected for the warning declaration.

Box 1-1: The nature of the earthquake rupture

Understanding the earthquake rupture plays a fundamental role in understanding the fault structure and earthquake hazards. One of the most common hypotheses to describe the rupture is the cascade model which is a sequential-development model, in which energy dissipates in the form of a continuous flow. Based on the cascade model, the earthquake magnitude is dependent on the state of stress across the fault plane. In the cascade model, faults are divided into patches of varying size and shape. When an earthquake initiates on one patch, slip on this patch can lead to extend slip on the adjacent patches if the rupture energy and the state of stress on adjacent patches are favorable. An earthquake continues spreading from patch to patch until there is insufficient energy to rupture the next patch at which point the rupture stops. Given this framework, the initial rupture behavior of large and small earthquakes is similar, and it is consequently not possible to estimate the magnitude of an earthquake until the rupture has stopped.

Throughout the last decade the seismological community has debated whether the first few seconds of the P-wave (the first few seconds of radiated energy) provides information about the final magnitude of an earthquake before the rupture is complete [*Ohnaka*, 2000; *Ellsworth and Beroza,* 1995; *Kilb and Gomberg*, 1994; *Steacy and McCloskey*, 1998]. Much of the debate has focused on the time-domain characteristics of the P-wave. However, evidence for a scaling relation between the frequency content of the first few seconds of the P-wave and the final magnitude has also emerged.

However, simultaneous with evolving the EEWS, some basic rupture models such as the fault cascade model have been faced a major challenge. First, *Nakamura* [1988] stated that the magnitude of the earthquake is positively correlated with some of the parameters associated with the initial part of the rupture. Note that in earthquakes with magnitudes less than 6.0, the total rupture time is about 4 seconds. Therefore, all the features of the released energy can be extracted from the first 4 seconds of the signal. Also, investigating different EEWS parameters have demonstrated that earthquakes larger than 6.0 are also associated with various parameters in this short period of time, when failure is not completed.

Therefore, other conceptual models where the structure of the total stress field in the seismic zone would impact the shaping of the P wave emission can be put forward and could be considered as alternatives to the cascade concept.

1.4.2 Earthquake Location

Within the first few seconds after the P-wave onset, an EEWS issues the preliminary location (*i.e.*, epicentral distance, depth and origin time of the event) of the triggered event. Indeed, depending on the source-to-site distance, only a significant time about few seconds is available before arriving the destructive waves. Thus, using the optimized method to locate an earthquake is a very critical part of a standard EEWS towards decreasing the fault and missed alarms [*Iervolino et al.*, 2006]. Mathematically, the earthquake location problem is solved considering the ray-path theory and the linear or non-linear equations, one for each station. Furthermore, the standard approaches to locate the earthquake are not valid to use in real-time methodologies which should be evolutionary, independent of origin time and highly robust in presence of outlier data

Therefore, among all possible methods and techniques to locate the earthquake, a nonlinear probabilistic approach is implemented in EEWS that the basic concept is based on the Equal Differential Time (EDT) formulation [*Font et al.*, 2004; *Lomax*, 2005]. In this evolutionary and probabilistic algorithm, after recording the earthquake at the first station, both preliminary location and 3D probability density function are determined. In fact, as soon as the first station is activated, the location of the earthquake is largely determined, then by triggering the other stations, the approximate location smoothly converges to the real location. Considering the dense network (*e.g*. 10 km average of intermediate station-distance), the time required to locate an earthquake is about one to three seconds after the earthquake detection [*Satriano et al*., 2008]. Moreover, for a sparse seismic network (such as the Greece network with 100 km station distance), a further simulation with a Mw 6:7 southern Greece earthquake shows that at a regional scale, the real-time location can provide useful constraints on the earthquake position several seconds [*Satriano et al*., 2008]. It is also worth to note that in this algorithm, locating the earthquake is completely independent of the origin time of the earthquake and the unknowns are only longitude, latitude and depth of the earthquake. In addition, this method is much more robust in the presence of outliers [*Lomax*, 2005] which will be more significant when only few amounts of data are available.

1.4.3 Magnitude Estimation

Till 1900, precise information of earthquake properties such as size and intensity were not available. Size of an event was only evaluated based on the field observations such as the number of casualties and damages for instance. Earthquake magnitude is a relevant measurement of an earthquake describing the size and differs from energy release or shaking intensity. For example, the shaking intensity of the event varies with distance, while the magnitude is always constant and only dependent on the amount of released energy in the source.

In general, magnitude is expressed using the logarithm of the measured peak amplitude on a seismogram, in different part of the waveforms due to the definition of various scales. And it is well-known that amplitude content of the waveforms is attenuating by different factors such as increasing the hypocenteral distance and geometric expansion of the waves.

The general equation to compute the earthquake magnitude is obtained from the following formula, $M=\log(A/T)+f(h,\Delta)+C$, where A is displacement peak amplitude, T is dominant period, f indicates the correction term as a function of depth (h) and epicentral distance

(Δ), and C is constant coefficient related to the given area. Local magnitude (ML), energy magnitude or moment magnitude (Mw), body-wave magnitude (mb or mB) and Surface-wave magnitude (Ms) are some scales used in different agencies to report the earthquake size.

Undoubtedly, in EEWS standard approaches, one of the critical issues is estimating the magnitude of the event. In the developed algorithms, the information about the frequency or amplitude content of the early part of the P-waves is mainly used to estimate the magnitude of an earthquake [*Allen and Kanamori*, 2003; *Wu and Zhao*, 2006; *Zollo et al*., 2010]. The most common methods for the estimation of the frequency content of the P-wave are usually based on the predominant period parameter τ_p [*Allen and Kanamori*, 2003], the characteristic period τ_c [*Kanamori*, 2005], and log-average period τ_{log} [*Ziv*, 2014]. Moreover, the maximum peak of the displacement (Pd), velocity (Pv), or acceleration (Pa) in the first few seconds of the P-waves have been shown to be empirically related to the earthquake magnitude and thus can be used for early warning purposes [*Wu and Kanamori*, 2005; *Zollo et al*., 2006; *Melgar et al*., 2015]. Selecting a unique and stable method for estimating the earthquake magnitude in EEWS is, however, a challenging issue. Each method has its own sensitivity that depends on various factors, including the characteristics of different earthquake datasets and the background noise of the recorded waveforms. Recently integrated frequency- and amplitude-based parameters are introduced to improve the accuracy of the magnitude and potential damage estimate [*Kanamori*, 2005; *Wurman et al*., 2007; *Zollo et al*., 2010]. Although some approaches are based on a combination of τ_c and Pd [*Kanamori*, 2005; *Zollo et al*., 2010, 2012; *Böse et al*., 2012], other approaches make use of both τ_P^{max} and Pd [*Wurman et al*., 2007; *Kuyuk and Allen*, 2013].

In the following sections, we present a brief description of all EEWS parameters used in estimating the magnitude. In Appendix A, we investigate different frequency- and amplitude-based parameters from earthquakes occurring around the metropolis of Tehran using vertical seismic records of the Iranian Seismological Center (IRSC).

1.4.3.1 EEWS Frequency-based Parameters

To estimate the earthquake magnitude, the methods based on frequency contents mainly refer to the calculation of some parameters such as Predominant Period, τ_p^{max}, Characteristic Period, τ_c and the Log-Average Period, τ_{log} [*Nazeri et al*., 2017].

Predominant Period, τ_p^{max}

As mentioned before, first *Nakamura* [1998] observed that the magnitude of an earthquake can be estimated using the "predominant period" parameter calculated in the first few seconds of the P wave. The predominant period parameter is computed using:

$$\tau_i^p = 2\pi\sqrt{V_i/D_i} \tag{1-1}$$

$$V_i = \alpha V_{i-1} + v_i^2 \quad , \quad D_i = \alpha D_{i-1} + \dot{v}_i^2 \tag{1-2}$$

where v_i is the value of the velocity signal at time i, V_i the velocity squared signal, D_i the velocity derivative squared, and α is a smoothing coefficient. *Allen and Kanamori* [2003], proposed a modified version of the predominant period, [*Nakamura*, 1988], and considered its maximum value in 2 to 4 s after the P-wave onset. Although *Wolfe* [2006] introduced the average of the predominant period, τ_p, in a window around the initial P-wave, in EEWS the maximum of this parameter is usually preferred [*Lockman and Allen*, 2007].

Lockman and Allen [2007] observed that τ_p immediately after the P-wave onset has an artifact behavior, *i.e.* it oscillates for about 1 to 2 seconds. Thus, to improve the magnitude estimate using τ_p, they suggested a transient zone after the P-wave onset for calculation of τ_p^{max}. Different duration of the transient zone was reported in literature, *e.g.* 0.05 s [*Olson and Allen,* 2005], 0.5 s [*Lockman and Allen,* 2007*; Ziv,* 2014] and 2.0 s [*Lockman and Allen,* 2007]. The transient zone is proportional to the oscillatory nature of τ_p after the P-wave onset. Selecting an appropriate transient zone usually depends on the region and frequency content of data [*Lockman and Allen,* 2007].

Another main issue refers to choose the proper type of filter. Most of the filters used to calculate τ_p^{max} are generally low-pass Butterworth filters with different corner frequencies depending on the geographical area. For example, *Olson and Allen* [2005] used a frequency of 3.0 Hz to evaluate data from Japan, Taiwan, California, and Alaska, whereas *Allen and Lockman* [2007] conclude that the corner frequency of the low-pass filter depends also on the magnitude of the event. Their results show that the proper corner frequency for earthquakes with M <5 is about 10.0 Hz, while a 3.0 Hz would be appropriate for events with M> 4.5.

Characteristic Period, τ_c

Kanamori [2005] developed a different period parameter, τ_c, which is expressed by velocity and displacement records. Note that τ_c is produces a single measure point for the entire analyzed window due to the integration involved in the process. This parameter is calculated as:

$$\tau_c = 2\pi \sqrt{\frac{\int_0^{\tau_0} u^2\, dt}{\int_0^{\tau_0} v^2\, dt}} \tag{1-3}$$

where u and v are velocity and displacement signals respectively. τ_0 is the time window after the P wave onset which is usually set as 3 seconds in standard approaches. The proper filter to obtain this parameter is also high-pass Butterworth filter with corner frequency about 0.075 Hz.

Log-Average Period, τ_{log}

Recently *Ziv* [2014] introduced a new frequency-based parameter, *e.g.* the log-average period, τ_{log}. While τ_p^{max} and τ_c are calculated in the time domain, τ_{log} is calculated from the Fourier spectrum of the velocity seismograms in the frequency domain. First, the Fourier spectrum is calculated after applying a Hanning window in a 3 s time window after P-wave onset. Then amplitude spectrum is resampled between the frequencies from 0.1 and 10 Hz with an interval equal to 0.1 log unit of frequency. The relevant equation to calculate this parameter is expressed as:

$$\log(\tau_{log}) = \frac{\sum_i P_i^*(w_i) \log\left(\frac{1}{w_i}\right)}{\sum_i P_i^*(w_i)} \tag{1-4}$$

where τ_{log} is in second and $P_i^*(w_i)$ presents the new coefficients of Fourier spectrum in first few seconds after the P-wave.

1.4.3.2 EEWS Amplitude-based Parameters

Peak Displacement, P_d

Wu and Kanamori [2005] found that the peak amplitude of the initial part of the displacement signal (Pd) in a given time-window (usually equals to 3 seconds) has a linear relationship with the Peak Ground Velocity (PGV) value. PGV equals to the maximum value of ground velocity at a given site during a particular earthquake. As PGV is a very important parameter in seismic hazard analysis, the Pd value can be proposed as an proxy

parameter to the PGV in EEWS to reduce significantly the time required to computation part. However, their conclusion has been confirmed by other literatures [*Wu et al*., 2007; *Zollo et al*., 2010] and it has not been refused up to now. In addition to the risk analysis issue, the Pd parameter is widely used to calculate the earthquake magnitude using an attenuation relationship. Since the relevant time window to compute Pd is few seconds after P-wave, precise determination of the P phase is one of the key steps (Figure 1-2).
The next important and basic step to calculate Pd is computing the displacement signal by integrating the input data which is usually acceleration or velocity waveforms. Also, a casual 0.075 Hz high pass Butterworth filter was applied to remove the low frequencies after integrating to the displacement records.
Then we can calculate the earthquake magnitude (M) according to the following empirical attenuation relationship in terms of hypocentral distance (R) in km and parameter Pd in cm. It is also worth noting that in calculating the Pd parameter, the first 3.0 seconds of the P wave is considered.

$$\log P_d = A\,M_w + B\,\log R + C \quad (1\text{-}5)$$

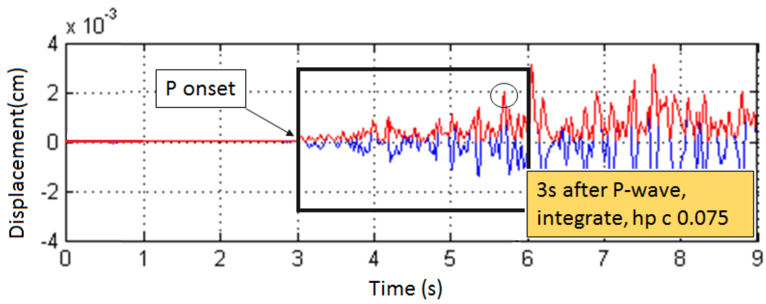

Figure 1-2: Pd value. figure shows the displacement waveform (the blue signal) in cm and how peak amplitude of initial part after the P-wave onset is computed. The red signal represents the absolute displacement signal which is used to measure the peak.

As it is mentioned, in this formula, R is the hypocentral distance in km, that can be estimated using the known B/C-Δ method implemented in Japanese EEWS without necessity of determination of the earthquake location [*Yamamoto et al*., 2012; *Nazeri and Shomali*, 2019]. The unknown coefficients A, B and C are estimated by the least square multi-regression analysis. This equation shows that Pd is a function of both magnitude and distance which is decreasing with increasing distance and increasing with increasing the magnitude (Figure 1-3).
Zollo et al., [2006] suggest that P_d can be also normalized to a reference distance to correct the attenuation relationship to be independent to distance. To this purpose, a reference

distance can be considered any meaningful parameter, for example an average depth of the events which is equal to 10 km for Italy region.

$$\log\left(\mathrm{Pd}^{10\mathrm{km}}\right) = \log\left(\mathrm{Pd}^{\mathrm{R}}\right) - \mathrm{C}\log\left(\frac{\mathrm{R}}{10}\right) \tag{1-6}$$

where C is estimated by the least square regression analysis. So, magnitude is expressed by normalized Pd:

$$\log\left(\mathrm{Pd}^{10\mathrm{km}}\right) = A' + \mathrm{B}'\mathrm{M} \tag{1-7}$$

And finally considering both equations:

$$\log(Pd) = AM + B\log(R/10) + C \tag{1-8}$$

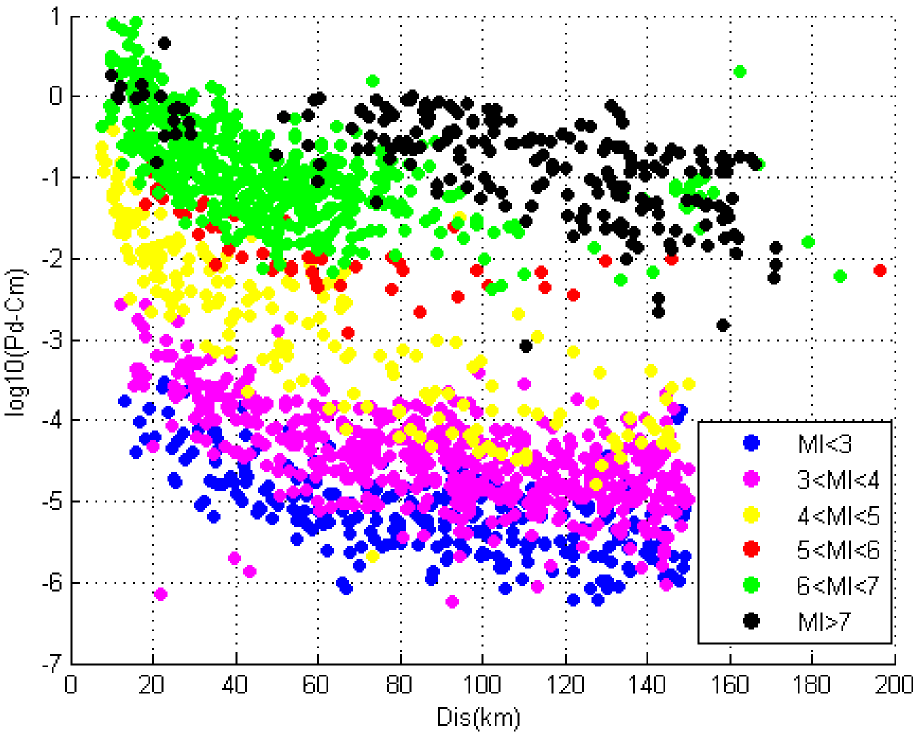

Figure 1-3: logarithm of Pd parameter in cm versus distance in km. Colors refer to range of magnitude.

1.5 EEWS: Worldwide and in Southern Italy

Along with implementation and use of EEWS as an effective risk reduction strategy in high seismic hazard countries in the world *e.g.* Japan, USA, Mexico, and Taiwan, in Europe, the development and testing of EEWS is also being experimented in several active seismic regions mostly along the Mediterranean region. Most of the projects are financially supported by EU through several collaborative projects (*e.g.* SAFER, REAKT). Certainly, one of the pioneer countries in Europe in the early warning topics is Italy. The seismological research group, RISSC-Lab, at the University of Naples Federico II developed an integrated PRobabilistic and Evolutionary early warning SysTem (PRESTo) that continuously processes the streams of acceleration or velocity from seismic stations [*Zollo et al*., 2009]. In addition to PRESTo, there are also two more systems *i.e.*, on-site (Station-based, SAVE) and quake up which is the new version of PRESTo. In the following sections, different early warning systems developed in southern Italy are explained in detail.

1.5.1 Network-based System (PRESTo)

PRESTo (PRobabilistic and Evolutionary early warning SysTem) is a software platform (Figure 1-4) for the regional (Network-based system) earthquake early warning that integrates the developed algorithms for real-time earthquake location and magnitude estimation into a highly configurable and easily portable package [*Zollo et al.*, 2009; *Satriano et al.*, 2011]. This software is in testing phase on the the Irpinia Seismic Network (ISNet) deployed in Southern Apennines along the active fault system responsible for the 1980, November 23, Ms 6.9 Campania-Lucania earthquake.

In fact, ISNet implements a prototype system for earthquake early-warning and alert management in southern Italy. Moreover, PRESTo has been implemented in different places and seismic networks *e.g*., at the Korean Institute of Geoscience and Mineral Resources, in South Korea; at the National Institute of Research and Development for Earth Physics, in Romania; and at the Istituto Nazionale di Oceanografia e di Geofisica Sperimentale, in Italy [*Picozzi et al*., 2015].

Picozzi et al., [2015] has also investigated a feasibility study for a nationwide EEWS in Italy using EEWS platform Presto and the Italian strong motion network (RAN), owned and managed by the Italian Department of Civil Protection (DPC) [*Gorini et al.*, 2010]. Their observations show that despite the high RAN's station density, a regional EEW approach for Italy may not provide timely warnings within a distance of about 25 km to 30 km from the epicenters. This observation, due to the closeness in Italy of seismogenetic faults and populated cities, was the strong motivations to conceive, develop and propose an on-site approach to EEW.

Estimating the magnitude and location of earthquakes and calculating the ground motion at the targets makes the PRESTo a very practical and usable computer package. Phase picking in PRESTo is initiated once at least two stations trigger an energetic even. PRESTo applies an optimized phase detector and picker algorithm for real-time seismic monitoring and EEWS in its regional setting [*Lomax et al.*, 2012]. An event is located using non-linear location [*Satriano et al.,* 2008] when more than 6 stations trigger the event. PRESTo reports the initial location, magnitude and ground motions in the target positions in incremental way. The estimate of magnitude by PRESTo is done based on the Bayesian formulation which is defined according to measurement of displacement and estimating the conditional probability density function (PDF) of magnitude.

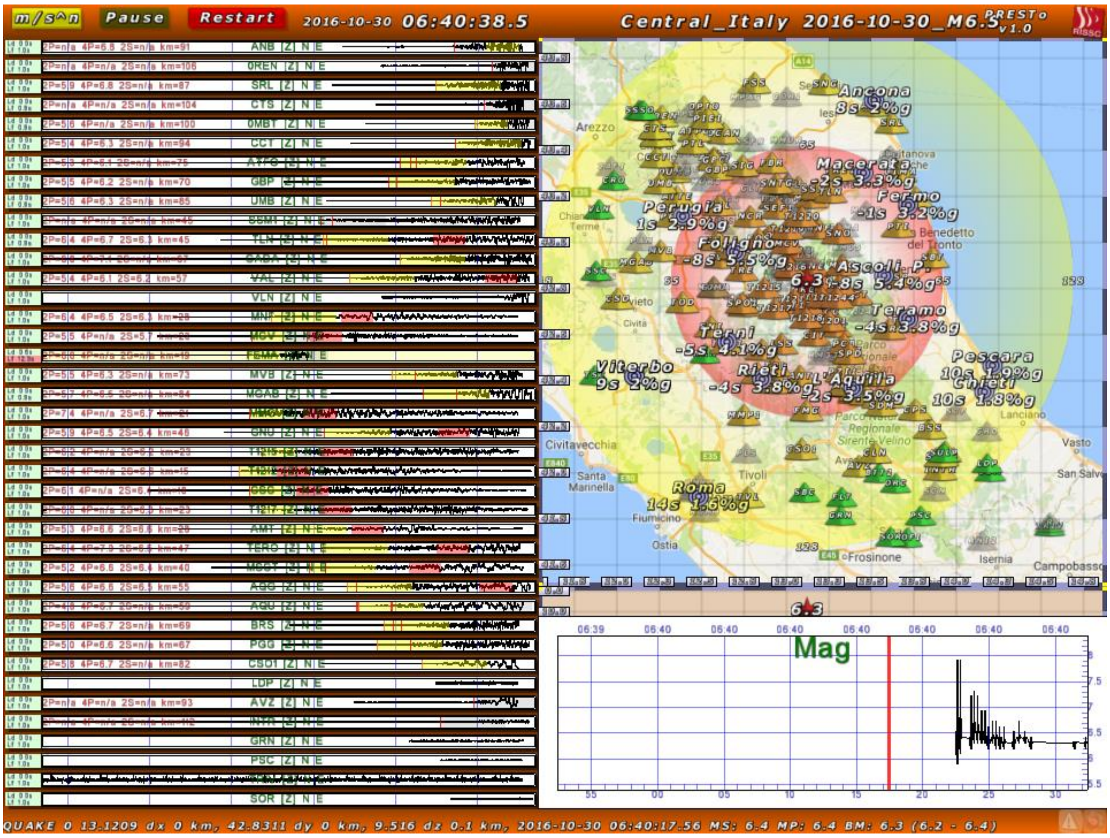

Figure 1-4: Snapshot of running PRESTo during the playback of the Norcia earthquake [RISSC-Lab].

1.5.2 Single Station-based System, One-site (SAVE)

Another EEWS software platform developed by RISSC-Lab is a station-based system denoted as SAVE (Figure 1-5), Onsite Alert Level, [*Colombelli et al.*, 2015; *Caruso et al.*, 2017]. SAVE processes the vertical component of both accelerometers and (broad band) velocimeters. Based on the real-time measurement of the initial Pd and the average period, τ_c, over time windows of 1, 2 and 3 seconds after the P-phase arrival, SAVE predicts the expected ground shaking at the recording site, issues a local alert level and a qualitative assessment about the earthquake magnitude and the source to-site distance. As soon as a detected signal exceeds some user-configurable thresholds of the output parameters (*e.g*. predicted intensity IV or above), SAVE delivers a warning message both via internet (via UDP) and a visual display, while providing a readable summary of the outputs of the system, which is also sent to remote users by mail.

Caruso et al., [2017] evaluate the performance of the SAVE, using a database of earthquakes occurred during the last 10 years in Italy and recorded by the RAN network (made freely available by the ITalian ACcelerometric Archive, ITACA 2.0, http://itaca.mi.ingv.it/ItacaNet;) [*Luzi et al.*, 2008; *Pacor et al.*, 2011].

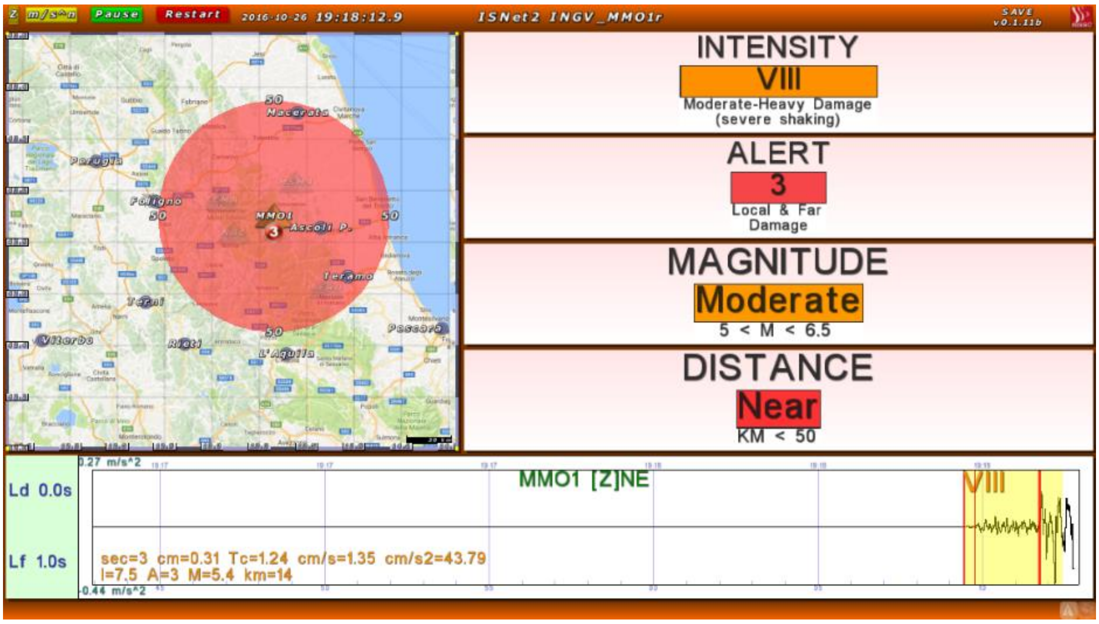

Figure 1-5: Snapshot of running SAVE during the playback of the Norcia earthquake [RISSC-Lab].

The on-site system SAVE processes the vertical ground motion component from one or more co-located sensors at a recording site. Both acceleration and (broad band) velocity probes are supported. The waveforms can be streamed in real-time from the data loggers or played-back from past events in off-line mode. In the real-time mode, SAVE supports the SeedLink protocol for data streaming, which has been chosen because it is commonly implemented in data-loggers or available through the installation of the *SeisComP* server for data collection [*SeisComP*, 2016].

Same as Presto, the P-wave picking algorithm implemented in SAVE is *FilterPicker* [*Lomax et al*., 2012], which is optimized for earthquake early warning, as it already operates on data packets of variable lengths and it can declare a pick (P-wave arrival time) within few samples from the trigger. When a single sensor is used, indeed, the risk for a wrong P-wave detection due to spurious, transient signals (*e.g*. from anthropic sources) is relatively high. Therefore, in order to avoid the declaration of too many false alarms, the automatic picking algorithm can be configured to be less sensible to spurious transient signals and different criteria to filter and rule-out low-quality data have been implemented. The proper setting of FilterPicker parameters is extremely relevant for the onsite early-warning system in order to avoid the issuance of false alarms. The selection of the picker parameters mainly depends on the noise level at the site, but also on the magnitude and distance ranges of the expected events, which determine the minimum ground motion level to be detected for the warning declaration.

Considering the uncertainties associated to each estimated parameter, SAVE does not provide all the punctual output values, but it rather provides output parameters through a simplified classification scheme. The Instrumental Intensity (I_{MM}) is derived by the conversion of Peak Ground Velocity (PGV) using the scale proposed by *Faenza and Michelini* [2010] and is classified in three class of perceived shaking: *Light* (if the intensity predicted is < III), *moderate* (if the intensity predicted is in the range IV-V) and *strong* (if the intensity predicted is upper than V) [*Caruso et al.*, 2017].

1.5.3 Application of PRESTo and SAVE to the 2016 Mw 6.2, Amatrice earthquake

In this section, the performance of two discussed software *i.e.*, network-based (PRESTo) and the onsite (SAVE) is evaluated considering the 2016, August 24 Amatrice earthquake occurred in the central Italy as a case study. Both on-line and off-line applications are implemented into the seismic waveforms recorded by the networks operated by Institute Nazionale di Geofisica e Vulcanologia (INGV) and Italian Civil Protection Department (DPC). Figure (1-6) shows the time history of the alert issuing as given by PRESTo and SAVE. In Presto the alert is based on the prompt estimation of location, magnitude and ground shaking prediction through specific GMPEs. While, in SAVE the alert is based on the direct estimation of the predicted intensity at the site as given by the measure of the first P-amplitude. The blind zone is the region within which the strong shaking waves arrive before the alert which it is drastically reduced using the onsite method.

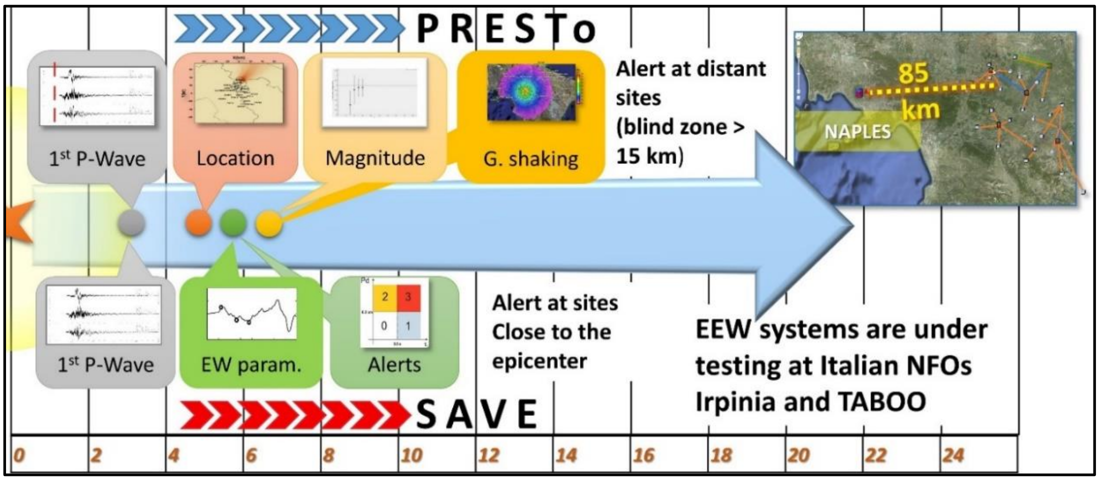

Figure 1-6: Time history of the alert issuing as given by PRESTo and SAVE for the selected case study *i.e.*, the 2016, August 24 central Italy earthquake [RISSC-Lab].

PRESTo has been installed on the server managing the real-time data streaming from the INGV network nearby Ancona, a city in the Marche region in central Italy. Therefore, in the real-time application, PRESTo issues the first alert after triggering 6 stations at 01:36:46.3 in the Coordinated Universal Time (UTC) which is 11.4 and 14.3 seconds after the first pick (near Amatrice) and origin time (reported by INGV), respectively. In comparison to INGV bulletin, the reported location by PRESTo is approximately 1.8 km far from the real epicenter, and the estimated magnitude is about 0.2 less than its real value. Note that there is a latency about 3-4 seconds, up to 10-20 seconds coupled with the low density of data in the epicentral area.

Moreover, PRESTo is evaluated in off-line mode using the seismograms of the earthquake recorded by the RAN stations belong to DPC network. In this regard, the first alert is issued after triggering 5 stations at 01:36:38.6 UTC which it is 3.8 and 6.6 seconds after the first pick (near Amatrice) and origin time (reported by INGV), respectively. Compared with INGV bulletin, the reported location by PRESTo approximately is 1.7 km far from the real epicenter and magnitude is about 0.2 less than the real value. Figure (1-7) presents the accuracy of PRESTo in predicting the instrumental intensity at the recording sites of the network. To this purpose, prediction error on PGV and Intensity (I_{MM}) are evaluated at the recording sites. A description of the ground shaking would have been available about 6-7 seconds after the origin time.

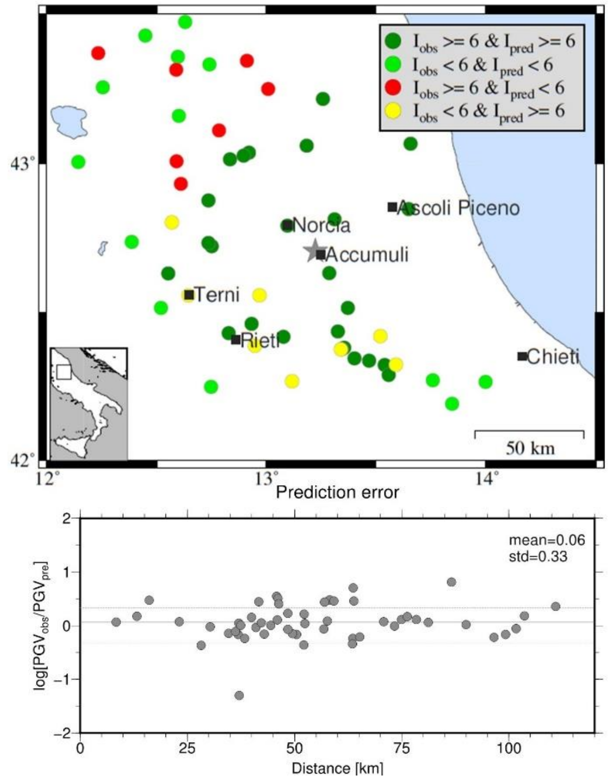

Figure 1-7: Top, a map showing the performance of PRESTo in terms of correct predictions (dark and light green), underestimated prediction (red) and overestimated predictions (yellow). Bottom, plot shows the prediction error on PGV, which is the proxy parameter used to estimate the I_{MM} [RISSC-Lab].

For this event, the analysis and performance of the onsite system *i.e.*, SAVE, is evaluated as well. Figure (1-8) shows a play-back of the seismic record acquired at the station AMT of the RAN. The onsite method estimates the intensity through the predicted PGV at the site, the latter parameter related to the P-wave peak displacement. The joint measurement of the P-wave peak displacement and characteristic period allows to get estimation of the magnitude and distance which are provided according to a broad classification given the expected uncertainty on these parameters as obtained from a single station. Finally, the alert level is given by the combination of the measured peak displacement and characteristic period [*Zollo et al*, 2010].

However, the performance of the SAVE in off-line analysis of RAN records is examined by setting a threshold for the instrumental intensity (I_{MM} >=VII). The correct intensity prediction is obtained in 83% of the cases, while 12% are the false alarms and only 4% the missed alarms. The latter are observed at a relatively large distance and along the rupture directivity direction. The accuracy of SAVE in predicting the instrumental intensity at the recording sites of the network is presented in Figure (1-9).

1.6 Limitation of Standard Approaches; The Next Generation of the EEWS Systems

Nowadays EEWS is becoming one of the important issues in earthquake seismology and many scientific researches have been done to develop it [*Kanamori*, 2005; *Wu and Kanamori*, 2008; *Böse et al*., 2009; *Zollo et al*., 2010; *Picozzi et al*., 2015; *Colombelli et al*., 2015; *Caruso et al*, 2017; *Nazeri et al*., 2017; *Nazeri et al*., 2019]. Despite the outstanding development, progressing of this new technology is still at the beginning of a long way. Estimation of all earthquake characteristics is mainly based on initial part of the motions with rather non-negligible uncertainty. Simplifications of most processes and algorithms used in standard EEWS approaches are dominant part of computations to model the earthquake source and the related wave propagation. For instance, the peak motion prediction in EEW methods are typically based on the point-source approximation and on 1D empirical attenuation relationships, depending on magnitude and hypocentral distance. However, for large events (M>6) such a simplified representation is inadequate and may result in unreliable predictions of the expected shaking, thus reducing the effectiveness of the EEW systems.

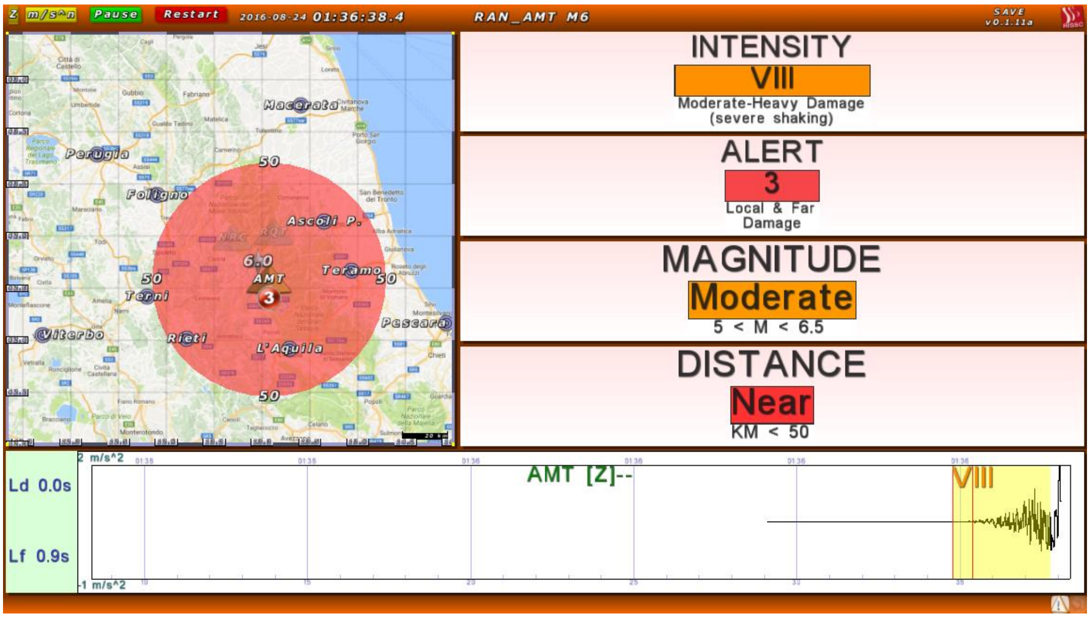

Figure 1-8: Snapshot of running SAVE during the playback of the Amatrice earthquake [RISSC-Lab].

On average few portions of the P-waves, maximum 3 seconds, is used to real-time estimation of the event magnitude and location, that could be a problem for any calculation of the ground motion of large events. The rupture process of an earthquake is the result of a complex combination of many factors, and the final magnitude depends on some average quantities of the whole process. In case of a large earthquake (M > 7) tens of seconds are necessary for the whole process to be achieved.

To evaluate the effectiveness of EEW systems for large events, the 2011 Tohoku-Oki earthquake is normally an interesting topic. This event represents a unique opportunity to check the extension of available EEW methodologies up to giant earthquakes, to bring out their limits and to propose new strategies to overcome such limitations. For this earthquake, the constraints of the standard EEW approaches have become evident as the complexity of the rupture process played a key role for the real-time magnitude estimation.

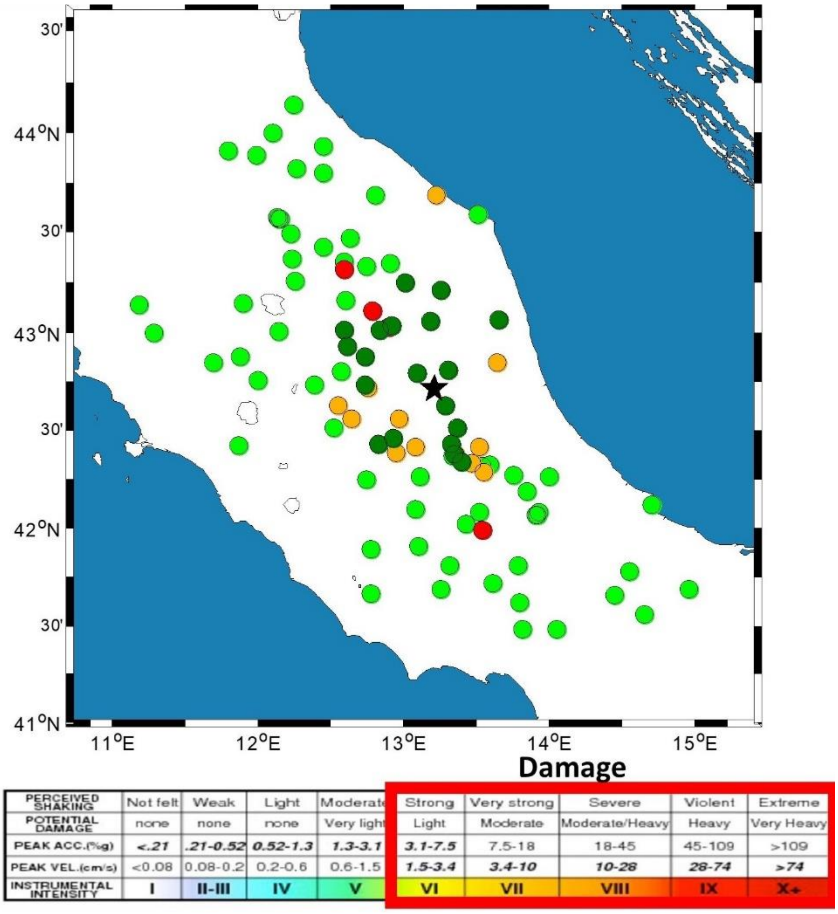

Figure 1-9: showing the performance of SAVE in terms of estimated I_{MM} [RISSC-Lab].

During the event, the dense strong motion networks deployed across Japan provided seismic observations over wide ranges of distances and azimuths from the source, with a high signal-to-noise ratio up to several hundred kilometers from the source. Figure (1-10) presents the performance of EEWS during this event. Kinkazan seismic station detected the threshold excess of filtered acceleration at 14:47:02.9 and provided the control signal to trains between Shiroishi-Zaoh station and Kitakami station of the Tohoku Shinkansen line. Subsequently, other seismic stations began issuing signals through the excess of acceleration threshold almost sequentially according to certain delays caused by wave propagation from the hypocenter. Finally, all the lines of Tohoku Shinkansen (from Tokyo station to Shin-aomori station) were controlled. It is reported that deceleration by emergency brake of a Shinkansen train is roughly 2.6 km/h/s. While, the estimated LT is up to 12-22 seconds, which it corresponds to reducing speed of about 30-60 km/h. Though the reducing speed is limited, the speed reduction is considered very significant for the safety of high-velocity Shinkansen trains.

First, Japan Meteorological Agency released the initial magnitude about M 4.3 that it was significantly underestimated and then, two minutes after the earthquake occurrence magnitude was reported as value of M 8.1. Clearly, all these points refer to use of few portions of the P-wave to estimate the required parameters which it is not adequate to determine the final values for such a large event and ongoing rupture.

Thus, in this thesis, we aim to develop the methodologies to improve the accuracy of real time ground motion prediction, through the fast determination of magnitude and fault plane geometry. All estimates are used to build the simplified kinematic source models and then convolving with pre-computed Green’s functions to provide complete wavefield synthetic seismograms, then providing early estimates of the expected intensity measures (PGA/PGV) at the EEW target sites. The alert decision scheme is defined upon the exceedance of a user-compliant PGA/PGV threshold by the predicted synthetic values.

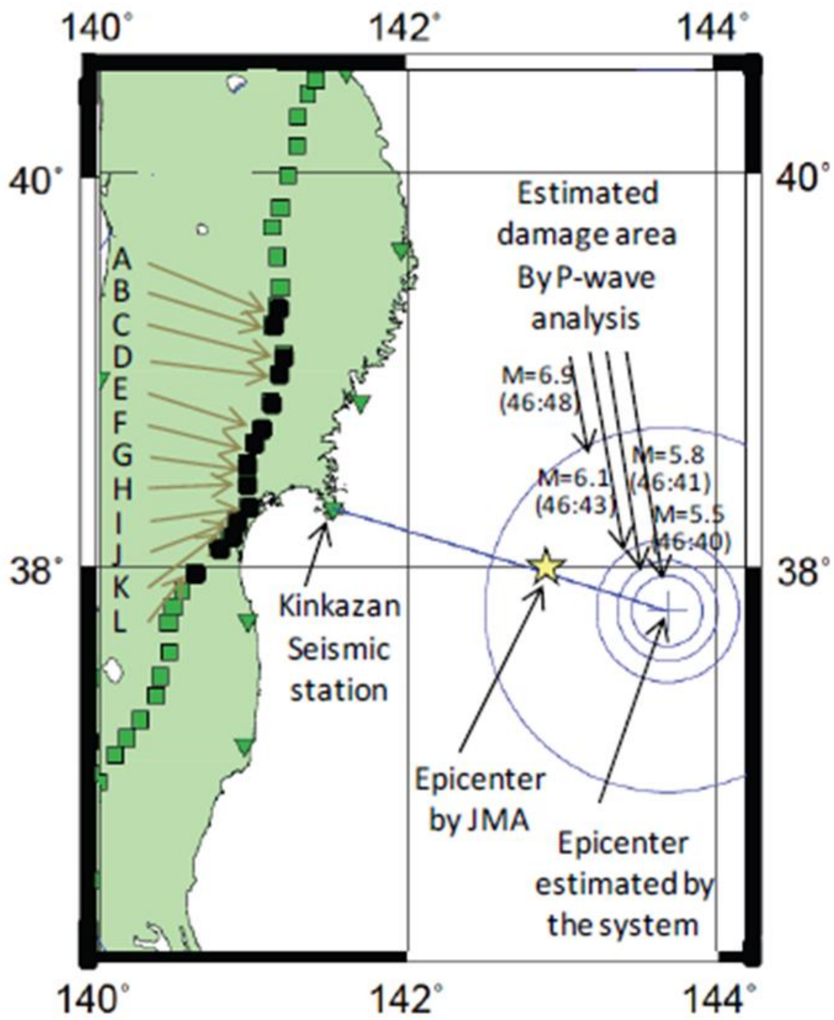

Figure 1-10: Performance of EEWS during M 9, 2011Tohoku earthquake. Locations of the epicenter (star) and Kinkazan seismic station. The epicenter estimated by the system (cross) and damage area (circles) are also shown. Circles show the estimated damage areas for P-wave warning that were issued by Kinkazan seismic station at 14:46:40.0, 14:46:41.0, 14:46:43.0 and 14:46:48.0. Estimated magnitudes for the warnings are also described beside the circles [RISSC-Lab].

CHAPTER 2

Rapid Estimation of Earthquake Source Characteristics

This chapter has been published as:

1. Sahar Nazeri, Simona Colombelli, Aldo Zollo, Fast and accurate determination of earthquake moment, rupture length and stress release for the 2016–2017 Central Italy seismic sequence, Geophysical Journal International, Volume 217, Issue 2, May 2019, Pages 1425–1432, https://doi.org/10.1093/gji/ggz097

2. On the way Paper, New LPXT approach, Prametrization

2.1 Introduction

Undoubtedly, earthquake is one of the most complex natural phenomena for which the accurate determination of all characteristic parameters is a difficult task. Although nowadays, estimating some earthquake properties such as location, magnitude, and moment tensor is well-performed, characterizing the source properties such as average slip, fault length/surface and average stress drop is still a challenging issue [*Allmann and Shearer*, 2009; *Kaneko and Shearer*, 2015; *Zollo, et al.*, 2014]. The displacement spectra in the frequency domain is generally used to obtain the average kinematic and static source parameters [*Brune*, 1970; *Madariaga*, 1976]. To model the dynamics of the rupture and the related parameters, such as the dynamic stress drop, the high-frequency content of the spectrum is needed, and this may be affected by some complexities of the medium, like distance attenuation and path effects [*Allmann and Shearer*, 2009]. Moreover, the point-source approximation is usually assumed to model the rupture process on an extended fault surface, depending on the source-to-receiver distance and on the observed frequency content of the recorded signals. This is an acceptable assumption for small-to-moderate events (M<4.0-5.0), while it may produce significant bias in the ground shaking prediction for large magnitude events (M≥6.0–6.5) [*Zollo et al.*, 2007; *Rydelek et al.*, 2007; *Festa et al.*, 2008]. Furthermore, the ground shaking prediction is generally based on the magnitude estimate and on the use of standard isotropic Ground Motion Prediction Equations (GMPEs), which account only for the source-to-site distance and do not consider the azimuthal variation of the radiated wavefield. Thus, for large seismic events, the distance of the site of interest from a fault, the approximation of a single radiating point, may be inadequate. Nevertheless, there is strong evidence for a dominant finite-rupture effect on the distance/azimuth distribution of the ground shaking radiated by extended faulting phenomena especially at near-fault distances, *e.g.*, distance comparable with the fault length [*Archuleta and Hartzell*, 1981; *Somerville et al.*, 1997; *Koketsu et al.*, 2016]. Therefore, in the shake map computation, the finite extension of the source (length, width of the fault plane) is a relevant piece of information to be known, along with the focal mechanism which gives the fault geometry and orientation. Indeed, the knowledge of the expected rupture length and orientation will improve the accuracy in predicting the ground motion amplitude during moderate to large earthquakes; thus, producing realistic strong motion shake maps.

In this chapter, following a similar approach as used by *Colombelli and Zollo* [2015], first we have refined and tested the LPXT methodology (Logarithm of the Peak X:Displacement/Velocity/Acceleration as a function of the P wave Time window) for the automatic and rapid determination of source parameters (moment magnitude/average slip, fault length/surface and average stress drop) using the events of 2016-2017 Central Italy seismic sequence [*Chiaraluce et al*., 2017]. Then, to better illustrate this approach, we evaluate the theoretical modelling to calculate moment magnitude estimation as a function of stress drop and rupture velocity. This new approach *i.e*., parametrization of the LPXT curve and its regional dependency, we also investigate Japanese dataset, magnitude range of 2.5 to 6.5. Indeed, in the second study, we more focus on estimating the magnitude using the plateau level of the curve. In the following sections, both datasets and results are discussed in detail.

While the approach proposed in this work has been originally conceived for the off-line characterization of the earthquake source properties, it is worth to note that the same approach can be also adapted to Earthquake Early Warning Systems (EEWS) and used for the real-time estimation of the main source parameters.

On the other end, as the current chapter and the next ones are generally about evaluating the source properties of the earthquakes, before going through the main topic of the interested methods, first the fundamental theory and the required conceptions are briefly overviewed.

2.2 Seismic Source Configurations

Most of seismic sources involve faulting or shearing motions on surfaces inside the earth resulting from a sudden release of energy in the Earth's lithosphere that creates seismic waves. The mechanisms of the causative fault of the earthquake are classified to three main types: normal, reverse (thrust), and strike-slip. In the other point of view, a point source and an extended source are two main configurations to model an earthquake source. Although the rupture process can be simply model as a point source, there is a strong limitation in the case of an complex rupture process, possibly resulting from the inclusion of a non-double-couple force system (the compensated linear vector dipole's component, in the moment tensor inversion). For large-magnitude earthquakes ($M_w > 7$), indeed, the slip distribution on the fault plane is often heterogeneous, both in terms of amplitude and in terms of vector orientation. Thus, a unique and simplified model such as the double-couple representation may not be realistic to describe the source complexities.

For a point source, the kinematic rupture process is completely defined by the so-called source time function. While for an extended source, the rupture velocity and the dimensions of the slip plane are explicitly included in the seismic source model. In general, the slip plane is divided into a number of relatively small slip patches. In the following sections, single point source and extended source will be briefly explained.

Box 2.1: Seismic Wave Equation

In the seismic wave theory, one of the main points refers to finding the solution of the wave equation (2-1) to better description of the nature of the recorded seismograms generated by earthquake at the given station. Indeed, for an isotropic, elastic and homogeneous medium, the displacement equation can be described as a differential formulation [*Shearer*, 1999]:

$$\rho \frac{\partial^2}{\partial t^2} \overrightarrow{u(\vec{x},t)} = (\lambda+\mu)\nabla\left(\nabla.\overrightarrow{u(\vec{x},t)}\right) + \nabla^2\overrightarrow{u(\vec{x},t)} + \overrightarrow{f(\vec{x},t)} \tag{2-1}$$

where $\overrightarrow{u(\vec{x},t)}$ and ρ are displacement vector and density of the medium respectively, λ, μ are the Lame parameters. Figure (2-1) shows a schematic diagram of the rupture along a fault spreading from the hypocenter, or earthquake nucleation point.

All released energies radiated from different sub-fault regions are emitted as that of the seismic sources, trough the Earth's layers to reach to the Earth's surface. Note that the direction of the rupture propagation is not generally parallel to the slip direction. Moreover, the displacement field varies over the surface of the fault, and it is determined from the stress distribution acting on the rupture plane. Clearly, many quantities play the important and non-negligible roles to produce the seismogramsrecorded at the seiemic stations like the origin of the released energy (source of the rupture), medium and instruments. If $\overrightarrow{u(\vec{x},t)}$ denotes the displacement motion of the surface at time *t* and at the given site located at the Cartesian coordinates $\vec{x} = (x_1, x_2, x_3)$, we obtain:

$$\overrightarrow{u(\vec{x},t)} = S(\overrightarrow{x_0},t) * G(\vec{x},\overrightarrow{x_0},t) * I(\vec{x},t) \tag{2-2}$$

where $S(\overrightarrow{x_0},t)$, $G(\vec{x},\overrightarrow{x_0},t)$ and $I(\vec{x},t)$ present the terms related to the source, medium and instrument response respectively and the star-mark stands for the convolution. $G(\vec{x},\overrightarrow{x_0},t)$ contains all information of the waves propagating from the source to the receiver, known as Green's functions (GF).

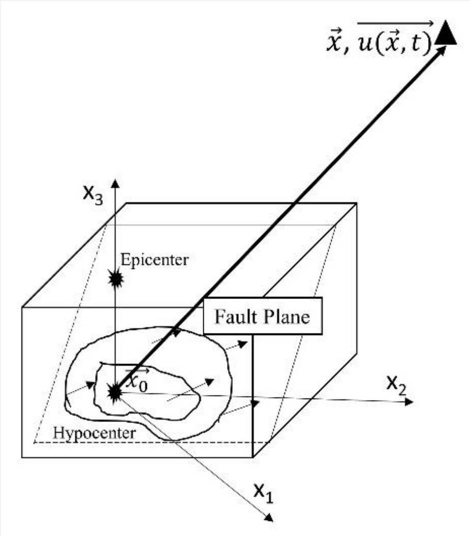

Figure 2-1: Schematic diagram of the rupture along a fault spreading from the hypocenter, or earthquake nucleation point. The station (triangular) and the hypocenter of the earthquake are located at $\vec{x}$ and $\vec{x}_0$ respectively. The small arrows indicate the directon of the rupture.

As it is also shown here, the GF concept is mathematically used to solve the differential equations, non-homogeneous boundary value problems. Note that the reference point is the source of the event located at $\overrightarrow{x_0}$ (Figure 2-1). Physically $\overrightarrow{u(\vec{x},t)}$ is the solution of the wave equation (2-1).

2.2.1 Point Source Approximation

The simplest possible model of a seismic source is a point source buried in an elastic half-space. Point source approximation is allowed when the receiver-source distance, R, is larger than a fault length (L) *i.e.*, $R >> L$ (Figure 2-1). In the other word, the rupture happens at a mathematically infinitesimal surface along the strike and dip directions. Considering this approach, $\overrightarrow{u(\vec{x},t)}$, the displacement on the surface is simply described in different terms as:

$$\overrightarrow{u(\vec{x},t)} = \frac{1}{4\pi\rho} A^N \frac{1}{R^4} \int_{\frac{R}{V_p}}^{\frac{R}{V_s}} \tau\, M_0(t-\tau)d\tau \qquad \text{Near-field term}$$

$$+ \frac{1}{4\pi\rho {V_p}^2} A^{IP} \frac{1}{R^2} M_0\left(t - \frac{R}{V_p}\right) \qquad \text{Intermediate-field P-wave term}$$

$$+ \frac{1}{4\pi\rho {V_s}^2} A^{IS} \frac{1}{R^2} M_0\left(t - \frac{R}{V_s}\right) \qquad \text{Intermediate-field S-wave term} \qquad (2\text{-}3)$$

$$+\frac{1}{4\pi\rho {V_p}^3} A^{FP} \frac{1}{R} \dot{M}_0 \left(t - \frac{R}{V_p}\right) \qquad \text{Far-field P-wave term}$$

$$+\frac{1}{4\pi\rho {V_s}^3} A^{FS} \frac{1}{R} \dot{M}_0 \left(t - \frac{R}{V_s}\right) \qquad \text{Far-field S-wave term}$$

where ρ is density, t is time, V_p, V_s are P-wave and S-wave velocity respectively, and $M_0(t)$ represents the cumulative deformation on the fault and with its first derivative, $\dot{M}_0$, controls the shape of the radiated pulse for all terms. Note that medium is considered as infinite, homogeneous and isotropic. $M_0(t)$ increases gradually by time after starting the rupture and reaches to a constant value of M_0 at the end of the process. M_0 is known as the seismic moment tensor which depends on the source strength and fault orientation. This parameter characterizes all the information about the source of the rupture. In fact, the moment release of the earthquake as a function of time is known as either the "source time function" or the "seismic moment rate function". For example, for a small earthquake with the fault as a single point source, displacement on fault can be considered to occur as a ramp function. Thus, the source time function arising from a ramp time history on a single point source is a boxcar of length τ_r, which is the rise time of the ramp function. While for large earthquakes, the source time function is more complicated. Note that to consider the earthquake source/fault as a single point source, all methods should be applied at "low" frequencies, for which the corresponding wavelengths are much longer than the fault dimensions. In addition, in this case, the dimensions of the slip plane and the rupture velocity are indistinguishable and implicitly included in the dynamics of the source time function.

Almost all seismic data used in geophysics are collected in the far-field, while those data used in earthquake engineering are occasionally collected in the near-field. Note that the discrepancy between the far-field and near-field terms mainly refers to the receiver-source distance which is dominant in the far-field terms. In equation (2-3), the far-field terms for both P- and S-waves are indicated that the amplitude attenuates as R^{-1} and propagate with speed V_p or V_s with arrival time around R/(V_p or V_s) for P- and S-waves respectively [*Aki and Richards*, 1980].

2.2.2 Extended Source Approximation

In the real world and not in the far-field point of view, the point source approximation is too simple to be considered as a proxy for a complex earthquake rupture. The first idea is to specify the earthquake source as a finite source and investigate the associated energy originates from works done by *Haskell* [1964, 1966, 1969]. Indeed acceleration, velocity, and displacement waveforms can be simulated from a finite source, *i.e.* a sequence of double couple point sources [*Haskell*, 1964], presenting unilaterally shear faulting [*Haskell*, 1969].

Hence, to model an extended source along fault strike, the rupture plane is divided into several slip patches. For each slip patch a source time function is defined, which is in general a function of space and time. The source time functions, representing the slip rate for each slip patch, are all the same except for a time shift defined by the rupture velocity. If we simply consider the extended source as a line source with a total length of L, the radiation of waves in an infinite homogeneous medium can be represented as a continuous superposition of both inhomogeneous and homogenous plane waves [*Bounchon and Aki*, 1977]. Moreover, waves propagate like a cylindrical in the medium [*Bounchon and Aki*, 1977]. Therefore, the displacement and stress along the vertical z and horizontal x axis to the source axis is written as:

$$F(x,z;\omega) = e^{i\omega t}\int_{-\infty}^{\infty} f(k,z)\, e^{-ikz} dk \tag{2-4}$$

where the integral is over the horizontal wave number k, t is time and ω is the circular frequency. In order to transform the integral into a summation, an infinite distribution of sources at equal interval L and along the x-axis is considered:

$$G(x,z;\omega) = \int_{-\infty}^{\infty} f(k,z)\, e^{-ikz} \sum_{m=-\infty}^{\infty} e^{-ikmL}\, dk \tag{2-5}$$

Regarding the distribution theory [*Schwartz*, 1966], the summation term can be expanded using the Dirac delta function as:

$$\sum_{m=-\infty}^{\infty} e^{-ikmL} = \frac{2\pi}{L}(\delta(kL) \tag{2-6}$$

by considering $k_n = \frac{2\pi}{L}n$, equation (2-5) becomes:

$$G(x,z;\omega) = \frac{2\pi}{L}\sum_{m=-\infty}^{\infty} f(k_n,z)e^{-ik_n x} \tag{2-7}$$

when the series converges, the equation becomes:

$$G(x,z;\omega) = \frac{2\pi}{L} \sum_{m=N}^{N} f(k_n, z) e^{-ik_n x} \tag{2-8}$$

finally, from this complex frequency solution ($G(\omega)$), the impulse response *g(t)* is obtained as:

$$g(t) = \int_{-\infty}^{\infty} G(\omega)\, e^{-i\omega t}\, d\omega \tag{2-9}$$

Note that all these concepts to find the final solution for a line source is known as "Discrete Wavenumber theory".

2.3 Real-Time Characterization of the Extended Seismic Source

Characterizing the earthquake source is always one of the interesting topics for seismologists as it helps to better understand the mechanism of the rupture. In many literatures, different algorithms, mainly based on circular cracks, are developed or modified to calculate the source properties. *Brune* [1970], *Sato & Hirasawa* [1973] and *Madariaga* [1976] source models are more universal since they describe the source considering the far-field displacement spectrum based on different initial hypothesis. In general, probabilistic and complex inversion methods and spectral approaches become more widespread in seismological applications specially in computing the kinematic source properties like size, stress drop, direction of the propagation and so on [*Piatanesi et al.*, 2007; *Minson et al.*, 2013; *Song and Somerville*, 2010; *Supino et al.*, 2019]. However, in the following sections, we present a fast and robust method known as Logarithm of P-wave Peaks in different Time windows, LPXT method where X stands for different waveforms used to follow the process *e.g.* D, V or A for Displacement, Velocity or Acceleration respectively [*Colombelli et al.*, 2014, 2015; *Nazeri et al.*, 2019].

2.4 LPXT Method; Logarithmic P-Wave Peaks in Different Time Window

Colombelli et al., [2014] introduced the LPDT method using the displacement signals. Indeed, the main idea of this algorithm refers to generate an informative curve in logarithm scale which it is generated based on the evolutionary behaviour of the P-wave peak displacement with time. *Colombelli et al.*, [2014, 2015] conclude that the LPDT curve carries information (dimension of the earthquake source and seismic moment) about the earthquake source, so then it can be used as a proxy for the final size of the rupture. Here in this study we generate the LPXT curve for acceleration and velocity as well.

Therefore, for each available waveform, we measure three initial peak amplitude as the absolute maximum on acceleration, velocity and displacement waveforms, named P_a, P_v, and P_d, respectively. The peak amplitude parameters are measured in progressively expanded time window, starting from the P-wave onset using a given time step which should be comparable with the data sampling time (Figure 2-2). Note that the minimum time window equals to data sampling. To correct the observed amplitude for the distance attenuation [*Zollo et al.*, 2006; *Nazeri et al.*, 2017], we first derived the empirical attenuation relationships for the studied area and for each parameter assuming the following polynomial form:

$$\log P_x = A_x M_w + B_x \log R + C_x \tag{2-10}$$

where M and R are the moment magnitude and hypocentral distance in km and P_x is the considered ground motion quantity, with the subscript x denoting a, v and d for acceleration in cm/s^2, velocity in cm/s and displacement in cm. To estimate the coefficients (A_x, B_x, and C_x) of this relationship listed in Table 1, a least squares multiple regression analysis is used.

We first estimate these coefficients for different time windows and find that the three coefficients do not change significantly with the window length, so the same coefficients measured in a fixed time window of 3.0 seconds are used for the entire duration of the LPXT curves (Figure 2-3).

Table 1. Coefficients of equation (1) for each waveform.

	A	**B**	**C**	**Standard error**
Acceleration	0.6	-2.7	1.64	± 0.37
Velocity	0.76	-2.3	-1.26	± 0.32
Displacement	0.92	-1.85	-3.63	± 0.35

Once the observed amplitudes are corrected (*i.e.*, normalized to a reference distance of 1 km) by the hypocentral distance (hereinafter named P_a^C, P_v^C, and P_d^C), using the equation $\log P_x^C = \log P_x - B_x \log R$, the LPXT curves (in acceleration, velocity and displacement) are built as the average value of the logarithm of corrected peak amplitude parameters. The LPXT curves are computed at any time step after the P-wave arrival time and before the expected arrival of the S-wave, which is set by a preliminary estimated empirical relationship between the S-P travel time and the hypocentral distance (see Figure 2-2a).

Thus, at each time step, the vertical component waveforms, possibly contaminated by the S-wave arrivals, are automatically excluded. Hence, by increasing the time window, the closest stations are eliminated one by one, and the computation is finally stopped when a minimum number of stations is available (it can be fixed as 3 to 5 stations depends on the number of available stations).

To model and interpret the observed shape of LPXT curves, we simulate a triangle-like moment rate function (MRF) considering a circular crack, following the formulation of *Sato and Hirasawa*, [1973] for a constant-velocity, circular rupture and generate its corresponding LPDT curve by using a similar procedure as for real data (see Figure 2-2c). As it is clear in Figure 2-2c, the increase of the MRF corresponds to an increase of the LPDT curve and the beginning of the plateau on the LPDT curve (Plateau Time) occurs at the peak of the MRF.

Thus, the plateau level carries information on the maximum amplitude of the MRF and the corresponding saturation time is related to the half-duration of the triangular function. Theoretically, for a circular rupture propagating at a uniform velocity from the nucleation of the rupture to the border, the relation between the source radius and half-duration is independent on the specific dynamic rupture model. Therefore, by considering all azimuthal coverage around the fault, the average Half-Duration (HD) is obtained as [*Aki and Richards*,1980], more detail is explained in Box 2.2:

$$< HD >= \frac{a}{v_r}\left(\frac{\pi}{2} - \frac{v_r}{v_p}\right) \tag{2-11}$$

where a is the source radius, v_r is rupture velocity and v_p is the P-wave velocity.

Given an estimate of the half-duration of the source, the above equation allows estimating the radius of a circular earthquake rupture, without complex procedures and waveform analysis. Note that in the LPXT method, the corner time of the plateau level (highlighted by “Plateau Time” in Figure 2-2b) is equivalent to half-duration (Figure 2-2c). Then, the stress drop ($\Delta\sigma$) is derived from moment (M_o) and source radius (a) estimation using the *Keilis-Borok* [1959] equation, $\Delta\sigma = \frac{7}{16}\frac{M_o}{a^3}$.

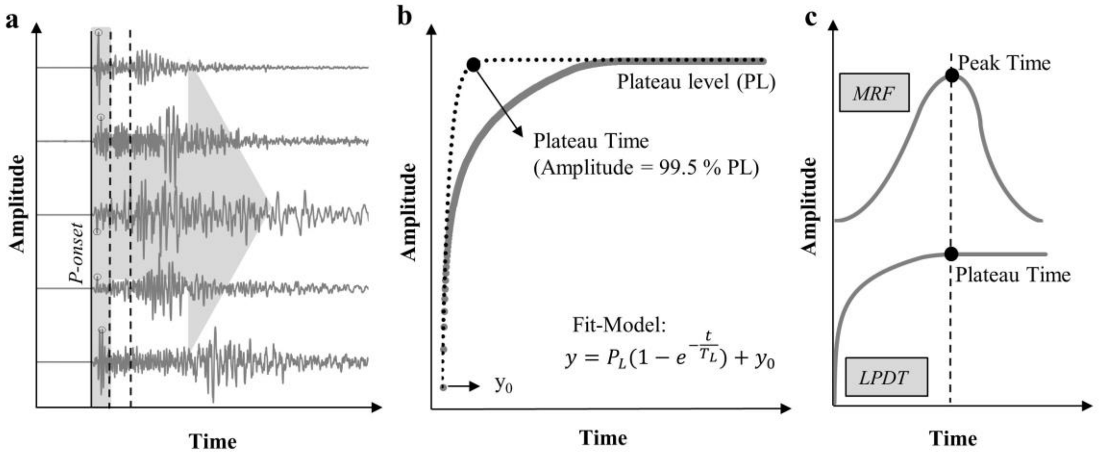

Figure 2-2: Relationships between LPDT curves and MRF. (a) The figure shows the different time windows (dashed lines) after the P-wave triggering on some sample traces, to compute the peak amplitudes on each time window. (b) an example of final LPDT curve for a single event calculated from observed data. To model the observed curves, we used an exponential fitting function (expression 3), for which y_0 (*i.e.*, the intercept of the curve) is fixed to the first point of the curve. To correctly estimate P_L and T_L we applied a weighted regression procedure to fit the LPDT curve (dotted curve). (c) The triangle-like moment rate function (MRF) and its relevant LPDT curve. The dashed line represents that the maximum level of the LPDT curves (Plateau time) occurs at the peak of the MRF (Peak Time).

Box 2.2: Half-duration and duration of the circular rupture [*Aki and Richards,1980, Zollo and Emolo*, 2011]

By considering the circular rupture model, here all steps to drive the corresponding formula of the Half-Duration (HD) and Total-Duration (T_d) are explaind. HD at at the station is the time difference the signals emitted by the closest fault point (P_1) and the nucleation of the rupture (O).

$$\Delta T = T_{P_1} - T_O = \left(\frac{a}{V_r} + \frac{R_1}{V_p}\right) - \frac{R}{V_p} \cong \frac{a}{V_r} + \frac{R - a\cos\left(\frac{\pi}{2} - \theta\right)}{V_p} - \frac{R}{V_p} \quad (2\text{-}12)$$

$$\Delta T = HD = \frac{a}{V_r} - \frac{a}{V_p}\cos\left(\frac{\pi}{2} - \theta\right) = \frac{a}{V_r} - \frac{a}{V_p}\sin(\theta) \quad (2\text{-}13)$$

Therby the average HD among all stations distribuated over azimuth-distance around the nucleation point is calculated by integarting over θ angel as:

$$\langle \Delta T \rangle = \overline{HD} = \int_0^{\frac{\pi}{2}} \left(\frac{a}{V_r} - \frac{a}{V_p}\sin(\theta)\right) = \frac{a}{V_r}\frac{\pi}{2} - \frac{a}{V_p}\int_0^{\frac{\pi}{2}} \sin(\theta)$$

$$= \frac{a}{V_r}\frac{\pi}{2} - \frac{a}{V_p} = \frac{a}{V_r}\left(\frac{\pi}{2} - \frac{V_r}{V_p}\right) \quad (2\text{-}14)$$

To compute T_d, the proccess is the same as HD as below:

$$\Delta T = T_{P_2} - T_O = \left(\frac{a}{V_r} + \frac{R_2}{V_p}\right) - \frac{R}{V_p} \cong \frac{a}{V_r} + \frac{a\cos(\theta)}{V_p} = \frac{a}{V_r}\left(1 + \frac{V_r}{V_p}\cos(\theta)\right) \quad (2\text{-}15)$$

$$\langle \Delta T \rangle = \overline{T_d} = \int_0^{\frac{\pi}{2}} \frac{a}{V_r}\left(1 + \frac{V_r}{V_p}\cos(\theta)\right) = \frac{a}{V_r}\left(\frac{\pi}{2} + \frac{V_r}{V_p}\int_0^{\frac{\pi}{2}}\cos(\theta)\right) = \frac{a}{V_r}\left(\frac{\pi}{2} + \frac{V_r}{V_p}\right) \quad (2\text{-}16)$$

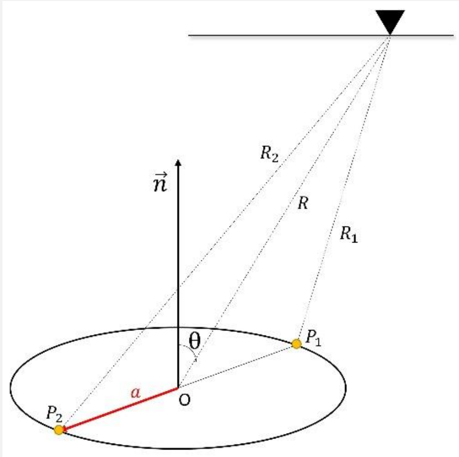

Figure 2-4: Circular fault rupture geometry.

2.4.1 Modelling the LPXT

In the original work of *Colombelli and Zollo* [2015], the LPDT curves are modelled using a piecewise linear function, which is a too simple model to describe the continuous time evolution of the ground motion amplitude. Here, to model the observed LPXT curves, we adopted an exponential function of the form:

$$y = P_L(1 - e^{-\frac{t}{T_L}}) + y_0 \quad (2\text{-}17)$$

where P_L represents the plateau level of the curve and y_0 indicate the intercept of the plot with the y-axis. Mathematically, T_L is the time-constant and shows how rapidly an exponential function grows to the 63% of its maximum value, *i.e.* P_L.

The LPXT curves are obtained as the average among many stations distributed, in principle, over azimuth-distance. When the azimuthal gap is not fully covered by stations, the data deficiency around the source may strongly affects the middle part of the LPDT curves, resulting in irregular shapes, with the appearance of intermediate, small steps before the final plateau value. Therefore, to avoid unrealistic estimation of the fitting parameters, we apply a two-step regression analysis, first a standard unweighted regression analysis and then a weighted fitting procedure for the initial part of the curves. The first analysis is applied to estimate preliminary values of P_L and T_L parameters. The fitting process is then repeated using a weighted fit, where a larger weight is assigned to the initial part of the curve, from the beginning to T_L. The quality of the weighted-fit curve is previously shown in Figure 2-2b while the misfit values (at each time) are shown in Figure 2-7.

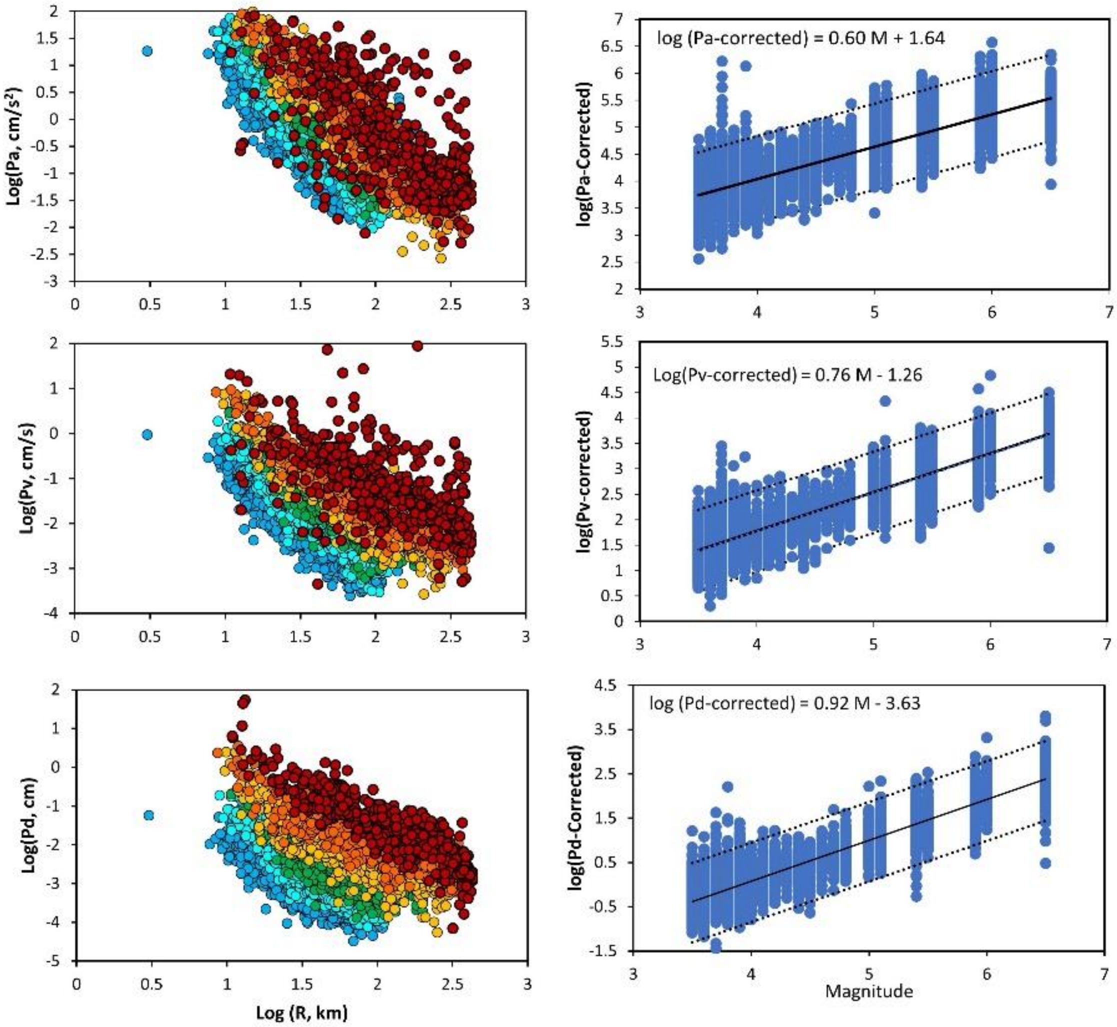

Figure 2-3: Left column: Plots show the logarithm of the Pa (top), Pv (middle) and Pd (bottom) calculated in 3 s after P onset versus logarithm of hypocentral distance (R). Colors represent the different range of magnitude; blue ($M \leq 4$), cyan ($4 < M \leq 4.5$), green ($4.5 < M \leq 5$), yellow ($5 < M \leq 5.5$), orange ($5.5 < M \leq 6$) and red ($6 \geq M$), **Right column:** Plots show the logarithm of the normalized Pa, Pv and Pd to the R. The best-fit lines with the appropriate standard deviation are shown by black solid and dotted lines, respectively.

Note that the parameter T_L is only used in the second step of the fit process. Figure 2-6a shows the scaling of P_L as a function of magnitude of the evaluated events (plotted in Figure 2-5a). Thus, immediately after computing P_L and estimating the magnitude based on the input data, the seismic moment M_0 can be easily calculated from the empirical relationship of the *Hanks and Kanamori* [1979] moment-magnitude scale. For each of the analysed events, the source radius is finally computed by inverting equation (2-11), and assuming that the corner time of the plateau on the weighted fit curve is equal to the half-duration of the source.

2.4.2 Application to Italian Earthquakes

We use a selection of earthquakes belonging to the 2016-2017 Central Italy seismic sequence, with moment magnitude ranging between 3.4 and 6.5. After a preliminary evaluation of the signal-to-noise ratio for all the available records, the original dataset (135 earthquakes) is reduced to 28 events with high-quality records, including 12 events with moment magnitude larger than 4.7. The earthquakes have been occurred in an active seismic region [*Meletti, et al*., 2016] of central Apennines in Italy and as it is shown in Figure 2-5a, almost all the events show a NW-SE striking, normal faulting mechanism. This long-lasting seismic sequence [*Luzi et al*., 2017] has started with the Amatrice earthquake, Mw 6.0 on August 24th while the largest event of the sequence, the Mw 6.5 Norcia earthquake, occurred on October 30th.

We use a total number of 1895 of vertical components of the ground motion waveforms, recorded within a maximum epicentral distance of 100 km. The map of the selected epicenters and stations is shown in Figure 1a. The selected stations belong to the Italian Strong Motion Network (Rete Accelerometrica Nazionale (RAN)), operated by the Italian Department of Civil Protection, and to the Italian National Seismic Network, operated by the INGV. The P-phase arrival times has been manually picked on all the vertical acceleration waveforms and a 0.075 Hz high-pass Butterworth filter is applied to the displacement records, to remove possible base-lines arising from low-frequency noise amplification due to the double integration of the accelerometric records.

2.4.3 Results and Discussion

Following above discussion, the proposed methodology is based on the use of LPXT curves with the main objective of calculating the seismic moment and source duration. As compared to the common procedures to compute the earthquake source parameters, this method is straightforward, accurate and fast. Indeed, in the standard, spectrum-based approaches, the seismic moment is calculated from the low-frequency part of the displacement spectra, while the source radius is estimated from the corner frequency [*Allmann and Shearer*, 2009].

According to the obtained results and the comparison with source parameter estimates using the other methods, which will be discussed later, no significant differences in uncertainties on source parameter estimations are observed. Indeed, although some uncertainties related to the manual phase-picking and data/fit-processing are predictable for the current algorithm that may affect the results, the uncertainties of the spectrum-based methods such as the ones related to the bias between the corner frequency and attenuation parameter, affecting the spectral shape are not negligible [*Kaneko and Shearer*, 2015].

As it is clear from Figure 2-5b, c, d, for all the analysed events and for the three ground motion quantities (P_a^C, P_v^C, and P_d^C), the LPXT curves have a similar shape and scaling, with small initial values and a final plateau value, that is generally higher and reached in a longer time for the larger magnitude events.

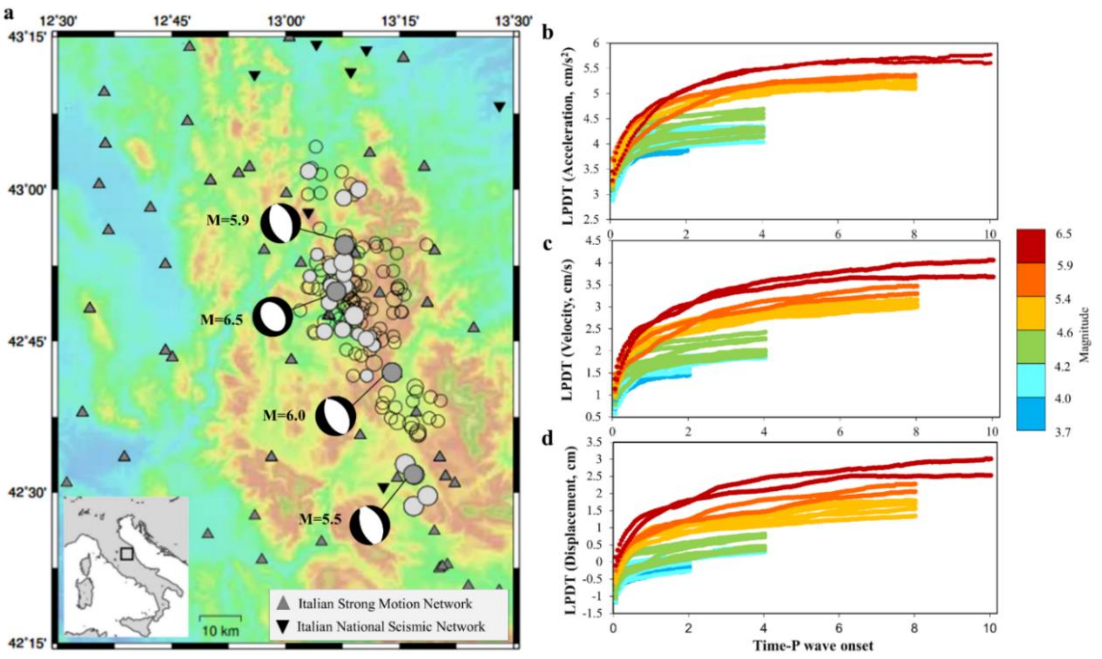

Figure 2-5: Italian Dataset and LPDT curves. (a) The map shows the distribution of all the events of the 2016 Central Italy sequence (black open circles) and the epicenter position of the selected earthquakes (grey filled circles), with a variable size, depending on the magnitude. Dark grey triangles show the position of the stations used for the analysis. The focal mechanism solution (as provided by INGV) is also shown of the largest events (M > 5.5). (b, c and d) LPDT curves: Average-logarithm of Pa^C, Pv^C and Pd^C in terms of different time windows exactly after the P-wave onset.

Therefore, the mentioned method can be applied to acceleration, velocity and displacement waveforms, with the main advantage of being easily exportable and adaptable to any kind of seismic network and of not requiring complicated data processing. A unique filter (high-pass Butterworth filter) is only applied to the displacement signals in order to remove base-line effects on the time series, while acceleration and velocity are used as they are recorded (only the mean value and the linear trend are removed). This is a further advantage of the methodology, since acceleration, velocity, and displacement provide a complementary image of the entire spectral content of the source.

To better interpret the LPXT curve, a continuous and parametric exponential function to model the curves is adopted with only two parameters, the characteristic time, T_L and the plateau level, P_L, both controlling the evolution and shape of the curves. The scaling of P_L is consistent with what has been found for the Japanese dataset [*Colombelli and Zollo*, 2015]. The plateau level, P_L, is linear increasing (in logarithmic scale) with the magnitude of the event, so that the larger the magnitude the higher the P_L value (Figure 2-6a). Therefore, as soon as the LPXT curve saturates, the magnitude is computed using the equation (2-10) *i.e.*, the empirical attenuation relationship between peak amplitudes, magnitude and the hypocentral distance.

Figure 2-6b represents the estimated source length and half-duration of the source time function for different events in the dataset which is computed from the corner time of the plateau level on the weighted-fit curve to the LPXT. In addition, we compute the theoretical scaling of the source radius as a function of magnitude using different fixed values of the stress drop from 0.1 to 10 MPa shown with different lines in Figure 2-6b. As it is evident from Figure 2-6b, for the considered magnitude range from small to moderate, the estimated values of the source radius are compatible with the theoretical expected trends and show a consistent self-similar scaling with magnitude. Specifically, for a magnitude 4.1, we find an average radius of about $1.1 \pm 0.17\ km$, while $6.5 \pm 0.76\ km$ is found for a magnitude 6.0 event. According to the computed source radius following the LPXT curves of the acceleration, velocity and displacement data, the average stress drop is 1.2 ± 0.6, 1.2 ± 0.5, and $1.0 \pm 0.4\ MPa$ respectively.

It is worthwhile to mention that, *Bindi et al.*, [2004] using aftershocks of the 1997 Umbria–Marche seismic sequence ($1.4 \leq M_L \leq 4.5$) in the central Italy, have also found a self-similar scaling of static stress drop with the average about $2.0 \pm 1.0\ MPa$ by analysing the S-wave spectra and using a non-parametric inversion approach. Moreover, the average stress drop estimated in this study is comparable with the average value of 2.6 MPa obtained for the 2009 L'Aquila sequence [*Pacor et al.*, 2016]. The proposed method represents a simple and automatic approach to quickly estimate the earthquake magnitude and the expected length of the rupture, solely based on the continuous measurement of the initial P-wave peak amplitude. Although the required parameters are obtained here in an off-line analysis, the same methodology can be used to the future implementation of real-time, earthquake shaking prediction or even early warning. For instance, the earthquake rupture moment, length and stress release as an output of this method can be considered as initial reference for a source model to be used for computing the synthetic seismograms and rapid strong ground motion scenarios for earthquake impact evaluation. This is indeed one of the objectives of a current EU H2020 project, SERA (Seismology and Earthquake Engineering Research Infrastructure Alliance for Europe).

For real-time applications, the only piece of information needed is a reliable estimation of the earthquake location, in order to properly account for the path attenuation effect and normalizing the observed amplitudes. In terms of real-time applications, further analyses are needed to simulate the continuous data streaming, accounting for the P-wave propagation through the seismic network and to evaluate the real-time performance of the methodology. Assuming a standard velocity model, we can theoretically compute the time at which the measurements of required parameters could be available at the network. Figure 2-6b shows that the source parameters would be available less than 1.0 s after the first P-wave arrival time for $M < 4.0$, less than 2.5 s for $4.0 < M \leq 5.0$, and less than 4.3 s for two large events in the dataset, *i.e.*, magnitude 6 and 6.5.

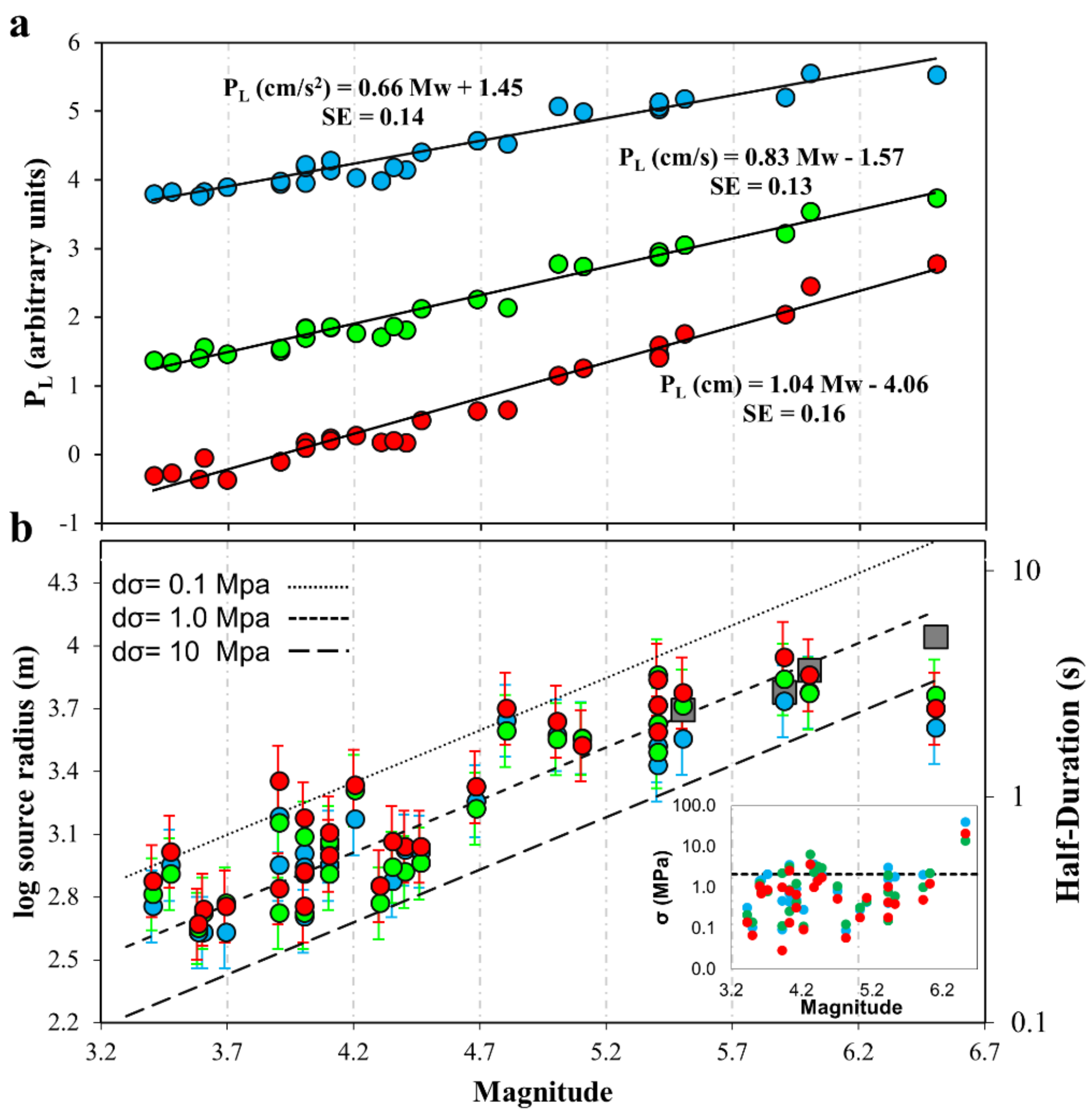

Figure 2-6. Scaling relationships vs. magnitude. (a) The plot shows the plateau values of the LPDT curves for acceleration, velocity and displacement as a function of magnitude. The best fit line is shown by a black solid line. The best-fit linear regression equation is also shown on the plot. (b) Scaling of the Logarithm of the source radius as a function of magnitude. The lines represent the theoretical scaling, with constant static stress-drop values (0.1, 1 and 10 MPa). The secondary y-axis presents the HD of the source time function. The inset plot shows the estimated stress drop for the individual earthquakes in the selected dataset. The average stress drop value (**Δσ** ≅ 1.1±0.5 MPa) is shown as a dashed line. The grey squares represent the values computed by *Madariaga* [1977] formula, using the average rupture length as obtained by two models [*Cheloni et al*., 2017; *Xu et al*., 2017]. In both panels, the estimated parameters related to the LPXT curves of acceleration, velocity, and displacement are shown with blue, green and red circles respectively.

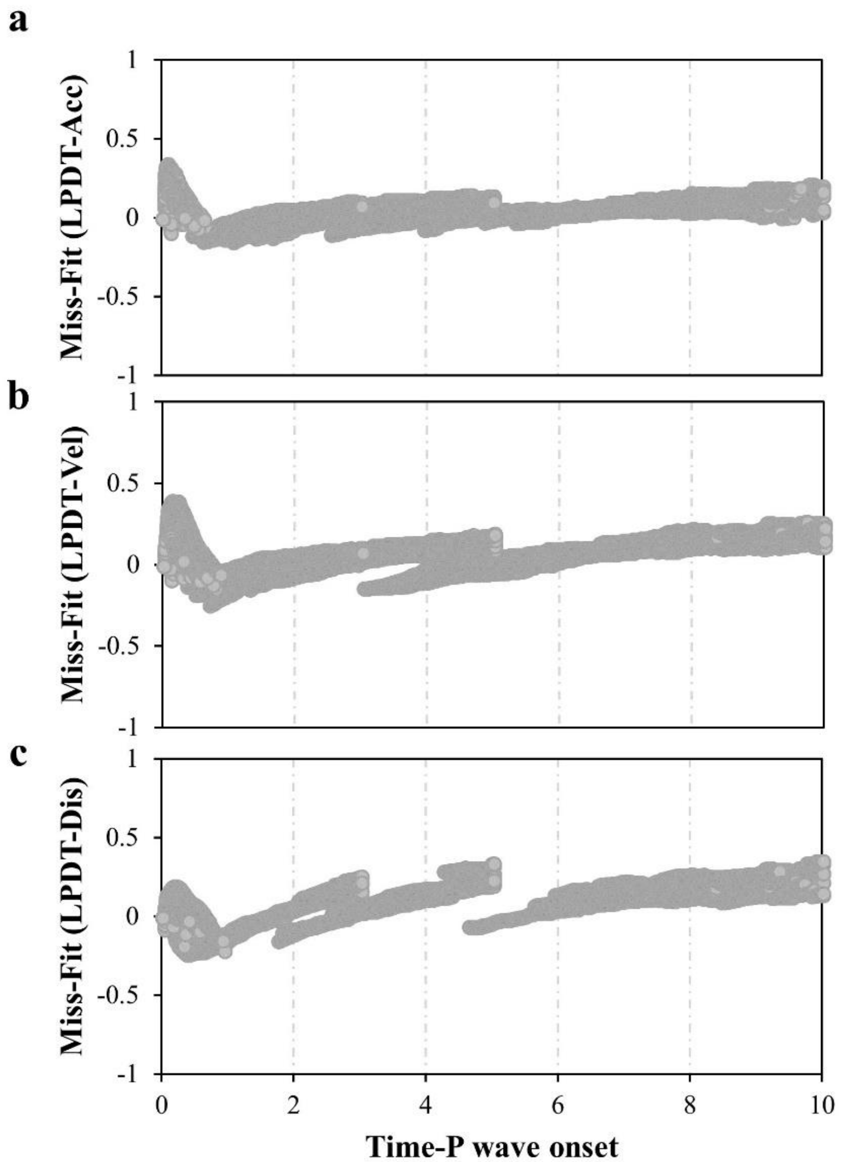

Figure 2-7: Misfit and residual analysis. The figure shows the mis-weighted fit at the initial and last part for all LPDT curves, computed based on the different used signals, *i.e.*, (a) acceleration (b) velocity and (c) displacement.

On the other hand, since the earthquake magnitude and the source properties are related to the released seismic energy, combining the S- and P-waves will obviously improve the final estimations but simultaneously arising some data processing complexity. While the use of the S-wave is strongly related to the existence of a dense strong motion network around the region of interest, the automatic detection of the S-phase is clearly not as simple as the identification of the P-phase. Because as mentioned above, the LPXT curve is average of the corrected P-wave amplitude by hypocentral distance, if we want to add the S-wave, we should also compute its attenuation relationship to correct the S-wave amplitude. Further computational complexities will be also due to the automatic selection of the coefficient for different phases. Thus, by only using the P-wave, the process is more straightforward, rapid, and noteworthy simple without any kind of complexities related to either considering the S-waves or computing the spectra of the waves as a routine way to compute the rupture properties.

2.4.3.1 Detail Discussion about the Major Earthquakes of the 2016-2017 Central Italy Seismic Sequence

For the four major earthquakes of the sequence with moment magnitude above 5.5, we also checked an independent estimation of the stress drop value, considering the rupture size provided by two different models, based on the joint inversions of Synthetic Aperture Radar (SAR), Interferometric SAR and Global Position System data [*Cheloni et al*., 2017; *Xu et al.*, 2017]. To estimate the static stress, drop of near-rectangular ruptures, we used the *Madariaga* [1977] equation to retrieve the static stress drop:

$$\Delta\sigma = \frac{1}{C}\mu\frac{\Delta u}{W} \quad (2\text{-}18)$$

where W is the fault width, μ is the rigidity at the source, Δu is the average final slip at the fault and C is a constant which depends on the specific fault geometry and slip direction. *Madariaga* [1977] evaluated C for circular, rectangular and elliptical fault geometries and found that it ranges between $C_{min} = \frac{16}{7\pi} = 0.73$ for circular ruptures and $C_{max} = \frac{\pi}{2} = 1.58$ for very long and thin ruptures. Note that the *Keilis-Borok* [1959] and *Madariaga* [1977] formulas provide the same static stress drop value for circular fault ruptures. In our estimation of stress drop values for the larger magnitude events of the Central Italy sequence, we used an intermediate value, *e.g.* $C = 1$, given the evidence of a near-rectangular faulting surface.

We find that the static stress drops (shown in Figure 2-6b with the grey squares) for these events are in a good agreement with the values estimated in the present study, with an average value of about $1.5 \pm 0.5\ MPa$, except for the $M_W = 6.5$, Norcia event. Indeed, for the largest event of the sequence, the estimated value of the source radius ($5.0 \pm 0.9\ km$) is smaller than the expected average value (about of 14 km) from the scaling relationship inferred from smaller magnitude events, with a consequent apparent higher value of stress drop (between about 15 and 44 MPa, with a mean value of $27.6 \pm 15\ MPa$) and shorter half-duration of the source (with an average of 2.3 s vs. a predicted value >3.0 s). The high stress drop value for this event is also consistent with the other independent estimates obtained from the energy-based procedures [*Picozzi et al*., 2017; *Bindi et al*., 2017]. A possible reason for the underestimated source size and high stress drop of the largest event could be the effect of the high-frequency radiation from a dominant slip-patch (up to $> 2\ m$ of average slip) [*Cheloni et al*., 2017] spreading over a smaller area than the final rupture surface. Although different authors reported a total rupture surface of about 80 to 200 km^2 [*Xu et al*., 2017; *Chiaraluce et al*., 2017; *Cheloni et al*., 2017], the dominant slip-patch which has radiated during this earthquake cover a surface of about 65 km^2 [*Cheloni* et al., 2017], which approximatively corresponds to the estimated source area (78 km^2) in this study. In this case, we conclude that our methodology is sensitive to the seismic radiation from the dominant slip release fault patch and may be not able to retrieve the secondary and more complex effects of the total source time function.

2.5 Parametrization of the LPXT Method

As discussed before, the LPXT method is mainly aimed to the calculation of the informative curves using all available observations [*Colombelli et al*., 2014, 2015; *Nazeri et al*., 2019]. Although in the previous studies by considering the circular rupture and assuming the *Sato and Hirasawa* [1973] model, we could interpret the observed LPXT curve as a proxy of the moment rate function (MRF), there is still a lack of theoretical framework putting the firm foundation for this data-driven method.. The key concern about the hypothesis is, thus, to understand how this empirical method can be formulated via basic physical concepts. For instance, although the earthquake magnitude is scaling with plateau level of the curves using the empirical equations shown in Figure 2-7a, it is advantageous to interpret it using a robust and strong theory, as well. Moreover, getting back to the basic definition of the earthquake magnitude, which is normally measured using the maximum motion, arises this question: what is the relevant amplitude to the obtained magnitude in this method? So, with aim of parametrization of the LPXT curve, in following a new strategy using far-field approximation is suggested to formulate this curve. Indeed, a theoretical source model is used to relate the MRF parameters to the corner-time and plateau of LPXT curves.

2.5.1 Theoretical formulation

To better interpret the obtained magnitude without any complexity, following the definition of various scales of magnitude based on the maximum amplitude of the corresponding waves, we try to parametrize the LPXT curve using the far-field approximation. Far-field P-wave displacement radiated from a point-source rupture in a homogeneous earth model [Aki and Richards, 1980] is defined by:

$$\Omega_o = \frac{F_S R_{tf}}{4\pi\rho {V_p}^3} \frac{1}{R} M_o \tag{2-19}$$

where R_{tf} is radiation pattern term, F_s is free surface coefficient, ρ is density, V_p is P-wave velocity in the given area, R is hypocentral distance, M_o is seismic moment and Ω_o is the area of the triangular source time function as it is presented in Figure 2-8. Considering the mathematical relation between the peak displacement and area of the triangular source time function, *i.e.*, $\Omega_o = \frac{P_d T_d}{2}$ where Td is total duration of the source rupture, the equation (2-19) is expressed in terms of P_d parameter. Then, using both equation (2-16) and *Keilis-Borok* [1959] formula, the equation (2-19) is simplified as below equation (2-21):

$$T_d = \left(\frac{7}{16}\right)^{1/3} \left(\frac{1}{\Delta\sigma}\right)^{1/3} M_0^{1/3} \left[\frac{\pi}{2V_r} + \frac{1}{V_p}\right] = K M_0^{1/3} \tag{2-20}$$

where K equals to $\left(\frac{7}{16}\right)^{1/3} \left(\frac{1}{\Delta\sigma}\right)^{1/3} \left[\frac{\pi}{2V_r} + \frac{1}{V_p}\right]$. Thus P_d is described as:

$$P_d = \frac{F_s\, R_{tf}}{4\pi\rho {V_p}^3} \frac{1}{R} \frac{2}{K} {M_0}^{2/3} \tag{2-21}$$

that in logarithm scale will be:

$$\log P_d = A_{pd} - \log R + \frac{2}{3} \log M_0 \quad , \quad A_{pd} = \log\left[\frac{F_s\, R_{tf}}{4\pi\rho {V_p}^3}\right] - 2\log K \tag{2-22}$$

this equation clearly represents standard attenuation relationship. By taking into account the *Kanamori* [1983] moment magnitude scale in $N.m$ *i.e.*, $M_w = \frac{2}{3}\log M_0 - 9.1$, will be simplified to equation (2-10) with below coefficients:

$$A_d = 1, \ \ B_d = -1, \ \ C_d = A_{pd} - 6.1 \tag{2-23}$$

Hence, the LPDT curve can be directly generated using the attenuation relationship derived from theory without any dependency to the region as:

$$\log P_d^C = \log P_d - \log R \tag{2-24}$$

Considering the moment rate function (MRF) of the circular rupture as a triangle (Figure 2-2c) and assuming the same shape for displacement with total duration of T_d (Figure 2-8), the same attenuation relation of peak amplitude can be also derived for the velocity (Box 2.3).

Accordingly, to generate the LPXT curves using the formula derived by far-field approximation, we only need to simply normalize the amplitude by considering the coefficient 1 for log(R) term in the attenuation relationships and compute the magnitude. Thus, as soon as the plateau level of the curve could be or extrapolated, the relevant magnitude is calculated as:

$$M_{w-LPDT} = \text{Plateau of the LPDT} - C_d \tag{2-31}$$

$$M_{w-LPVT} = \text{Plateau of the LPVT} - C_v \tag{2-32}$$

2.5.2 Japanese Dataset

Here, we evaluate Japanese dataset [*Colombelli et al*., 2014, 2015] and Italian dataset (Figure 2-5) [*Nazeri et al*., 2019] used in the previous studies and a new selection of Japanese earthquakes with moment magnitude ranging between 2.5 and 4. Figure (2-10) shows the location of the stations and Japanese earthquake epicenters including 43 moderate-to-strong events ($4 \leq M \leq 9$) used by *Colombelli et al*., [2014, 2015] and new selection of 31 small-to-moderate events ($2.5 \leq M \leq 4$).

Note that unlike the Italian dataset that most of the earthquakes (circles on the Figure 2-5) occurred at shallower depth with an average about 10 km, the depth of the Japanese events is deeper with an average around 30 to 40 km (Figure 2-9). We use all vertical components of the ground motion waveforms for Italian and Japanese dataset recorded within a maximum epicentral distance of 100 km. All data processing steps are exactly like the previous study which is also explained in section 2.4.3, except using the SI units for all measurements *i.e*., m, m/s and m/s^2 for displacement, velocity and acceleration peak amplitudes respectively and m for hypocentral distance.

Box 2.3: Parametrization of the LPVT

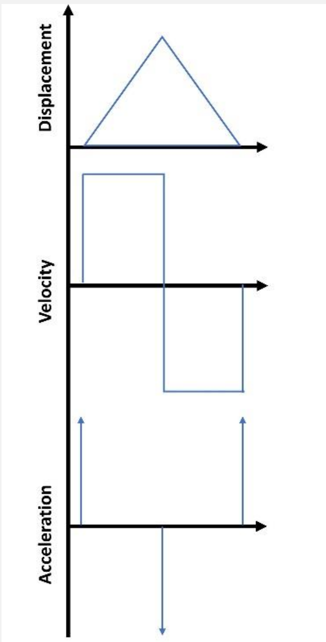

Figure 2-8: Simple schematic for displacement, velocity and acceleration, which velocity and acceleration are computed by derivative definition.

$$\mathrm{P_v} = \frac{\mathrm{P_d}}{\left(\frac{\mathrm{T_d}}{2}\right)} = \mathrm{P_d}\frac{2}{\mathrm{T_d}} \tag{2-25}$$

$$\log P_v = \log P_d - \log T_d + \log 2 \tag{2-26}$$

$$= \left[A_{pd} - \log r + \frac{2}{3}\log M_0\right] - \left[\log K + \frac{1}{3}\log M_0\right] + \log 2$$

$$\log P_v = \left[A_{pd} + \log 2 - \log K\right] - \log r + \frac{1}{3}\log M_0 \tag{2-27}$$

$$\log P_v = A_{pv} - \log r + \frac{1}{3}\log M_0 \tag{2-28}$$

$$A_{pv} = \log\left[\frac{F_s\, R_{tf}}{2\pi\rho {V_p}^3}\right] - 3\log K \tag{2-29}$$

Following the same steps done for equation (2-22), *i.e.*, putting the *Kanamori* [1983] formula in equation (2-21), equation (2-29) will be also simplified to equation (2-10) for the LPVT curve with below coefficients:

$$A_v = 0.5,\ \ B_v = -1,\ \ C_v = A_{pv} - 3.03 \tag{2-30}$$

2.5.3 Result and Discussion

Following the new approach, we regenerate the LPDT/LPVT curves for all Italian and Japanese dataset and compute the plateau level of the curves (Figure 2-10 a, b). Then assuming the equations (2-31) and (2-32) the magnitude of the events is estimated (Figure 2-11c, d). Note that new approach of LPXT method provides an estimate of seismic moment (not moment magnitude) assuming given values for the couple $\Delta\sigma$ and v_r. We can also use it to estimate the moment magnitude (M_w) in cases where $\Delta\sigma$ and v_r are known "a priori" for the region of interest. Or assuming the world-wide used constant values $\Delta\sigma = 3\ MPa$ and $v_r = 0.9\ V_s$. Note that these are average values, with a relatively large standard deviation, accounting for heterogeneity in the source process. Now, since seismic moment is better estimated from long-period data (regional, teleseismic P-S or surface waves) this method can be also used to determine the effective stress-drop, assuming the values of M_0 (long-period data) and v_r (theory).

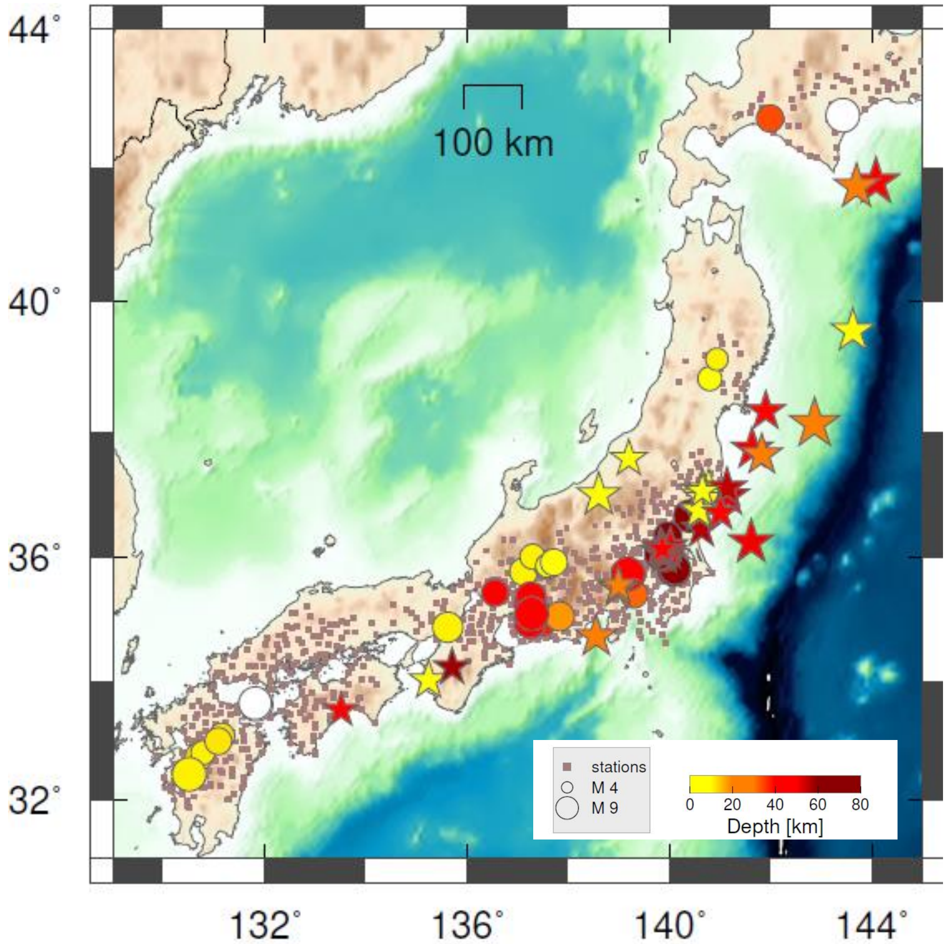

Figure 2-9: Japanese Dataset. The distribution of stations (small squares) and 43 selected events (coloured stars) in magnitude range 4 to 9 [*Colombelli et al*., 2014]. The distribution of new selection of Japanese dataset added in this study, magnitude ranging from 2.5 to 4 are shown with coloured circles.

In order to have an independent estimation of seismic moment with this method the MRF' half-duration is determined $T_2/2$ from another observed physical quantity, that is the corner time of the LPXT curve, *e.g*. the time at which the curve reaches the plateau and the MRF its maximum.

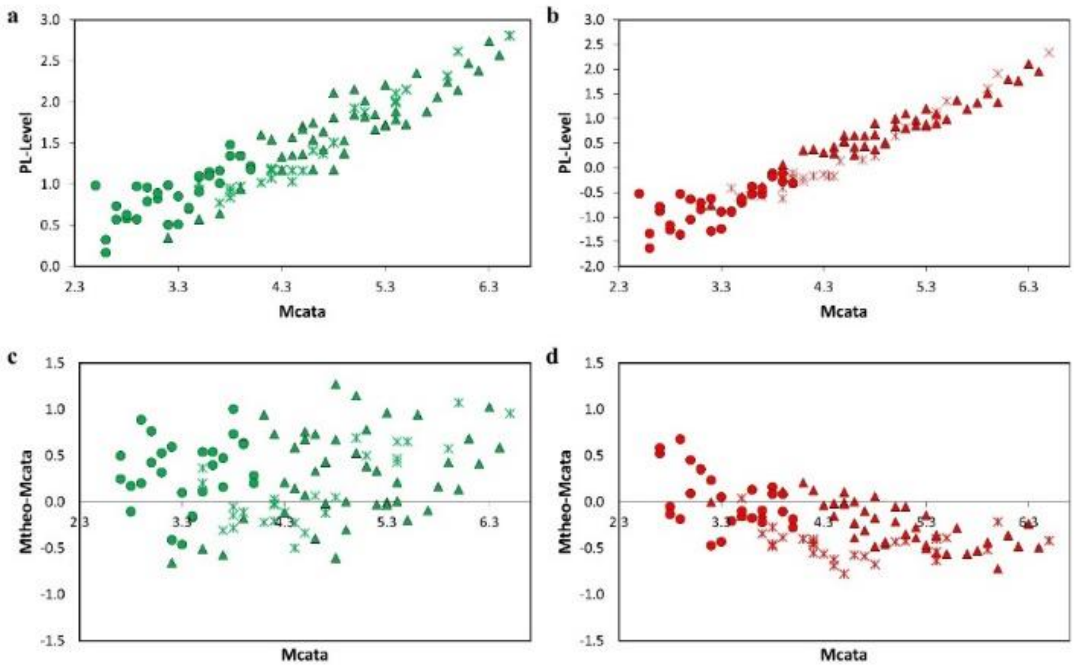

Figure 2-10: a. Plateau level of the LPVT curves. **b.** Plateau level of the LPDT curves. **c/d.** Residual plots of the calculated magnitude (Mtheo) with reference to catalogue magnitude (Mcata). In all panels, stars refer to Italian dataset, circles and triangles refer to new selection and previous dataset of Japanese events, respectively.

CHAPTER 3

Evolutionary Ground Shaking Prediction: The Case Study of 2016, Mw 6.5 Norcia Event

3.1 Introduction

The seismological agencies after occurrence of the earthquake, along with all required parameters, have also reported the level of ground shaking resulting from the earthquake using a typical map known as ShakeMap to assess the vulnerability and seismic hazard. ShakeMap combines expected theoretical spatial distribution of ground motion of an earthquake and observed data as reported by instruments in order to produce what is called shaking intensity sometimes called instrumental intensity. This precision will make a pertinent distinction with macroseismic intensity which is related to building collapse. Normally various classes of shaking are represented through this kind of maps like peak ground acceleration (PGA), peak-ground velocity (PGV), response spectral acceleration (SA), or ground-motion shaking intensity. ShakeMap is determined using the shaking parameters measured from stations in the seismic networks and conversion relations between PGM and the intensity scale [*Wald et al.*, 1999; *Faenza and Michelini* 2010, 2011]. Note that although ShakeMap does not carry information about the parameters describing the earthquake source, different relevant parameters to source like seismic moment and mechanism are the key issues to produce it.

Following the main aim of this chapter which is implementation of a prototype to include the P-wave based extended source in EEW and rapid response applications, we use the relevant algorithms to simulate the extended source and then investigate the evolutionary ground shaking as it is shown in Figure (3-1). Indeed, the final ShakeMap is combination of three values: observed values of PGA/PGV; predicted values from empirical scaling relationships; and predicted values from synthetic seismograms.

In this regard, we first obtain the P-wave based earthquake source model, as the P-waves are progressively available at the recording near-source stations, for the selected case-study *i.e.*, the Norcia earthquake. With the aim of reducing the uncertainties on the ground shaking prediction, the refined kinematic source model will be used for the computation of synthetic seismograms and corresponding ShakeMap. Note that all approaches presented here are expected to provide complementary images of the source and independent estimates of different parameters involved in the rupture process.

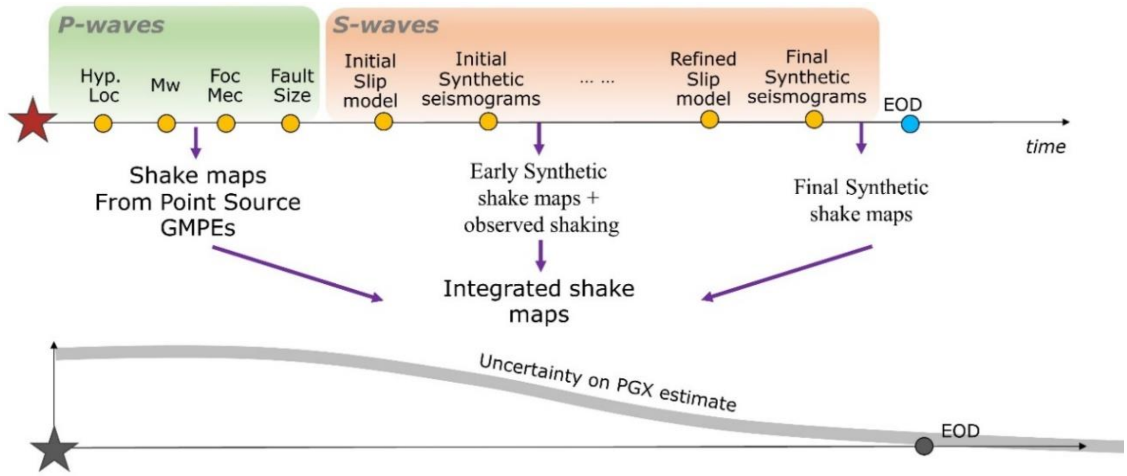

Figure 3-1: Evolutionary preducing the ShakeMap starting from point-source approximation to final refined source model. As soon as more data are available, the uncertainty is reduced.

The refined methods will be designed for the near real-time inverse/forward modelling of the kinematic rupture, in which the geometry and extension of the source are mapped and continuously updated to reconstruct the fault slip history from the signals and to predict the space-time ground shaking evolution. The idea is to use all available signals at each recording station. This means that, at each time, some stations may have the PGV already recorded and other stations may have not yet triggered the event or may have recorded a small portion of the P-wave.

To this purpose, the present chapter summarizes the evolutionary algorithms starting with some simplifications like the point-source approximation which is a typical describtion of the source in real-time and near real-time applications. This simplification is fully insufficient specially for large events with magnitude above 6 and may result in symmetric and circular expected shaking, thus reducing the effectiveness of the EEW systems. In the other hand, assuming the point-source approximation to model the rupture source is one of the limitations of the standard EEW approaches. Therefore the extended seismic source is charactrized and all calculations will be promptly used to evolutionary update the shaking predictions in the near-source.

Another fundamental source parameter to prepare ShakeMap, is the focal mechanism that should be taking into account. The focal mechanism is normally provided at later time by the agencies using complex inversion of waveforms for the determination of moment tensor components.

3.2 Rapid and Evolutionary Seismic source Description

For a given earthquake, in real-time and near real-time applications, the source is simply described as a single point, often providing unrealistic ground shaking distributions as it is shown in Figure (3-2a). In EEW standard approaches, this kind of description of the source is very common, for instance, it is used through the PRESTo in southern Italy.
Next, after estimating the relevant mechanism and geometry in EEW time scale, the kinematic rupture model, in which the geometry and extension of the source, is continuously updated to reconstruct the fault slip history and to predict the space-time ground shaking evolution. So, the shaking map in the region surrounding the area of earthquake nucleation is updated (Figure 3-2b). Noteworthy, three main concepts are combined to design and develop the updated ShakeMap, *i.e.*, the attenuation law based on the distance from the fault, the first observed data and preliminary kinematic source forward modelling.
In this step, the fault geometry is constrained combining the classical scaling laws and the mechanism early solutions. To model the source description, we use the fast source parameter estimates already presented in chapter 2 *i.e.*, the LPXT method, which is, in turn a measure of the source length, assuming a near-triangular moment rate function. Then, a single patch slip distribution is imposed, and its extension and position with respect to the nucleation are controlled by the size estimates from LPXT method and by preliminary directivity estimates, respectively. At the same time, the best fault plane solution mechanism and, possibly, the dominant rupture direction is estimated as well. To find the earthquake focal mechanism, we use the result published by *Tarantino et al.*, [2019] based on the evolutionary and automatic algorithm, using the absolute P-wave peak amplitudes, corrected by the geometrical attenuation effect.
Then at the Rapid-Response time scale (from minute to tens of minutes), the first kinematic low-frequency source descriptions are computed and the shaking can be re-computed with more detailed forward modelling and more data. Note that the accuracy of the shaking prediction is increased through time, as a more complete description of the source properties will be available (Figure 3-2b, c). In this perspective view, in the following sections, all evolutionary steps for the case study, Norcia earthquake, is presented.

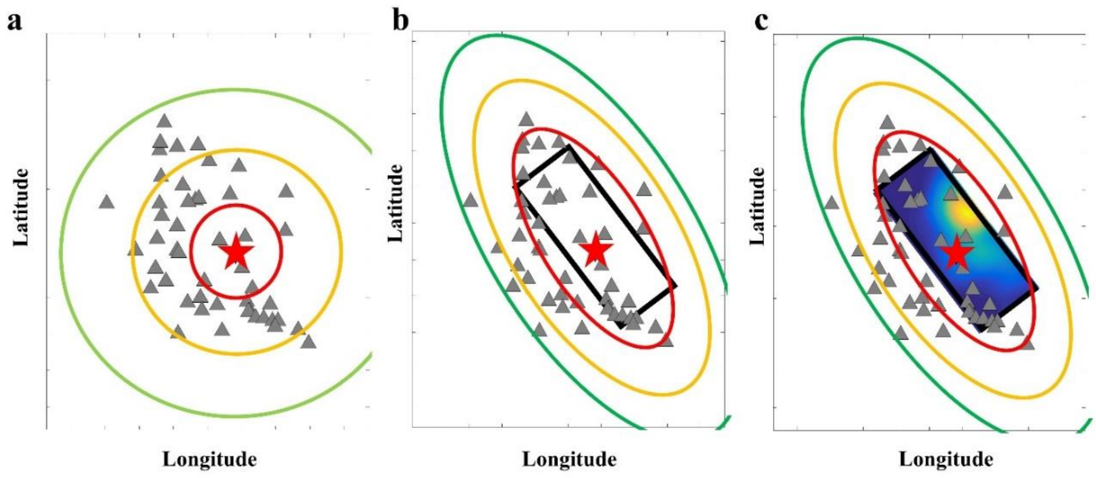

Figure 3-2: a. Point source approximation and circular symmetry (circles) of the expected shaking around the point source (red star). **b.** Extended source model and new expected shaking contours. **c.** The previous model with slip model. In all panels, the gray triangulars represent the distribution of seismic stations.

3.3 Case Study, the 2016 Norcia event

We analyze the October 30th, 2016, Norcia event, the largest earthquake with magnitude 6.5, in 2016-2017 seismic sequence occurred in central Italy, one of the most active seismic area in Italy. Within 36 years, since the 1980 Irpinia earthquake, this sequence constitutes the largest release of seismic energy in Italy, and since the 2009 L'Aquila earthquake, the Norcia event is the largest earthquake. As it is also explained in chapter 2, the sequence started with M_w 6.0 earthquake (occurred on August 24th, 2016, hypocentral depth about 8 km), and during about 30 months long, more than 100,000 aftershocks struck the area including four large events shown in Figure (2-6a). The >1000 km^2 area affected by deformation is involving a volume of about 6000 km^3 and the relocated seismicity is widely distributed in the hanging-wall of the master fault system and the conjugate antithetic faults [*Bignami et al*., 2019].

This event occurred on hypocentral depth about 7 km, in 5 km north-east far from Norcia with epicenter location of 42.83 and 13.11 degrees for latitude and longitude respectively (INGV report,). The largest azimuthal gap in station distribution as seen from epicenter is about 19 degree. The event has been recorded in 250 stations that the epicentral distances of the closest and farthest ones are about 0.065 and 5.26 degrees respectively. The causative fault is a normal faulting mechanism and the main shock ruptured the ~20 km long segment that had remained unbroken after the previous large events [*Cheloni, et al.,* 2017]. The observed PGA map of this event has been shown in Figure (3-3).

3.3.1 Preliminary Source Geometry

Fast estimate of the rupture extension is computed using the LPXT method by analyzing the variation of the peak amplitudes within different P-wave time windows. Note that all information of the source properties obtained from the LPXT method are infered based on a simplified circular fault model and a constant rupture velocity. The obtained estimate is interpreted as the radius, a, of the main patch of fault slip for events as large as the Norcia earthquake. Then, the radius is used to constrain the smaller dimension of a rectangular fault plane model, width W, as most of the low frequency radiation comes from the main slip asperity [*Wells and Coppersmith*, 1994].

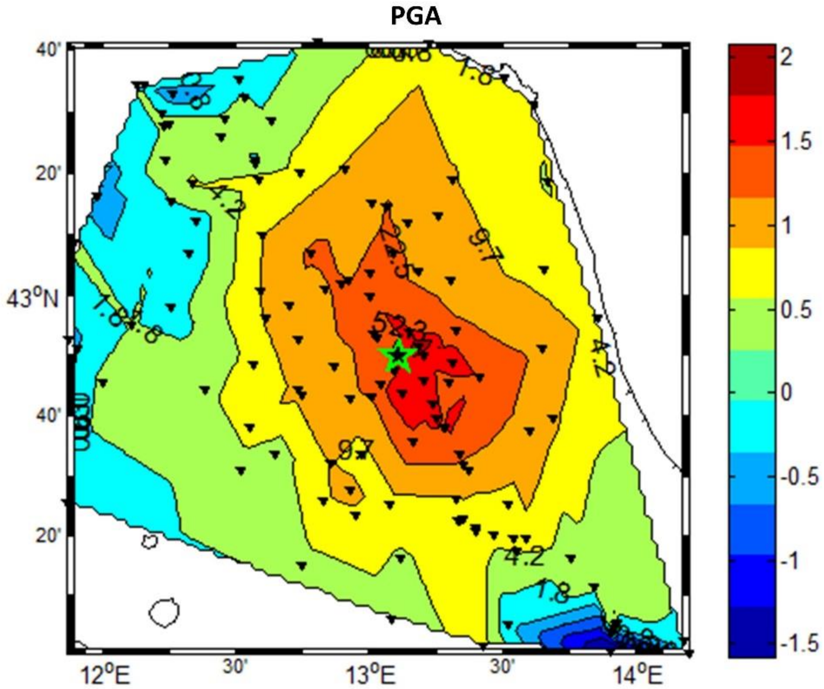

Figure 3-3: The PGA map of Norcia earthquake combining stations observations (shown by black triangles) and the assumed decrease with respect to the epicentral zone.. The coloures refer to log (100*PGA/g) in range of -1.5 to 2, while the numbers are 100*PGA/g ranging from 0.8 to 52.3.

For Norcia earthquake, the estimated radius, a, is about $5.04\ km$ [*Nazeri et al.*, 2019] and therefore the width is imposed about $W = 10.08\ km$. Thus, a rectangular fault plane oriented according to the focal mechanism has been built which is centered around the hypocenter. Moreover, the half-duration of the apparent source time function is determined using LPXT algorithm about 2.44 s.

On the other side, to provide stable solutions of the focal mechanism, we use the result published by *Tarantino et al.*, [2019] based on the azimuthal variation of the P-wave amplitude and possibly including some prior constraints. Few seconds after the origin time, the strike and rake reach to the stable solution, while providing the reliable solution of dip as a less stable parameter takes more time about 7 seconds. It is also important to notice that using this method, discriminating the real focal mechanism to the auxiliary plance is not possible on the typical involved time scale. For the mentioned case study, the following stable solution of the focal mechanism is reported in an off-line test: strike = 155°, dip = 56°, rake = -95° [*Tarantino et al.*, 2019].

3.3.2 Early ShakeMap Based on Early ShakeMap Based on Ground Motion Prediction Equations (GMPE)

The strategy that we follow to check the timely improvement of the prediction accuracy is systematically comparing the real PGV with the predicted ones from GMPEs (the Ground-Motion Predicted Equations [*Akkar and Bommer*, 2007]) at the location of the real stations. The *Akkar and Bommer*, [2007] equation for peak ground velocity (PGV) in cm/s is expressed as below functional form:

$$\log PGV = -1.36 + 1.06\,M - 0.079\,M^2 - (2.95 - 0.31\,M)\log\sqrt{R_{jb}^2 + 5.55^2} \tag{3-1}$$

where S_S and S_A take the values of 1 or zero for soft ($V_{S30} < 360\ m/s$) and stiff soil sites or rock sites being defined as having $V_{S30} > 750\ m/s$; similary F_N and F_R take unitary value for normal and reverse faulting earthquakes respectively, otherwise zero.
The prediction Error (PE) at each station used for this comparison is mainly calculated using two parameters: 1. the logarithm of the ratio between observed and estimated PGV and 2. the Variance Reduction (VR), normalized L-square norm of the PE parameter.

$$PE_i = log_{10}\left(\frac{PGV_{real}^i}{(PGV_{est}^i)}\right) \tag{3-2}$$

$$VR = \frac{\sum_{i=1}^{N} \|PE_i\|^2}{\sum_{i=1}^{N} \left\|log_{10}\, PGV_{real}^i\right\|^2} \tag{3-3}$$

These parameters are investigated using different earthquake source models, either from the single point of nucleation or from three different fault models (Figure 3-4). Note that to calculate the PGV values using GMPEs, the proper distance is considered as: the epicentral distance for point source model, the minimum between the *Joyner and Boore*

[1981] distances for the double fault case (Figure 3-4b) and the *Joyner and Boore* [1981] distance for the single fault cases (Figure 3-4c-d).

Along with assuming the point-source approximation (Figure 3-4a), the fault geometry has been first modelled by means of the focal mechanism and width W automatically extracted through the previously described techniques and imposing a double length with respect to the *Wells and Coppersmith*, [1994] scaling law to consider either unilateral and bilateral rupture (Figure 3-4b). The doubled length of the fault plane allows to place in a random position the main patch of slip. Second, we only consider the realistic focal mechanism removing the auxiliary plane (Figure 3-4c). Then, the third model is defined using more realistic geometry as inferred from a source low-frequency imaging [*Pizzi et al.,* 2017]. VR values estimated for all source models presented in Figure (3-4) are reported in Table (3-1).

Assuming the point-source approximation, clearly show a systematic underestimation of the PGV with reference to the observed values (Figure 3-5a). While, it is obvious that there is an effective improvement of the prediction as more detailed geometry of the source are available (Figure 3-5b-d).

Table 3-1: VR values estimated for all source models presented in Figure (3-4).

Source Models	VR
Point-source approximation	0.09
Early geometry with auxiliary plane.	0.05
Early geometry without auxiliary plane.	0.04
Fault geometry inroduced by *Pizzi et al.,* [2017].	0.03

3.3.3 Synthetic ShakeMap

Contemporary to these first GMPEs estimates the procedure develops some source kinematic models. As location, magnitude, focal mechanism and size of the fault are avaliable and by using a simplified low-frequency description, we define a set of stocastic source models investigating the epistemic uncertainty though the variation of location and amplitude of high-frequency slip asperities following a k-square approach, the rupture velocity, the rise time and the directivity in terms of reciprocal position of the hypocenter with respect to the main slip asperity. A similar set may be also defined later, on a rapid response time scale, when a low-frequency model is computed, including defined directivity and low frequency slip modelling. From this set of models the synthetic seismograms are computed at real stations and virtual nodes and the relative peak ground velocity are extracted.

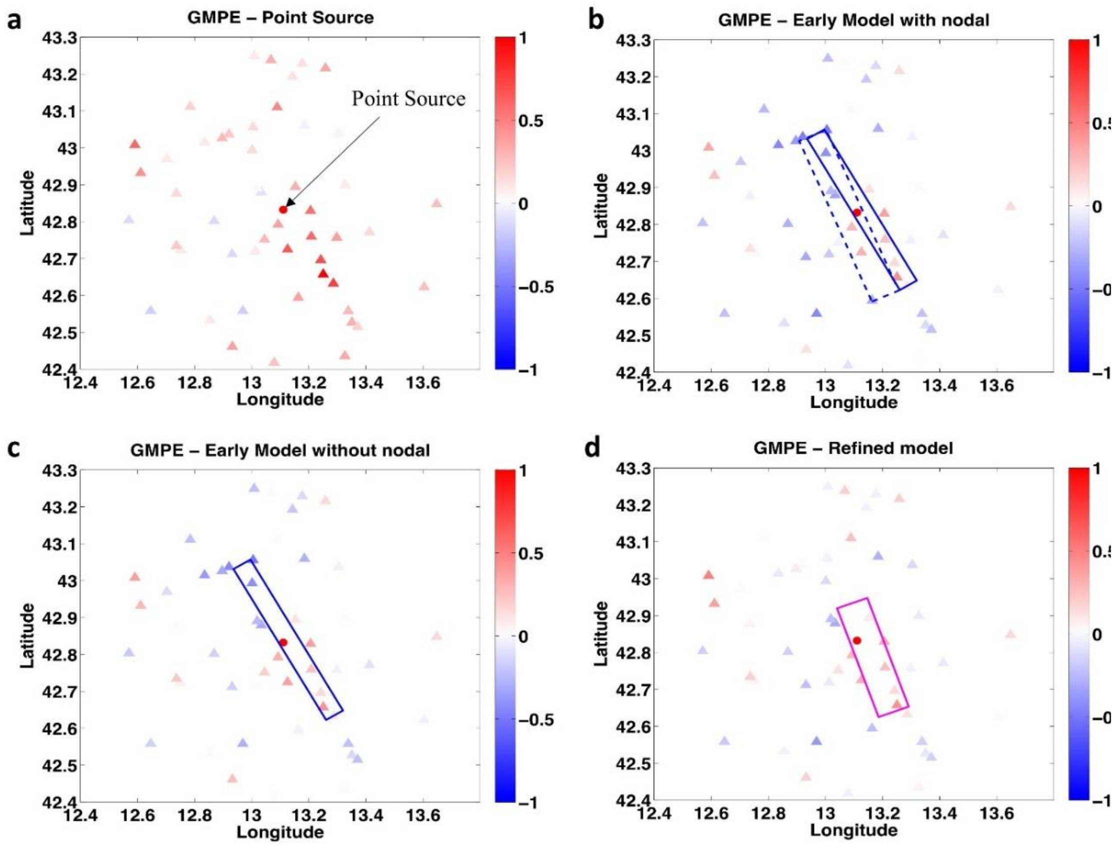

Figure 3-4: Prediction Error estimations considering an attenuation from different source models **a.** Point-source approximation **b.** Early geometry with auxiliary plane, **c.** Early geometry without auxiliary plane, **d.** Fault geometry inroduced by *Pizzi et al.*, [2017].

To model the extended source, the fault has been discretized in 23936 sub-sources in a 150 m spaced regular grid. Considering a rupture propagating at about 3 km/s, this would allow to model the generated signal up to $\sim 4\ Hz$ properly describing the smallest wavelength with at least 5-6 points. Also an inhomogeneous rise-time has been imposed on the sub-sources and each of the rise time value is extracted from a Gaussian distribution having a mean of 0.6 s; the rupture velocity is varying in an iterval from 65% to 80% of the of the S-wave velocity in the medium. A linear ramp has been implemented as source function. The justification to these choices can be found in *Scala et al.*, [2018].

Finally, the slip amplitude distribution A is defined, over a length L, summing a low-frequency Gaussian model (Figure 4-5a, top), to describing the main slip patch, and a stochastic k^2 distribution [*Herrero and Bernard*, 1994; *Scala et al.*, 2018] to honor the shorter wavelength source contributions (Figure 3-6a, middle). The center of the Gaussian slip is randomly extracted from a uniform distribution and the other sub-sources having $A \neq 0$ are located at a distance $d \leq L/2$ with respect to this center. In Figure (3-6a, botomn) and (3-6b) the final stochastic slip distribution and its projection onto the Earth's surface are presented respectively.

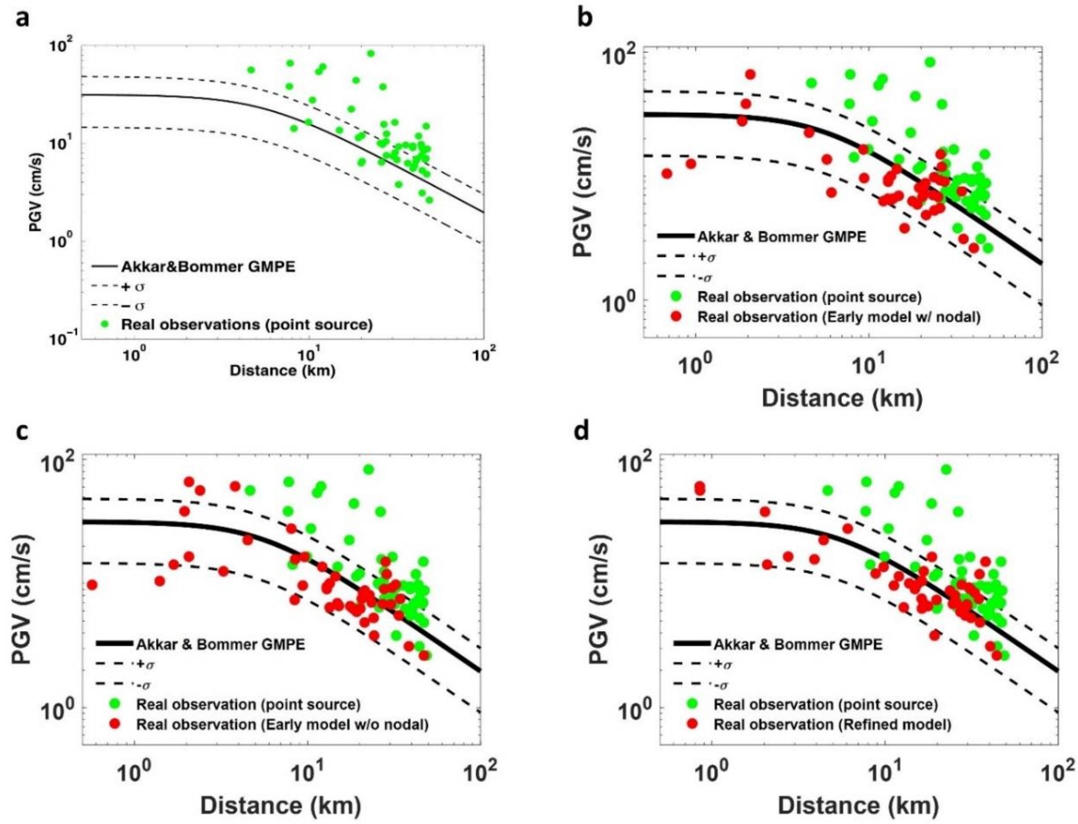

Figure 3-5: Comparision between the extrapolated data PGV: green points for point source model and red points for the refined model (observed PGV but the distance are computed from the preliminary fault model) in all panels, with predicted values (black line) assuming the *Akkar and Bommer* [2007] emprirical equations for all source models presented in Figure (3-4) respectively.

The synthetic seismograms are computed assuming a 1D velocity-model for wave propagation [*Ameri et al.*, 2012]. This allows to efficiently compute the Green's function in the frequency domain solving the wave propagation equation through the reflectivity method. This approach is efficiently implemented in the AXITRA code and in the first part of the LinSlipInv code (http://fgallovic.github.io/LinSlipInv/).

The synthetic seismograms are computed at the location of 51 real stations that recorded the Norcia event. The epicenter of the event (red star) and the stations (green triangles) are plotted in Figure (3-6b).

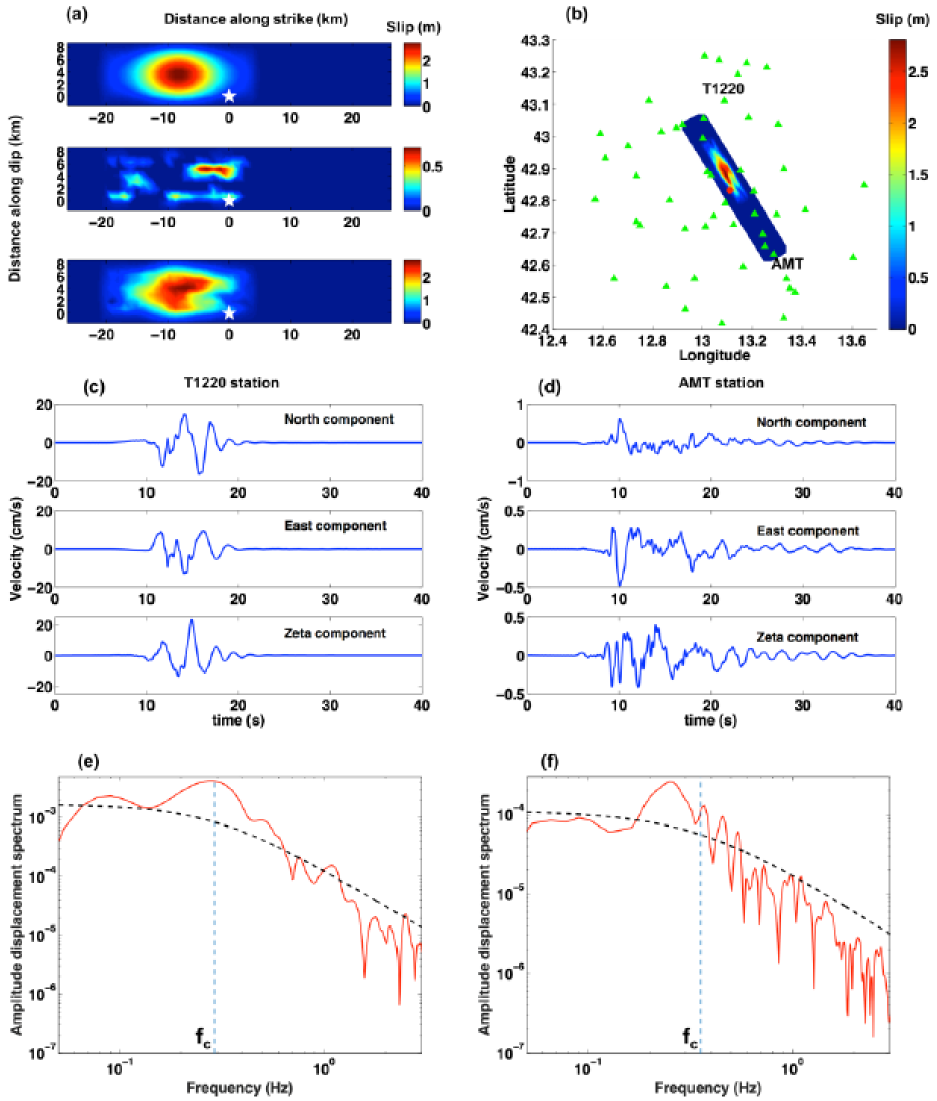

Figure 3-6: a. Scheme of the k^2 modelling of the source: on the top the Gaussian low frequency distribution, in the middle the stochastic distribution of the shorter wavelength slip asperities, on the bottom the final model as the summation of the low and high frequency descriptions. **b.** Projection onto the Earth's surface of the fault plane used in the forward model. On the fault projection the slip distribution is plotted. The red dot and the green triangles represent the epicenter and the used stations respectively. The texts refer to the stations whose synthetic traces are plotted in the panels **c** and **d**. (**e-f**): the amplitude displacement spectra for the same stations of panel **c** and **d**. The spectra are inverted through a classical f-2 fit (black dashed lines) and the corner frequencies are extracted (blue dashed lines) [RISSC-Lab, the report 28.3 of the SERA project]. Note that the final corner frequency is extracted from velocity spectra.

The three-component signal at the stations T1220, and AMT (see the text within the Figure (3-6b)) are showed in Figure (3-6c-d). With respect to the main patch of the slip, they represent the synthetic velocity traces at a directive and an anti-directive station, respectively. Finally, in Figure (3-6e-f) the amplitude displacement spectra for the same stations in the panels (c-d) are plotted for the vertical component. The corner frequency ranges from 0.15 to 0.35 for the stations on the directive and anti-directive direction are considered in the analysis respectively.

Figure (3-7) shows similar analysis as the one for GMPE-ShakeMap in Figure (3-4). Here the estimated PGVs are considered as the median of the PGVs from each set of simulations. What we observed here is that the best results are surprisingly obtained for the early kinematic models in particular in the case for which we are able to resolve the focal planes ambiguity. When the low-frequency model is included and hence the main propagation directivity is univocally modelled, the variance reduction significantly increases.

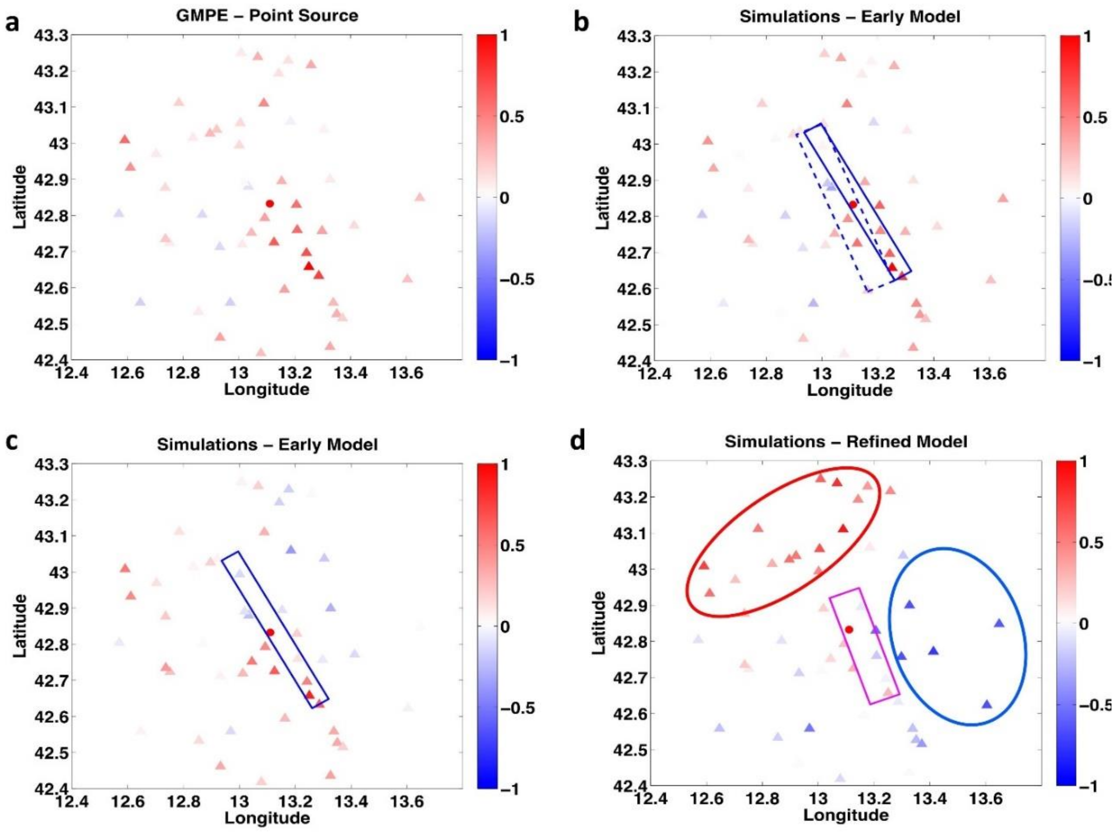

Figure 3-7: Prediction Error estimations using source model simulations for **a.** Point-source approximation **b.** Early kinematics with auxiliary plane, **c.** Early kinematics without auxiliary plane, **d.**

Refined kinematics without auxiliary plane. The ellipses represent a pathological behaviour described in the text.

In this model, the issue is related only to few stations, in particular to the very high coherency of the up-dip propagation that generates a systematic overestimation of the shaking on the footwall, and to a negligible shaking computed on the along-strike antidirective direction always too low as compared to the real observation. For all the other stations we noticed a significant improvement in particular along the along-strike directive direction. More efforts should be devoted to improve the simulation modelling possibly including a k^{-2} based rise-time distribution and a more complex propagation model, eventually accounting for a 3-D velocity model [*Del Gaudio et al.*, 2015; *Gallovič and Brokešová*, 2004; *Herrero and Bernard*, 1996].

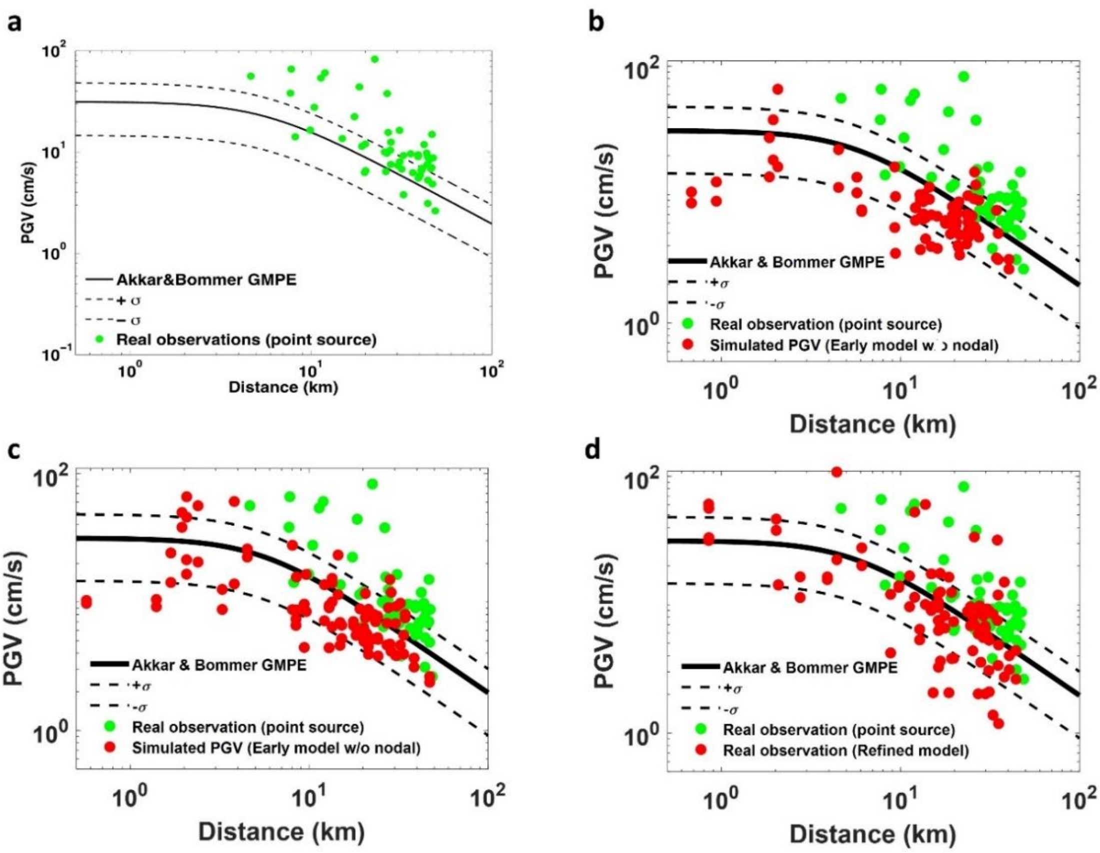

Figure 3-8: Comparision between the observed PGV (green points) with predicted values (black line) assuming the *Akkar and Bommer* [2007] emprirical equations for all source models presented in Figure (3-7) respectively.

Similar to the GMPE ShakeMap, Figure (3-8) shows the estimated PGV for all source models presented in Figure (3-7) and comparing again with observed values (green circles) and the predicted values (black line) assuming the *Akkar and Bommer* [2007] empirical equations. Note that in this Figure, the red dots refer to the observed PGV but the distance are computed from the preliminary fault model.

Box 3-1: Uncertainty estimates for the different models

This uncertainty is given by the GMPEs sigma for all the GMPEs predictions while it can be computed through the sigma of the PGV distributions in the case of kinematic simulations. In this histrogram we plot the GMPE's sigma along with the simulation sigma at the real stations for the early and refined source kinematic models. It is evident that the unmabiguous modelling of the directivity achieved in the refined model, leads to a significantly smaller uncertainty as an effect of the reduction of the epistemic uncertainty

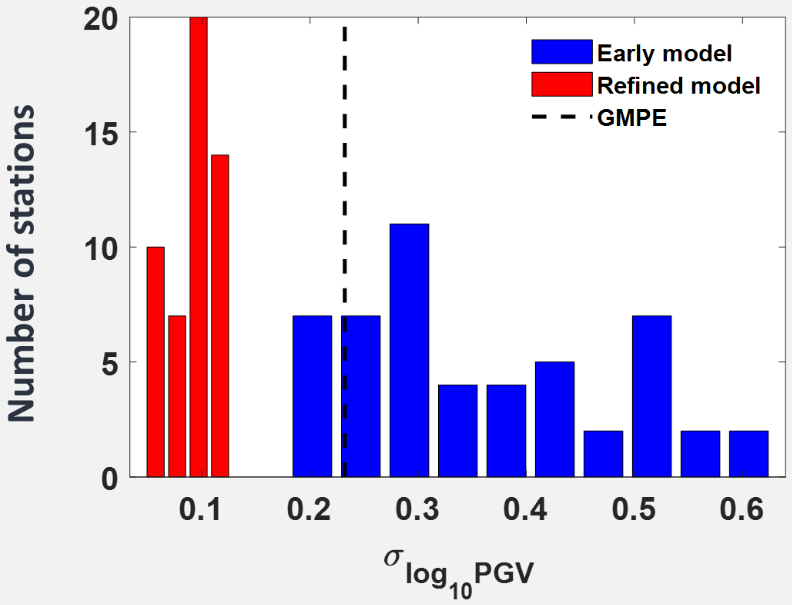

Figure 3-9: Uncertainty reduction for refined model simulations.

3.3.4 Integrated ShakeMap

In particular for this case-study even when the shaking expected values start to converge due to the good coverage of incoming real data the improvement of the uncertainty for the simulated PGV approach is significant and the variances of log(PGV) are smaller down to two orders of magnitudes with respect to those ones from GMPEs. It means that the uncertainty on the shaking Is significantly smaller for the case of simulations. Finally, we provide an overview of the efficiency through the analysis of the blind zones performed by means of the presented off-line test.

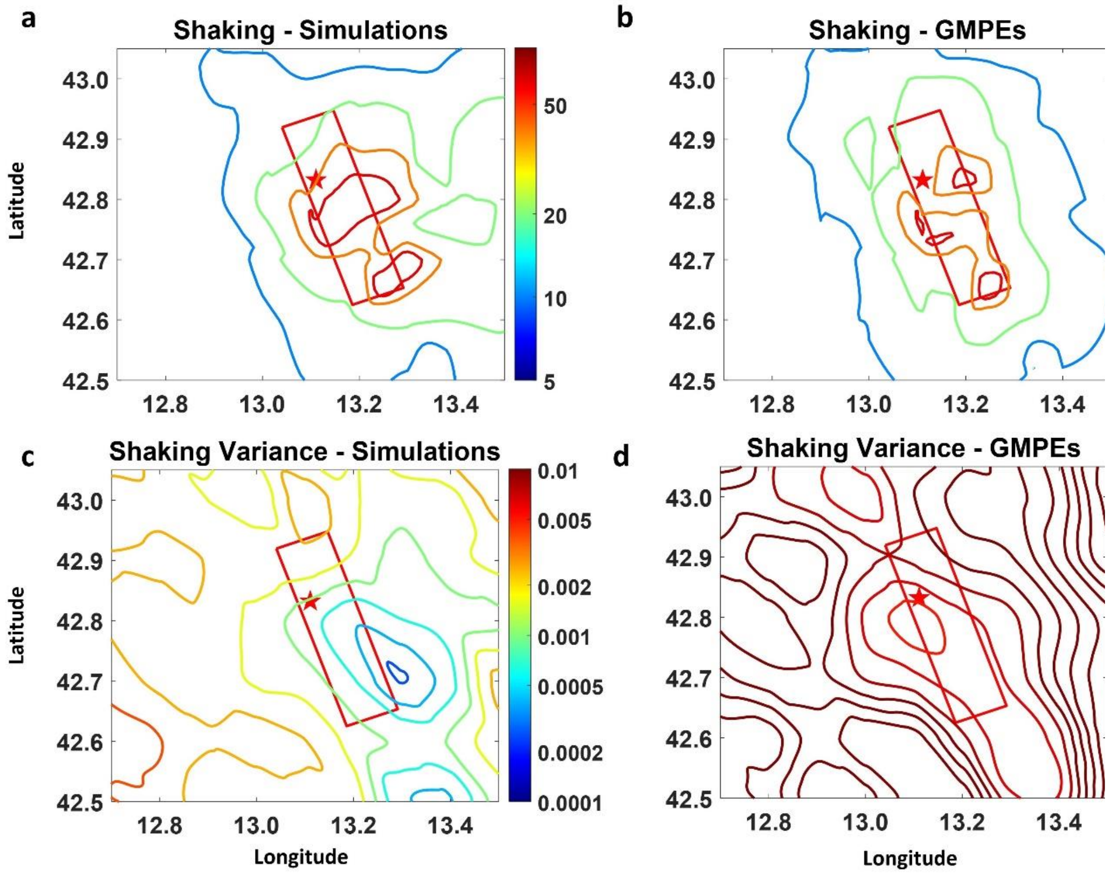

Figure 3-10: Variance from simulations until 2 orders of magnitude smaller

We see that the Early Source description leads to a blind zones only slightly larger than the point source approach making this prototype feasible for an EEWs implementation (Figure 3-10b).

After few minutes, the fast low-frequency description of the faults are available with a blind zone area which it is larger than the near-source. Therefore, this algorithm can be applied for shaking prediction implemented in earthquake early warning approach or rapid response systems.

3.3.5 Conclusions

We have shown that a realistic geometrical description of the fault, based on P-wave analysis can be obtained on typical EEW time scales and how this may improve the shaking prediction with respect to the classical point source approach. Contemporary the procedure uses these estimates to develop source kinematic fast simulations.

From the kinematic simulations the shaking can be estimated and used either along with the GMPEs or eventually replacing them in the Shake Map computation. This would have the advantage to reduce the epistemic uncertainty as an effect of the identification of rupture directivity.

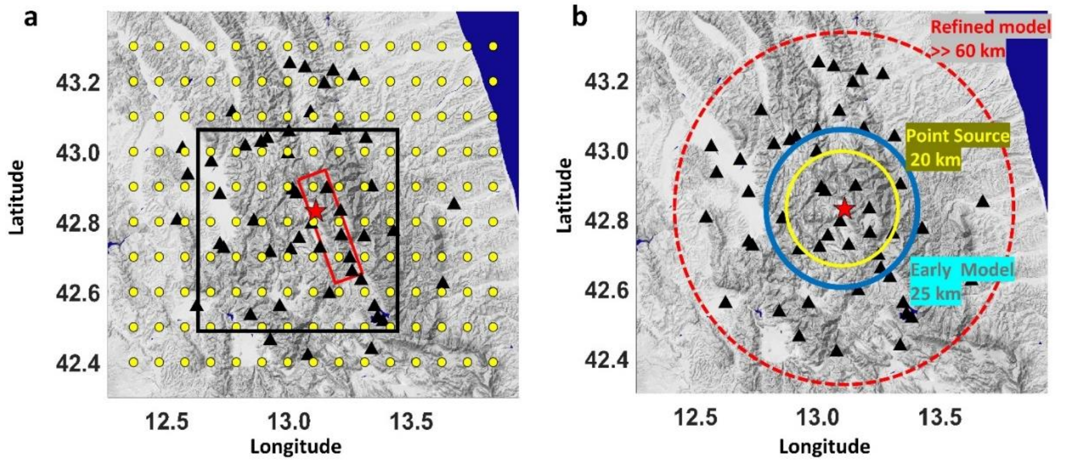

Figure 3-11: a. Rectangular grid point arounf the Norcia hypocenter to evaluate classical ShakeMap approach with either GMPEs or simulation shaking prediction interpolated through real observation. **b.** Results from an off-line test on the Norcia case-study for the different models.

In this sense we should improve the kinematic modelling possibly including different modelling of parameters like the rise time and possibly including 3D propagation models and use techniques for a faster determination of the directivity.

At the end what is still open issue is that:

- Is really needed to obtain a detailed low frequency description of the slip for the current purposes or it can be even roughly modelled as long as we have realistic estimates of the directivity?
- Are the site effects visible in the frequency range used in this study? And how it is possible to consider it in producing the ShakeMap. There are two options to include site effects: i) include a coefficient directly on GMPEs and ii) predict the value at the rock sites and then apply amplification factors (convolution of rock-site by the amplification factor). It is worth to mention that at the moment the site effects are taken into account as a additional term in the GMPEs, thus the same approach can be incorporated in the synthetic PGV approach by adding similar terms to the estimated PGV. The site effects can be also incorporated in terms of convolution in the Green's function computation.

- Another issue refers to addying the uncertainties on synthetic data, similar to what is done for the GMPE. Actually, the finite-fault, rupture kinematic models are used to generate continuously updated, ground shaking maps along with associated uncertainties. The accuracy and uncertainty on shaking prediction will be investigated through parameter variability tests based on real and simulated application case-studies. In fact, uncertainty on the synthetic data is given by the epistemic uncertainty on the source and it should be taken into account that the synthetic PGV is extracting from a set of synthetic (histograms in the box).

CHAPTER 4

Source Mechanism and Rupture Model from the Inversion of a Near-Source Record

4.1 Introduction

Nowadays, simulation is pioneered as a scientific tool in many branches of sciences to reproduce processes under test conditions and actual events. To develop the relevant algorithms, a remarkably complex mathematical process is needed. In seismological community, the numerical simulation of seismic waves is a fundamental tool for seismological studies such as estimation of the heterogeneous velocity structure [*Tape et al.*, 2009; *Chen and Lee* 2015], study of seismic source processes and wave propagation in the heterogeneous Earth and hazard assessment [*Lee et al.*, 2006; *Imperatori and Gallovič*, 2017; *Frankel and Clayton*, 1986; *Emoto et al.*, 2010; *Graves et al.*, 2010; *Maeda et al.*, 2016].

In this chapter, we simulate seismic waveforms to investigate the source mechanism complexity of August 21, 2017, Ischia earthquake. The main purpose is developing an automatic and fast algorithm to characterize the earthquake source using mathematical techniques to optimize the retrieved model. Assuming the finite-fault model, we apply both forward modelling and inversion technique. Therefore, we simultaneously implement Semi-Newton's and Powell's method (for inversion process), using Programme Axitra developed by *Coutant* [1990] at the University of Grenoble to simulate the seismograms. By applying different criteria and assuming various hypothesis explained in this chapter, the source mechanism and rupture model of this event are simulated from the inversion of a near-source record. Moreover, the methods applied to find the retrieved earthquake source model and then generating the synthetic shake map can be taken into account as an alternative approach for previous algorithms illustrated in chapters 2 and 3.

In summary, in this chapter, after reviewing the Axitra and different inversion methods, we explain in more detail all steps of preparing the synthetic PGV and PGA shakemap from the obtained model.

4.2 Generation of Synthetic Seismograms using AXITRA

Obtaining the synthetic seismograms using Axitra is normally performed in two main steps: first computing the Green's Function (GF) in the frequency domain; and second convolving the GF with the appropriate source time function (see Box 2.1). It means that besides the GF concept (Chapter 2), the theory behind the Axitra is included the discrete wavenumber theory as well. The programme is limited to use a one-dimension velocity model (horizontally structured layers) of the area. While, a complex source defined by its focal mechanism can be considered as an input parameter to run this software and then to simulate the seismograms. Various source time functions are set to the default of Axitra such as dirac, ricker, triangle, ramp, trapezoid and so on.

4.3 Inversion

In general, the geophysical problems can be solved by different algorithms of forward modelling or inversion. Origin of difference between forward and inverse techniques comes from the description of the equation $d = F(m)$, where d is data, m is model parameters and F is an operator representing the relation between data and model. Data is the unknown part of the equation in forward problems, while in the inverse problem contrary to forward modelling, based on the observation data *d*, model m will be predicted by $m = F^{-1}(d)$. In this equation, F^{-1} is the inverse operator. In fact, inversion refers to the different mathematical methods to retrieve all information about subsurface-source physical properties from observed data. In the seismological application of the inverse problem, *m* can be a representative of the source of the earthquake by this assumption that the physical properties of the medium are known. On the other hand, the main objective is to characterize the source from the observed seismic data recorded at the stations.

Box 4.1: Testing Axitra Considering Point Source in Homogeneous Medium

As there is no manual available for Axitra programme, before running for the real data, first we test it with a simple example *i.e.*, a single point source in the homogenous medium. So, the theoretical arrival times of P- and S-waves can be easily checked to understand how the input parameters are to be defined and how Axitra works. Figure (4-1) shows the location of the station and assumed point source. Note that the altitude of the station is fixed at 100 m to avoid free surface effects on amplitude.

To run Axitra, there are four main input files as listed below:

1. “Station” contains the location of the stations.
2. “Source” contains the hypocentral location of all sources.
3. “axi.hist” contains the moment magnitude of the earthquake, strike and dip of the fault plane and rake of the movement.

4. "axi.data" contains the velocity model of the region and all required parameters needed for calculation.

For this simple test, source time function has been selected as a simple triangular with half-duration equals to 0.1 seconds. The output of Axitra since it is chosen as the velocity waveform, is shown in Figure (4-1). We found that both P- and S-waves are cantered at the theoretical arrival time. Thus, as a conclusion, to make the realistic simulation for the arrival time, the half-duration of the source time function needs to be added to the origin time of the event. Note that the arrival time of the phases are also checked by TauP Toolkit.

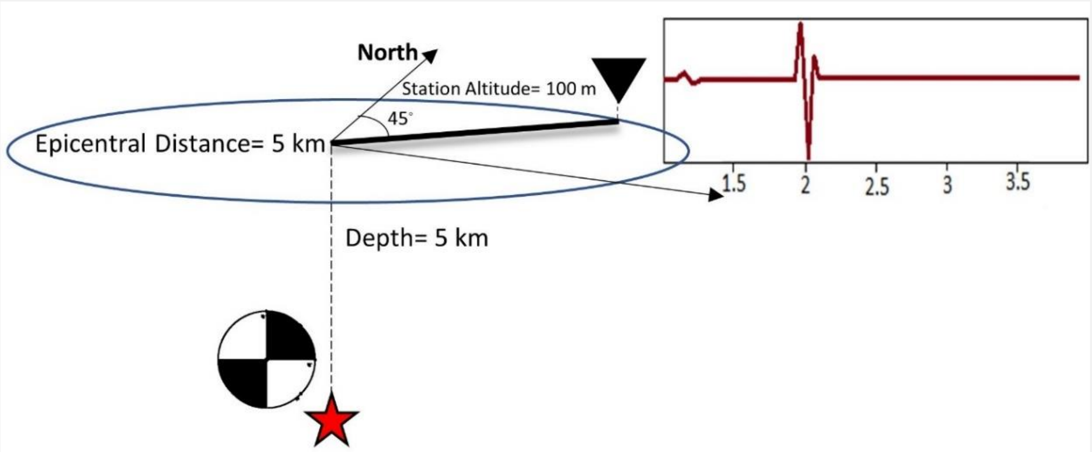

Figure 4-1: A single point source (red star) in the homogeneous medium. The station is shown with black triangle. The velocity waveform simulated at this station is shown with red signal in the box.

In many seismological and geophysical applications, the optimization approaches have found significant use to solve the inverse problem, finding an optimal value of a typical characteristic function (CF) of several variables. For example, CF that should be minimize (or maximize) is a misfit (or fitness) function showing the differences (or similarities) between observed and synthetic data [*Sen and Stoffa*, 1995]. It is also worth to note that most inversion methods follow a general algorithm. For example, for univariate search, it is described as three main steps as below:

1. Make an initial guess.
2. Loop over independent variables one by one, while all other independent variables are fixed, then performing 1D optimization on CF to find extremum for a given variable.
3. In the case of "not converge" go back to the previous step and repeat the process until finding the extremum.

After a few passes through all independent variables, an overall direction becomes apparent which is the direction connecting the starting point to the end point. CF has been chosen as both Root-Mean Square Deviation (RMSD) and Correlation Coefficient (CC), *i.e.* a misfit and fitness functions respectively:

$$RMSD = \sqrt{\frac{1}{N}\sum_{i=1}^{N}\left\|A_i^{obs} - A_i^{syn}\right\|^2} \tag{4-1}$$

$$CC = \frac{1}{N-1}\sum_{i=1}^{N}\left(\frac{\overline{A_i^{obs} - \mu_{A^{obs}}}}{\sigma_{A^{obs}}}\right)\left(\frac{A_i^{syn} - \mu_{A^{syn}}}{\sigma_{A^{syn}}}\right) \tag{4-2}$$

where A^{obs} and A^{syn} are observed and synthetic signals, N is total number of points in the discrete waves, and μ and σ are the mean and standard deviation of the signals, respectively. The equation (4-2) is also known as Pearson correlation coefficient showing a measure of linear dependence and varies between -1 and 1 for negative and positive similarity of the signals.

Among several global optimization methods developed for geophysical problems, for our case study, we apply the Semi-Newton's and Powell's inversion described in the next sections. While the Semi-Newton's method is based on the line search, the Powell's method is an unconstrained nonlinear optimization algorithm.

4.3.1 Semi-Newton's Inversion

The first optimization algorithm considered for this study is the Semi-Newton's method which is perturbative, iterative and linearized inversion. In this method, a quadratic function is locally used to minimize the error function. Indeed, the search direction of Semi-Newton's method at any iteration is calculated by assuming an initial model and its closest neighborhoods in orthogonal directions to find the next minimum point. To better clarify the algorithm, we consider a simple problem with two parameters that they are to be minimized toward the optimized solution. Schematic of this method is simply described in Figure (4-2).

After defining the starting model, the first step is exploring the model parameter space along the orthogonal direction (Figure 4-2b), and then repeat the process considering the new initial model (Figure 4-2c to j). At each iteration, the model corresponding to the minimum FC will be the new initial model for the next iteration. In this method, after some iterations the final model is obtained.

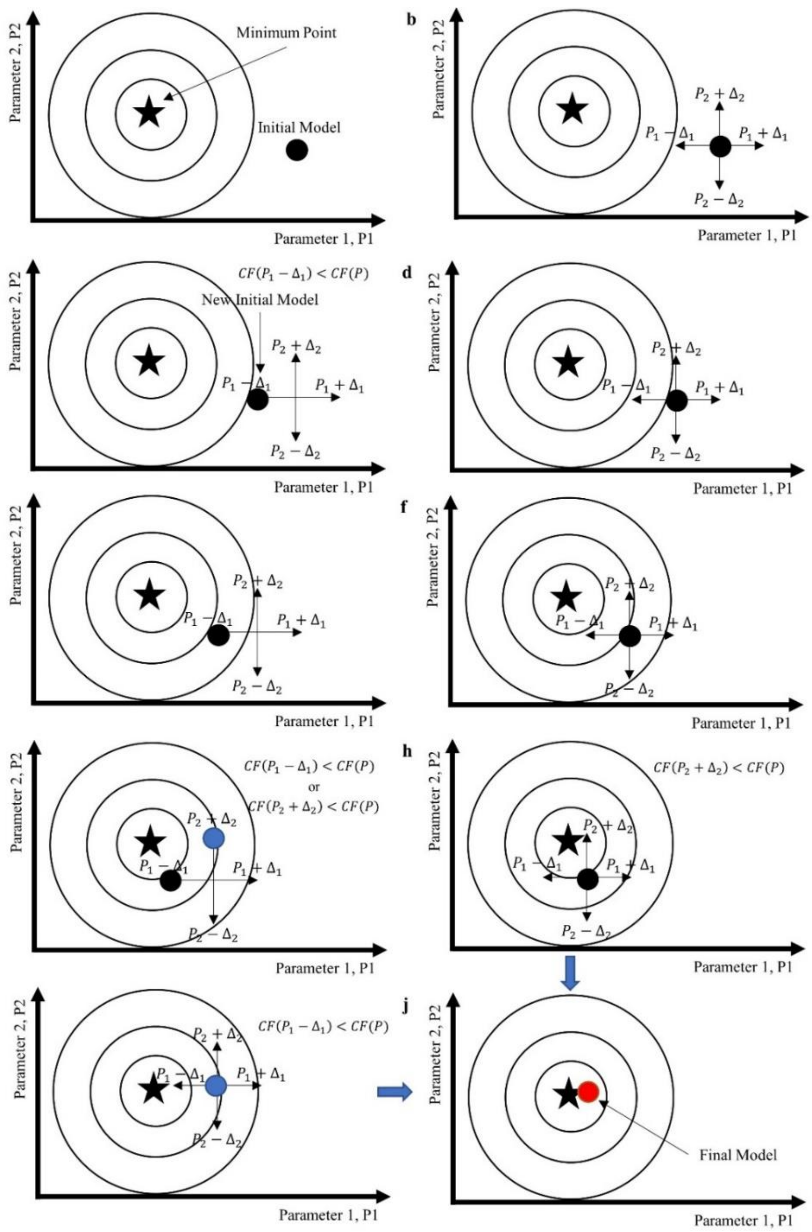

Figure 4-2: The schematic of the Semi-Newton's method. Black star is a real minimum value *i.e*., the solution of the problem. The circles are the cost function isocontour, while the black/blue circle present the model. The final model after some iteration is shown by red circle. More detials are described in the text.

The process is terminated when the procedure reaches a stable minimum value of CF or the estimated parameter values no longer vary. Note that number of iterations and accuracy of the results strongly depend on choosing an appropriate Δ for each parameter. To reduce the uncertainty and error so to increase the accuracy, the process can be repeated by considering the last retrieved model and changing Δ (for example half of the previous Δ).

4.3.2 Powell's Inversion

Powell's inversion method is actually efficient and convergent especially for the quadratic functions. In the category of the numerical optimization methods, the Powell's method is one of the strongest tools to find the minimum value of any multi variable functions, f, of N parameters, $f(x_1, x_2, \ldots, x_N)$. A minimum of the function f is approximated along each of the N variable parameters by this assumption that the partial derivatives of the function are not available. The first step of this algorithm is assuming an initial guess, X_0 and directions along all N parameters. After finding the sequence of points step by step along all directions, the final minimum will be measured. To better understand the theory behind this method, we consider a simple problem with only two variables, P_1 and P_2 (Figure 4-3). Thus, the summary of the process as it is obvious in Figure 4-3 is outlined below:

1. Randomly guess an initial model, X_0 and two directions, h_1 and h_2, along two variable parameters P_1 and P_2 respectively (Figure 4-3a).
2. Performing a 1D optimization along the first direction h_1 starting from X_0 to find the extremum X_1 as a next initial point (Figure 4-3b).
3. Performing a 1D optimization along the second direction h_2 starting from X_1 to find the extremum X_2 as a next initial point (Figure 4-3c).
4. To define the new direction h_3 which is the connection between two previous extremums *i.e.*, X_1 and X_2. This new direction, h_3 is known as the average direction as well.
5. Considering X_2 as a new initial point and repeating the previous steps from 2 to 4. Thus, performing a 1D optimization along the direction, h_3, to find the extremum X_3 (Figure 4-3d).
6. Performing a 1D optimization along the second direction, h_2, starting from X_3 to find the extremum X_4 (Figure 4-3e).
7. Starting at X_4 and again, applying a 1D optimization along the direction h_3 to find the extremum X_5 which is the optimum point (Figure 4-3f).

Note that to minimize the function, two search algorithms, golden ration and Fibonacci are required [*Mathews and Fink*, 2004].

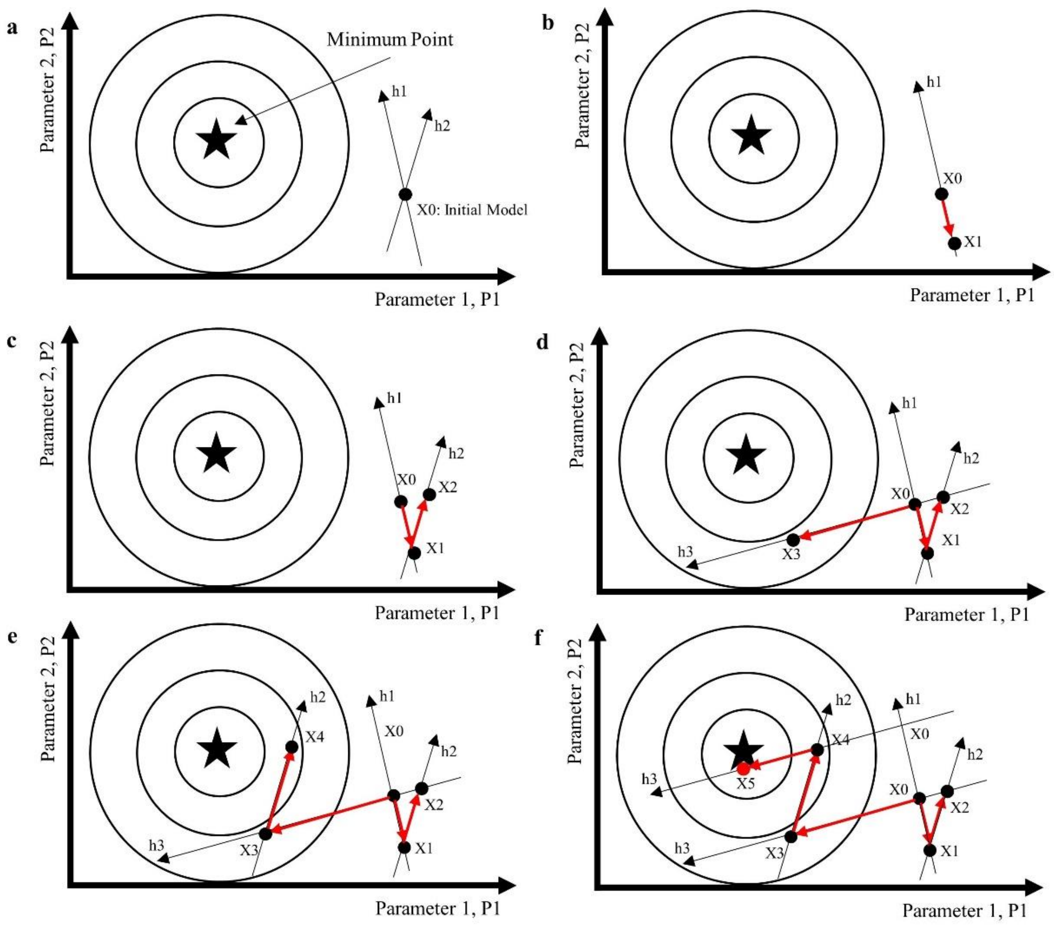

Figure 4-3: The schematic of the Powell's method. Black star is the solution of the problem. The circles are the cost function isocontour, while the black circles present the sequence models. The final model after some iteration is shown by red circle. More detials are described in the text.

4.4 Case Study: The 2017, Ischia Earthquake, Campania region, Italy

On August 21, 2017 a moderate size earthquake occurred at the volcanic island of Ischia located south-west of Naples, Italy, generated a widespread strong ground shaking that caused two victims and several tens of injured people and several buildings collapse in a limited area surrounding the town of Casamicciola in the Northwestern sector of the island (Figure 4-5). As it is listed in Table (4-1), different agencies have reported the location and magnitude of the event with a negligible discrepancy. The event is also well recorded in ISNet (Irpinia Seismic Network) the closest network to the region and the summary of the result about the source properties computed by RISSC-Lab team (Naples Federico II university) is presented in Box 4-2.

Box 4-2: ISNet report for Ischia earthquake.

Here we summarize the results of estimating magnitude and source parameters related to this earthquake issues from ISNet (Irpinia Seismic Network). Figure (4-4) shows the location of the event and all stations belong to the network. Source parameters are computed fixing the location of the event at the epicenter as defined by the INGV (Table 4-1). $M_l = 3.8 \pm 0.2$ is computed using the law provided by of *Bobbio et al.*, [2009], while $M_w = 3.8 \pm 0.07$ and $f_c = 0.53 \pm 0.07\ Hz$ are obtained by the inversion of the displacement spectra [*Zollo et al.*, 2014].

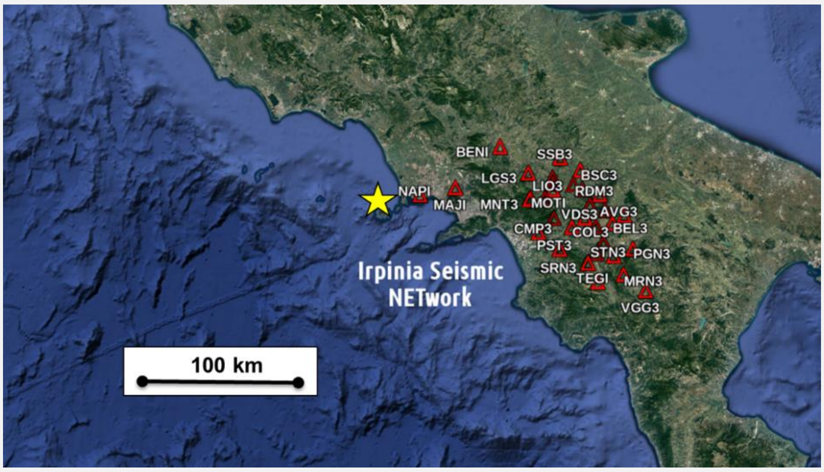

Figure 4-4: Location of the Ischia earthquake (yellow star) with respect to stations (red triangles) belong to ISNet [RISSC-Lab].

Note that this earthquake became an interesting research-topic for many geologists and seismologists, given rise to several publications to describe the earthquake source characteristics and its effects [*De Novellis et al.*, 2018; *Braun et al.*, 2018]. Figure (4-5) represent geological and structural maps of Ischia island [*Sbrana et al.*, 2009; *Acocella and Funiciello*, 1999].

The event has been also well recorded by a three-components accelerometric station (IOCA) operated by INGV located at few hundred meters distance from the event epicenter. To investigate the event rupture complexity and its radiated wave field, in the present work, we use a finite-fault model to invert the near-source velocity records at IOCA station and search for the best-fit kinematic rupture parameters. In this regard, both Semi-Newton's and Powell's optimization methods are implemented from local and global point of views to characterize the source of the earthquake and simulate the seismograms using Axitra.

4.4.1 Introduction and Historical seismicity of the Ischia Island

Ischia is located on the Tyrrhenian margin of Central-South Italy and it is characterized by a resurgent dome uplifted by at least 800 m in the last 33 ka, among the largest resurgence volcanic episodes have ever reported. The island surface is cut by a series of Plio-Quaternary NW–SE- and NE–SW-trending extensional fractures around the resurgent block, which are possibly related to the regional extensional structures [*Acocella and Funiciello*, 2006]. The faults have been formed before resurgence and were partly reactivated during resurgence. The NS and EW-trending fault systems occur at the borders of the dome and *Acocella and Funiciello* [2006] interpreted them as being directly connected to the resurgence phenomena.

During past centuries, the island has been affected by various moderate magnitude events with relatively high macroseismic intensity (IMCS>V; Mercalli-Cancani-Siberg scale) earthquakes (see Figure 4-5). In 1881 and 1883 two destructive events occurred in the area of Lacco Ameno and Casamicciola, current location of the 2017 event, with more than a hundred of fatalities and widespread building collapses in the wide area of Lacco Ameno and Casamicciola [*Del Gaudio et al*., 2019]. The 1883 earthquake reached a macroseismic Intensity IMCS X at the epicenter in the town of Casamicciola, with an estimated magnitude between 4.3 and 5.2, and a depth between 1 and 2 km [CPTI15, *Luongo et al*., 2006].

The 2017 mainshock and its five aftershocks have been located using the probabilistic location method of *Lomax et al*., [2000] using the available P- and S- phase pickings. To locate the mainshock only the P-wave arrivals at the three closest stations installed in the island have been used since the signal saturation prevents the accurate reading of the first S arrival.

Table 4-1: list of magnitude and location of Ischia event reported by different agencies.

Agency	Magnitude	Latitude (degree)	Longitude (degree)	Depth (km)
INGV	Md, 4	40.74	13.90	2
USGS	mb, 4.2	40.78	13.95	9.3
EMSC	mb, 4.3	40.78	13.90	10
MOS	mb, 4.5	40.75	13.82	10
NEIC	mb, 4.3	40.83	14.00	10

GFZ	mb, 4.0	40.77	13.87	10

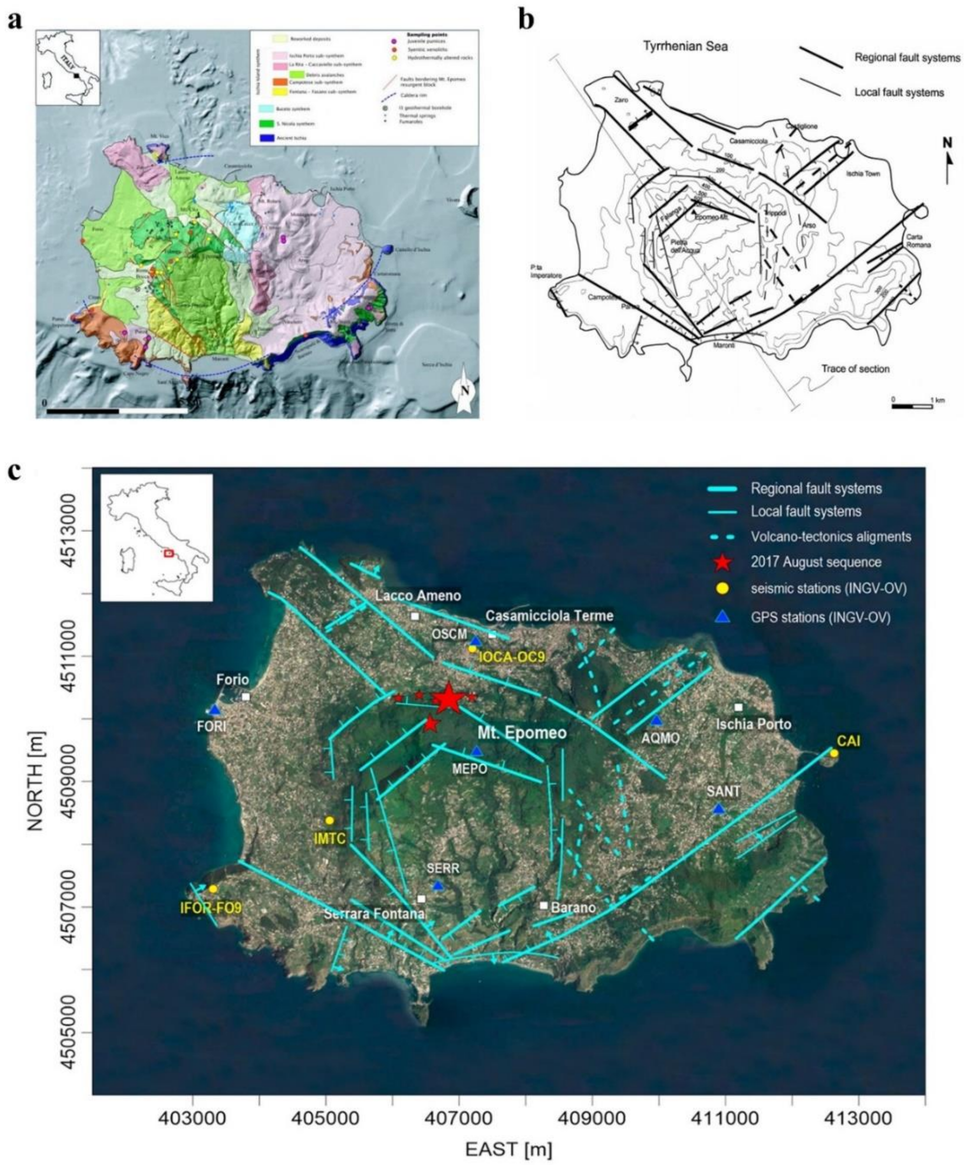

Figure 4-5: a. Geological sketch map of Ischia island [*Sbrana et al.*, 2009], **b.** Structural map of island [*Acocella and Funiciello*,1999]. **C.** Location of stations used in this study (IOCA, CAI, F09), are shown by triangle, while the epicenter location of the main event reported by INGV is shown by red star.

A 3D velocity model built upon previous tomographic studies of the extended Neapolitan volcanic area has been used for the computation of theoretical arrival times. We note that the first P-arrivals at coastal stations (distances larger than 10-20 km) are primarily head waves from the shallow crustal discontinuities, in particular from the interface separating the volcanic sediments and the limestone formation, whose morphology and depth is not known accurately. This uncertainty on the velocity model can seriously affect the earthquake location and focal mechanism determination.

Braun et al., [2018] re-evaluated the Ischia mainshock earthquake location by using the P-wave particle motion observed at IOCA station, evaluation of rotated spectra, and S-minus-P travel time, yields a hypocenter depth of 2 km and a location 0.5-1km south-west of IOCA, in the same epicentral area of the 1883 devastating earthquake. The reported epicenter locations of *Braun et al.,* [2018] and *De Novellis et al.,* [2018] are consistent while their depth estimates differ of about 1 km. *De Novellis et al*., [2018] analyzed and proposed the earthquake mechanism by exploiting seismological, GPS, Sentinel-1 and COSMO-SkyMed differential interferometric synthetic aperture radar coseismic measurements.

A number of significantly discrepant solutions for the focal mechanism of the Ischia mainshock are available as inferred from the inversion of P-wave polarities at local distances or moment tensor inversion at regional distances. A comprehensive review of the different published solutions is provided by *Braun et al.,* [2018], who further applied the combined spectral and time domain method of *Cesca et al.,* [2013] to determine the earthquake moment tensor. Their result shows both large negative isotropic and compensated linear vector dipole (CLVD) components which led the authors to suggest the occurrence of a complex rupture process, with an initial shallow normal-faulting event that triggered a subsequent shallow underground collapse.

Based on the INGV hypocenter depth and focal mechanism solutions, *De Novellis et al.,* [2018] proposed a model of the 2017 Ischia earthquake mechanism as generated by an E-W striking, south dipping normal fault, with a hypocenter located at a depth of 800 m. This solution was mainly constrained by the modeling of DinSAR and cGPS data assuming that they recorded the co-seismic ground deformation.

The joint inversion of the DInSAR and cGPS coseismic measurements constrained the fault plane geometry and allowed to retrieve the associated slip distribution, showing a main patch of slip (max amplitude 14 cm) located at the center of the fault plane at the hypocentral depth.

The strike of the fault has been found roughly consistent with an apparent aftershock alignment along the E-W direction and with the computed focal mechanism from regional seismic waveforms. However, the authors pointed out a main difference between the seismological and geodetic modelling solutions, with an important strike-slip component of the first which is not present in the second one.

The prompt availability of InSar data for the Ischia earthquake allowed to rapidly constrain the source location and mechanism of the event despite of the uncertain early estimations provided by seismological data. Nevertheless, the InSar data modelling assumed that the detected ground displacement was primarily generated by the co-seismic contribution of the causative earthquake fault. Recently, *Albano et al.*, [2018] revisited the InSar data from the Ischia event and investigated the possible contribution of earthquake-induced landslides to the detected ground displacements. Based on the limit equilibrium method, they estimated the spatial extent of the earthquake-induced landslides and the associated probability of failure. Their results show an area of partially overlapping with co-seismic ground displacement retrieved by InSAR data, which led to the conclusion that "the observed ground displacement field is the combination of both fault slip and surficial sliding caused by the seismic shaking" [*Albano et al*., 2018].

The 2017 earthquake seismic impact on buildings and structures of the island has been assessed through a series of surveys conducted immediately after the event by the RELUIS-DPC team (DPC, 2017) Terremoto isola di Ischia: l'attività di assistenza alla popolazione e verifiche agibilità, http://www.protezionecivile.gov.it/media-comunicazione/comunicati-stampa/dettaglio/-/asset_publisher/default/content/terremoto-isola-di-ischia-l-attivita-di-assistenza-alla-popolazione-e-verifiche-agibili-2 (in Italian) and INGV-ENEA team (Azzaro R, Del Mese S, Martini G, Paolini S, Screpanti A, Verrubbi V, Tertulliani A (2017) QUEST-Rilievo macrosismico per il terremoto dell'isola di Ischia del 21 agosto 2017, Rapporto interno. https://ingvterremoti.files.wordpress.com/2017/08/casamicciola-report-prelimquest.pdf (in Italian)).

Del Gaudio et al., [2019] reviewed the in-situ observations of the damage state of masonry and RC buildings in the epicentral area and matched them with simulated damage scenarios built upon the data from the 15th national census of the population and dwellings (ISTAT) converted into vulnerability classes. The latter are expressed according to the classification of the European Macrosismic Scale (EMS-98). In evaluating the seismic damage scenarios, the macro-seismic intensity shake map of the 2017 Ischia event is reconstructed using an interpolation method based on QUEST macro-seismic survey data [*Azzaro et al*., 2017]. The map shows an anisotropic distribution of intensities, with highest values in the SE and SW directions from the epicentral area, with the former having a more pronounced and extended lobe.

The present work has been primarily motivated by the availability of an unprecedented and high-quality strong-motion record in the near-source distance range (less than a 1 km epicentral distance) of a moderate size and shallow depth event at the Ischia island whose high-frequency refined modelling could bring new insight on both extended fault and rupture mechanism. Indeed, previous modelling of the IOCA waveform in de *Novellis et al.,* [2018], mainly concerned the low frequency band (0.1-2 Hz) and assume a point-source earthquake approximation.

The anomalous duration (about 4 sec) of the large amplitude, velocity and displacement waveforms observed at station IOCA (Figure 4-6), as compared to the expected (about 1 sec) source duration of similar size events [*Wells and Coppersmith*, 1994], suggests a possible coupling effect of the very shallow earthquake rupture and wave propagation across the near-surface sedimentary layers which could have contributed to amplify and time extend the ground shaking and hence the event damaging effects.

Here we mainly adopted a two-step modelling procedure where we first analyze the low-frequency (0.05-0.5 Hz) band-pass filtered waveforms to constrain the hypocenter nucleation, the fault geometry and slip, assuming a point-source earthquake mechanism. In this phase, a refined flat-layered velocity model is determined through a forward modelling of the low-frequency velocity and displacement records at IOCA station. Then the accurate P and S-P times at the available stations on the island have been used to define a circular area around IOCA where we search for the best-fit rupture nucleation location and fault mechanisms.

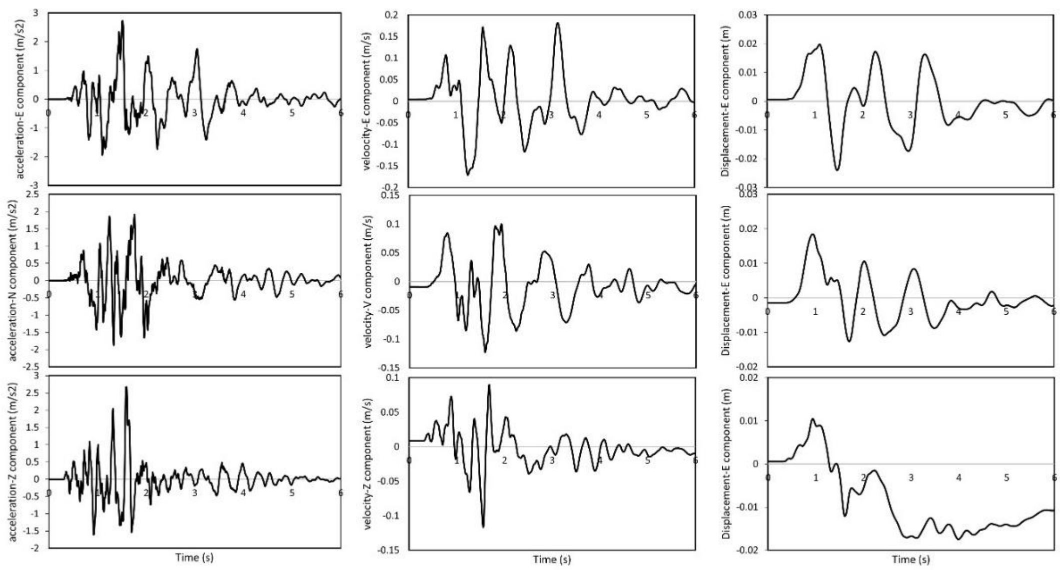

Figure 4-6: Left-column: The 6 seconds acceleration waveforms recorded on IOCA station, E (top), N (middle) and vertical components (bottom) respectively. **Middle-column:** Unfiltered velocity waveforms computed by the integration of acceleration, **Right-column:** Displacement records.

The non-linear inversion of the strong-motion record at IOCA station for a line-source kinematic rupture model is combined with the available information from other regional and local stations to provide the rupture length and orientation, the variable slip distribution along the strike and average rupture velocity.

The retrieved rupture model coupled with multi-path reverberations effects related to a thin, low velocity near-surface volcanic sedimentary layer, explains the observed ground motion duration at IOCA and strong shaking amplitudes and intensities recorded all over the island. The actual fault location, mechanism and the spatial correlation between large simulated PGV/PGA zone and the area where the maximum vertical displacement has been determined by InSar images, suggests that the latter is rather associated to locally strong-shaking triggered land-slide phenomena than caused by co-seismic slip.

4.4.2 Data

Seismic waveform data used in this study have been recorded at the three-component accelerometer of station IOCA and velocity sensors of stations CAI and F09 operated by INGV (Figure 4-5c). While the 2017 event has been clearly recorded with unsaturated amplitudes by IOCA station, the recorded waveforms at CAI and F09 stations are clipped after the P onset with clear positive polarity. Considering the location reported by INGV for the event, the IOCA station is located at few hundred meters epicentral distance. The IOCA station has measured a PGA of 0.28 g (both on the EW and vertical component), PGV of 17.8 cm/s and PGD of 2.32 cm, a relatively higher than expected for a M 4 earthquake. Figure (4-6) represent the acceleration (first column), velocity (second column), and displacement (last column in right) signals of the IOCA station. A casual 0.075 Hz high-pass Butterworth filter is only applied to remove the low frequencies after integrating to produce the displacement records. Acceleration and velocity waveforms shown on Figure (4-6) are unfiltered.

4.4.3 Preliminary Assumptions and Input Parameters

Before proceeding to the main part of our analysis for this event, which involves applying both inversion and forward modeling to simulate the rupture properties and so on, first we have to carry out some preliminary steps. One step is relocating the event using Non-Linear Location (NonLinLoc) package [*Lomax et al*., 2000] and evaluating the effect of different Vp/Vs ratio in the range of 1.5 to 2.4. Figure (4-7) presents the output of NonLinLoc package considering various Vp/Vs (1.5 to 2.3). It is clear from this Figure that the shaded area, probable location, tends to north-west of the IOCA station with an average depth about 1 km.

The simulation analysis to predict ground motion is started by considering the point source, and then, it is extended to the line source. Although different extended source models are taking into account, to avoid unnecessary complexities, the extended source is finally set as a line source with 1 km length composed by different point sources.

In our analysis, we use 1D velocity-model consists of four layers [*Capuano et al*., 2015]. *Capuano et al.,* [2015] using various geophysical data *i.e*., Bouguer anomaly data and seismic wave travel times, modeled the shallow crust of the Ischia island. The thickness and P-wave velocity (Vp) of the first layer are about 900 m and 1.7 km/s, respectively. To estimate the shear-wave velocity (Vs), like previous analysis by NonLinLoc, different values of Vp/Vs ratios from 1.5 to 2.4 are evaluated.

Despite the existence of three stations inside the island, we only focuse on the seismograms recorded on the IOCA station as an observed reference to compare with synthetic waveforms trough the quantitative and qualitative procedure. In addition, the source time function is simplified as a triangular with duration of 1 second which is suitable for magnitude 4.

4.4.4 Inversion of the Point Source approach

To constrain the best location of the nucleation of the rupture and relevant focal mechanism, the point source approximation is considered in the circular grid search around the IOCA station. In this step, both inversion algorithms and forward modelling are used in low frequency band of signals (0.05 to 0.5 Hz). At this step, depth and magnitude of the event are fixed to 1.1 km and 4.0, respectively.

The band-pass Butterworth filter [0.05 0.5] Hz is applied to both observed and synthetic waveforms which are compared in the fixed time window equal to 1.7 seconds starting from the P-wave arrival time. The P-wave onset is picked manually for observed records and automatically for synthetic signals by TauP Toolkit. To avoid any probable errors in picking the P-arrival time, aligning both observed and synthetic signals is also controlled by computing the cross correlation and considering the threshold value equal to 0.2 s to shift the records. Two different inversion techniques *i.e*., Powell's and Semi-Newton's inversion algorithms are implemented by minimizing the Root-Mean-Square Deviation (RMSD) as a cost function (FC) computed in two hypotheses: 1. Based on only Horizontal components, and 2. Based on all components.

In this step, focal mechanism of the rupture *i.e*., strike, dip and slip are an unknown parameter. For each point, different focal mechanisms are considered as the initial models (black beach-balls in Figure 4-8d) to run the inversion codes. The obtained focal mechanism is also checked by P-polarity analysis using all three stations inside the island. Figure (4-8a) shows the results of point source analysis where in different colours refer to RMSD values of horizontal components. Obviously, the minimum regions (shown with blue colour) are mostly in north-west and south-east of IOCA station. To more constrain the region, we compute the CC values of all minimum points and evaluate the fit quality of the observed and synthetic waveforms (Figure 4-8b/c). We conclude that the best point as a nucleation of the rupture is located 600 m on west of IOCA with strike-slip focal mechanism, 115, 45, and 145 for strike, dip and slip respectively.

4.4.5 Inversion of the Line Source analysis

Using the parameters concluded from the point-source approach, *i.e*. the best epicentral distance with respect to the IOCA station and focal mechanism, the simulation and inversion algorithms are repeated for an extended source as a line passed from the best point source. in addition, different configurations of the propagation of the rupture, *e.g*. bilateral and unilateral are studied.

Although different configurations are considered for the line source, for the sake of simplicity, we choose a line source composed of only four-point sources. Like the point source analysis, depth is assumed as a fixed parameter of 1.1 km. The unknown parameters are distribution of the moment magnitude among all considered point sources and the rupture velocity as a function of S-wave fixed to 0.92 km/s. The band-pass Butterworth filter [0.05 3] Hz is applied to both observed and synthetic waveforms in a fixed time window equal to 4.0 seconds after the P-wave arrival time. Again, the Powell's and Semi-Newton's algorithms are performed to search the optimum parameters by maximizing the Correlation Coefficient (CC) parameter as a cost function which is a proxy of similarity of the signals. The obtained model and location of the nucleation is also match with the region that historical events occurred in the island (Figure 4-10). Figure (4-10d) depicts the final recovered model of the seismic source. The qualitative comparison between the synthetic and observed (recorded on IOCA station) horizontal waveforms is shown in Figure (4-10b, c).

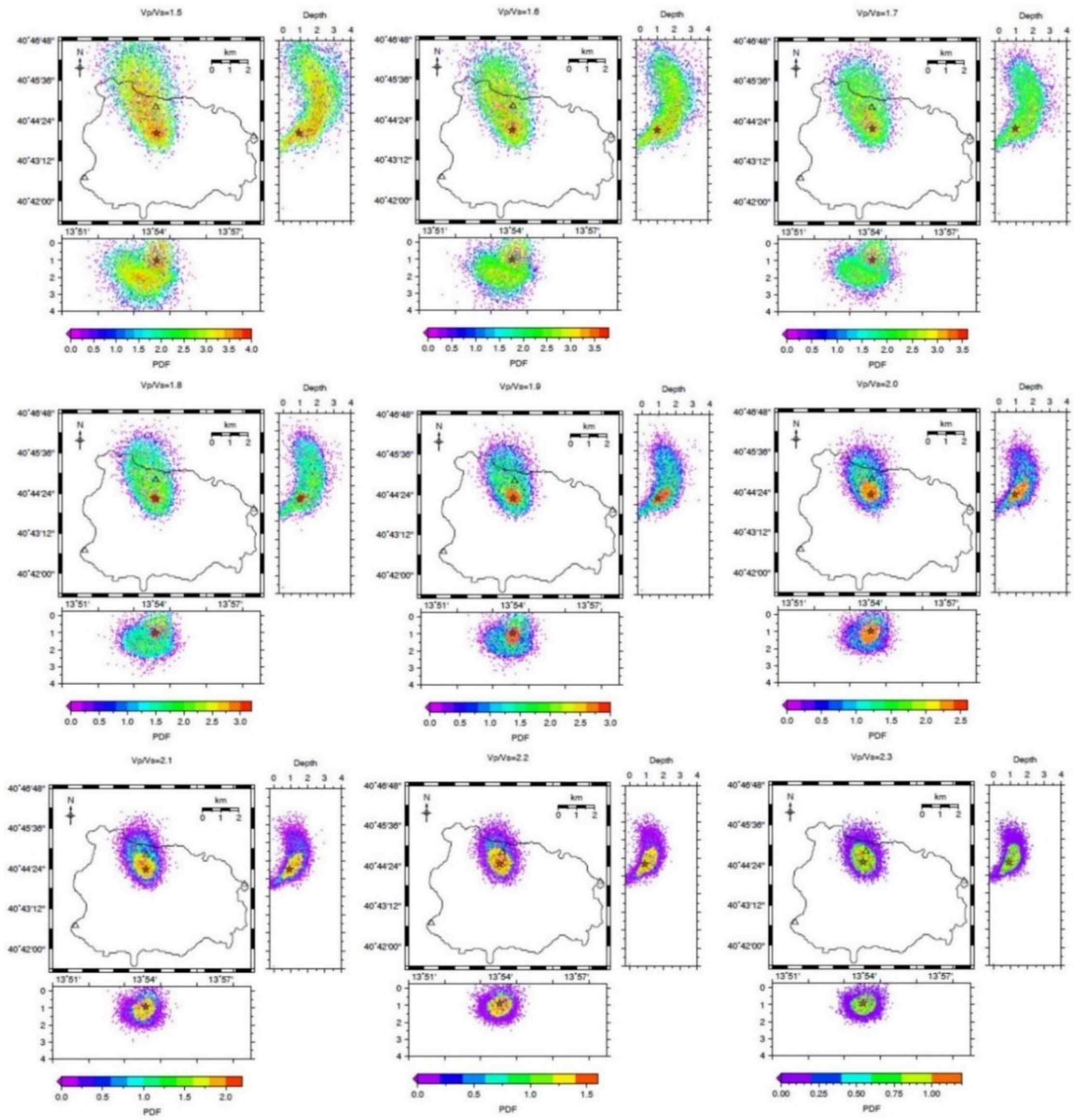

Figure 4-7: The probable location of the event around IOCA station using NonLinLoc software. Here Vp/Vs is varying in the range of 1.5 (top-left) to 2.3 (bottom-right).

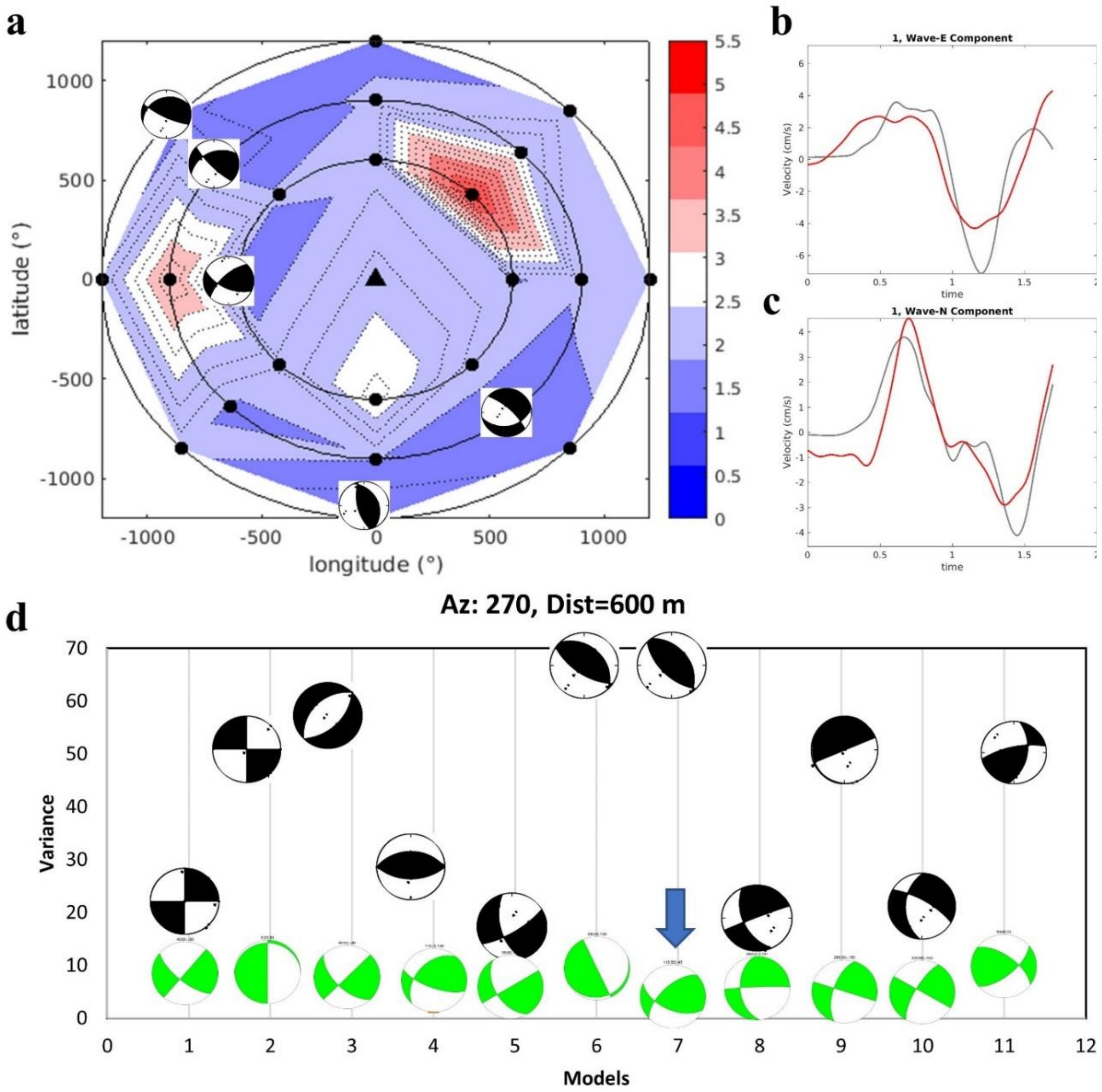

Figure 4-8: a. The output of point source analysis in grid search around IOCA station. Different colors refer to RMSD values computed by using the horizontal components. **b/c.** Fit quality of the observed and synthetic waveforms, b. E component, c. N component. **d.** different focal mechanisms as initial models (black beach-balls) to obtain a stable result (green beach balls).

At the last step of the simulation, for a rectangular grid search around the IOCA station, the synthetic ShakeMap scenario is designed, assuming the final kinematic rupture model and modified 1D velocity-model. Figure (4-9) presents both synthetic ShakeMap scenarios *i.e.*, peak acceleration and peak velocity using horizontal components.

4.4.6 Discussion and Conclusion

Using the program Axitra, assuming the finite-fault model and performing both forward modelling and inversion technique, we simulated the velocity waveforms recorded by the accelerometer IOCA station for the 2017 Ischia earthquake. The first conclusion illustrates to interpret the long last S-wave (4 seconds) which is longer than that expected for any earthquake with magnitude around 4, the initial 1D velocity-model with 4 layers has to be modified to a 6 layers model by adding two shallower layers. The thickness and Vp of the shallow layers are about 75/425 m and 0.4/1.0 km/s respectively, while the Vp/Vs ratio is about 1.8. Therefore, the unexpected duration of the S-wave from theory is due to propagating the waves in very shallow layers with density about 1700 to 1900 kg/m^3.

Inverting the velocity waveforms in low-frequency content up to 0.5 Hz using the point-source approach indicates that the probable nucleation of the rupture is located at 600 m west of the IOCA station with the normal strike-slip fault mechanism. Regarding the final focal mechanism, the fault strike, dip and rake are 115, 55 and 145 degrees, respectively. It is worth to note that the rupture mechanism of this event is a very challenging issue and has been investigated in literatures [*e.g. De Novellis et al*., 2018; *Devotiet al*., 2018; *Nappi et al*., 2018]. However, according to the obtained result in this study, the fault causing the earthquake has a NW-SE direction. Indeed, the rupture starts from west of IOCA and propagates toward south of IOCA.

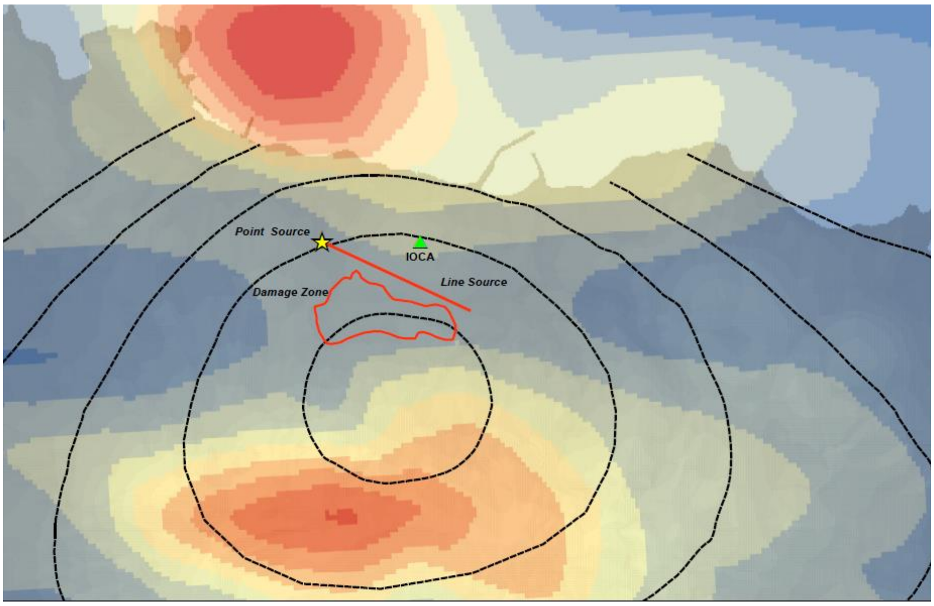

Figure 4-9: Synthetic Shake map, Peak acceleration (%g), of the island considering the retrived model shown in Figure (4-10d).

Among all explored configurations of the extended source according to two nodal planes of focal mechanism, the source of the event is finally modeled by a line source which constitutes four point-sources. With respect to point-source approach, the extended approach is explored in high-frequency content up to 3 Hz. Evaluating the spectrogram of IOCA waveforms demonstrates the lack of high frequencies (more than 2 or 3 Hz) for this event. In addition, according to our observations, the final magnitude and the rupture velocity are about 4.2 and 0.65 km/s, respectively.

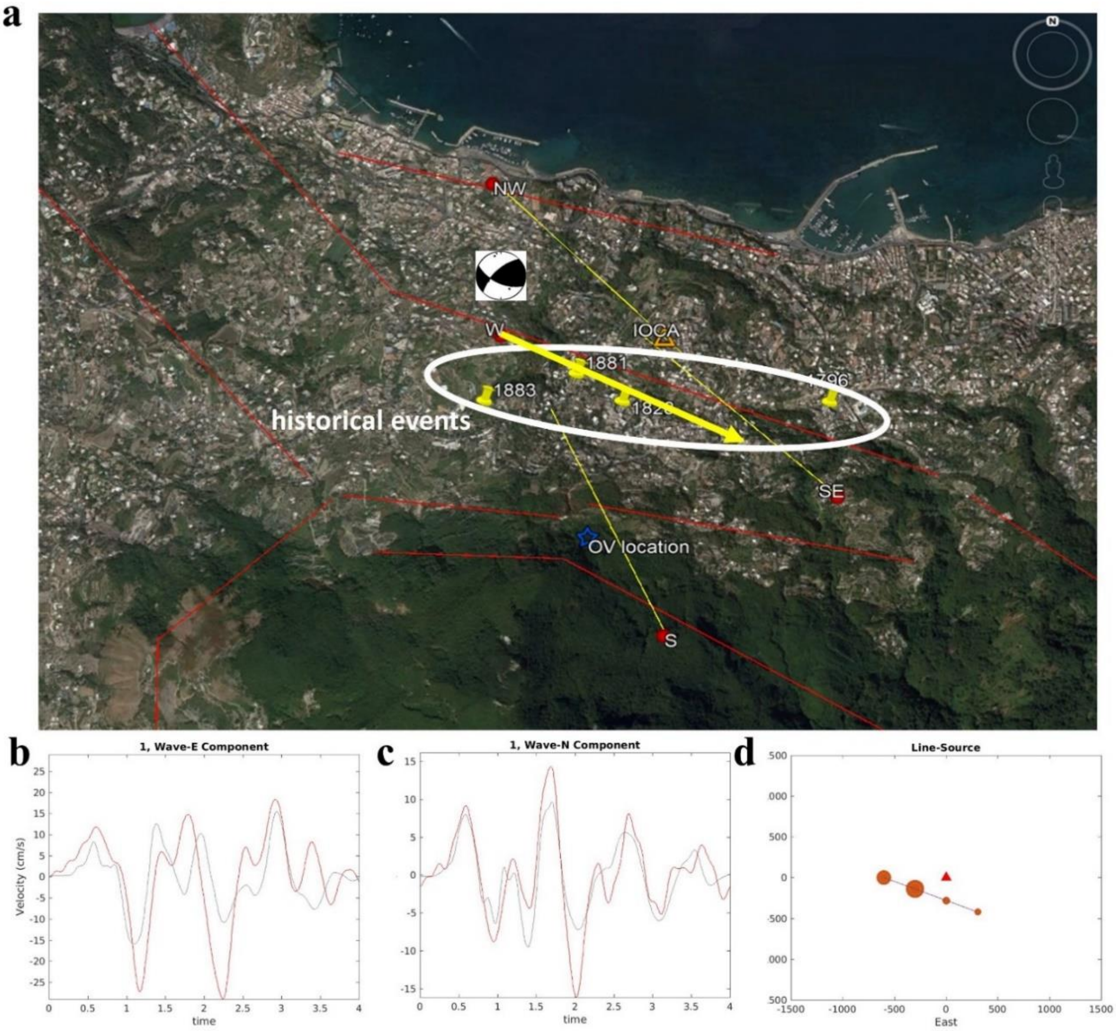

Figure 4-10: a. Location of the nucleation (600 m in west of IOCA) and the final causative (thick yellow line) fault of the event obtained from our analysis. Red Lines are main Faults of the region, yellow Lines are the fault related to the obtained focal mechanism for each point. The historical events are also highlighted on the map. **b/c.** Fit quality of the observed and synthetic waveforms, b. E component, c. N component **d.** final model of the line source. Rupture starts on west of IOCA and propagates toward the south.

Conclusion

This work was done in the framework of SERA infrastructure (Seismology and Earthquake Engineering Research Infrastructure Alliance for Europe, call INFRAIA-01-2016-2017), and JRA 6 (Joint Research Action, "Real-Time earthquake Shaking") projects toward overcoming the limits of the standard EEWS approaches. Main objective of this thesis in principle was to develop, implement and validate efficient algorithms for the real-time signal processing, slip inversion and ground-shaking forecast. In general, the content covers a part of the Earthquake Early Warning and post-seismic Rapid Response which offers valid strategies for real-time and seismic risk mitigation value for the whole community and scientific objectives. Starting from simple representation of the rupture *i.e.*, point source approximation, we could model the extended source of the earthquake and then produce the synthetic shake map to add to the available peak ground information from GMPEs and observed data.

To this purpose, first we developed and tested a methodology for rapid characterization of seismic source including the moment magnitude, dimension and duration of the rupture, and determination of the source kinematic parameters, as well. The proposed method is based on evaluation of the acceleration, velocity or displacement peaks measured on the vertical component of the ground motion in different time windows after the P-wave onset, using the 2016-2017 central Italy seismic sequence.
On the other hand, in the above mentioned project's framework, the other algorithm was developed that can provide stable solutions for focal mechanism based on the azimuthal variation of the P-wave amplitude and possibly including some a-priori constraints [*Tarantino et al*, 2018].
Therefore, using the refined and P-wave based source model and mechanism, we implemented a prototype to investigate the evolutionary ground shaking prediction for an ongoing event. Note that final shake map is integrated of three values including the observed values of PGA/PGV, predicted values from empirical scaling relationships and predicted values from synthetic seismograms.

In addition, parallel to all works done under the mentioned projects, we followed the other algorithm as an alternative approach to simulate the earthquake source and to generate the synthetic shake map using only one station waveforms, while the previous part was mainly network-based analysis. In this part, we tried to promote the continuum between data-based analysis to model-based interpretation. In this regard, the 2017 Ischia earthquake was investigated as a real case study, to determine the kinematic parameters of the rupture by using the inversion of the near-source velocity/acceleration records. The analysis was performed considering both a point source and a linear extended source model.

Although, in this thesis we tried to develop the relevant algorithms to cover some limitations and simplification in EEWS, future research will be involved more considerations. For instance, adding the site effects visible in the frequency range as we already discussed in the third chapters, or characterizing the earthquake source by LPXT method and make it more independent to stress drop and rupture velocity for a given region.

References

Acocella, V. and R. Funiciello, (2006), Transverse systems along the extensional Tyrrhenian margin of central Italy and their influence on volcanism. *Tectonics* **25**, TC2003, https://doi.org/10.1029/2005TC001845.

Acocella, V., and R. Funiciello, (1999), The interaction between regional and local tectonics during resurgent doming: The case of the Island of Ischia, Italy. *Journal of Volcanology and Geothermal Research*, **88**, 109–123.

Aki, K., and P. G. Richards (1980), Quantitative Seismology, University Science Books, Sausalito, Calif.

Akkar S. and J. J. Bommer (2007), Empirical Prediction Equations for Peak Ground Velocity Derived from Strong-Motion Records from Europe and the Middle East. *Bulletin of the Seismological Society of America*, **97** (2): 511–530. doi: https://doi.org/10.1785/0120060141.

Albano, M., Saroli, M., Montuori, A., Bignami, C., Tolomei, C., Polcari, M., et al. (2018), The relationship between InSAR coseismicdeformation and earthquake-induced landslides associated with the 2017 Mw 3.9 Ischia (Italy) earthquake. *Geosciences*, **8**(8), 303.https://doi.org/10.3390/geosciences8080303.

Allen, R. M., and Kanamori, H. (2003), The potential for earthquake early warning in Southern California, *Science*, **300**, 786–789, doi:10.1126/science.1080912.

Allen, R.M., P. Gasparini, O. Kamigaichi and M. Bose, (2009), The Status of Earthquake Early Warning around the World: An Introductory Overview, *Seismol Res Lett*, **80**(5), 682-693, doi 10.1785/gssrl.80.5.682.

Allmann, B. P., and P. M., Shearer (2009), Global variations of stress drop for moderate to large earthquakes, *J. Geophys. Res*., **114**, B01310, doi:10.1029/2008JB005821.

Ameri, G., Gallovic, F., and F. Pacor (2012), Complexity of the Mw 6 3 2009 L'Aquila (central Italy) earthquake: 2 broadband strong motionmodeling. *Journal of Geophysical Research*,**117**, B04308. https://doi.org/10.1029/2011JB008729

Archuleta, R. J. and S. H. Hartzell (1981), Effects of fault finiteness on near source ground motion, *Bull. Seism. Soc. Am*., **11** ,937-957.

Azzaro R., Del Mese S., Graziani L., Maramai A., Martini G., Paolini S., Screpanti A., Verrubbi V., Arcoraci L. and A. Tertulliani, (2017), *QUEST- Rilievo macrosismico per il* *terremoto dell'isola di Ischia del 21 agosto 2017. Rapporto finale*. Rapporto interno, 6 pp., DOI 10.5281/zenodo.886047

Bignami, C., Valerio, E., Carminati, E. *et al.* (2019), Volume unbalance on the 2016 Amatrice - Norcia (Central Italy) seismic sequence and insights on normal fault earthquake mechanism. *Sci Rep* **9,** 4250. https://doi.org/10.1038/s41598-019-40958-z

Bindi, D., Castro, R. R., Franceschina, G., Luzi, L., and F. Pacor (2004), The 1997–1998 Umbria-Marche sequence (central Italy): Source, path and site effects estimated from strong motion data recorded in the epicentral area, *J. Geophys. Res*., **109**, B04312, doi:10.1029/2003JB002857.

Bindi., D., Spallarossa., D., Picozzi, M., Scafidi, D., and F., Cotton (2017), Impact of agnitude Selection on Aleatory Variability Associated with Ground-Motion Prediction Equations: Part I-Local, Energy, and Moment Magnitude Calibration and Stress-Drop Variability in Central, *Bulletin of the Seismological Society of America*, **108,** 1427-1442.

Bobbio A. Vassallo M., and Festa G. (2009), A local magnitude scale for southern Italy, *Bull. Seismol. Soc. Am.* **99**, 2461–2470.

Böse, M., E. Hauksson, K. Solanki, H. Kanamori, and T. H. Heaton (2009), Real-time testing of the on-site warning algorithm in southern California and its performance during the July 29 2008 Mw5.4 Chino Hills earthquake, *Geophys. Res. Lett.*, **36**, L00B03, doi:10.1029/2008GL036366.

Böse, M., T. Heaton, and E. Hauksson (2012), Rapid estimation of earthquake source and ground-motion parameters for earthquake early warning using data from single three-component broadband or strong-motion sensor, *Bull. Seismol. Soc. Am*., **102**(2), 738-750, doi: 10.1785/0120110152.

Bouchon, M. and K. Aki, (1977), Discrete Wave number Representation of Seismic Source Wave Fields, *Bull. Seismol. Soc. Am*. **67**, 259–277.

Braun T., Cesca S., Kühn D., Martirosian J. A. and T. Dahm, (2018b) Anthropogenic seismicity in Italy and its relation to tectonics: state of the art and perspectives. *Anthropocene* **21**, 80–94. https://doi.org/10.1016/j.ancene.2018.02.001

Braun, T., Famiani, D., and S. Cesca, (2018), Seismological constraints on the source mechanism of the damaging seismic event of 21 August2017 on Ischia Island (Southern Italy). *Seismological Research Letters*, **89** (5), 1741–1749. https://doi.org/10.1785/0220170274.

Brondi, P., M. Picozzi, A. Emolo, A. Zollo, and M. Mucciarelli (2015), Predicting the macroseismic intensity from early radiated P wave energy for on-site earthquake early warning in Italy, *J. Geophys. Res. Solid Earth*, **120**, 7174–7189, doi:10.1002/2015JB012367.

Brune, J. (1970), Tectonic stress and spectra of seismic shear waves from earthquakes, *J. Geophys. Res.*, **75**, 4997–5009, doi:10.1029/JB075i026p04997.

Capuano, P., De Matteis, R. and G. Russo, (2015), The structural setting of the Ischia Island Caldera (Italy): first evidence from seismic and gravity data. *Bull Volcanol* **77,** 79. https://doi.org/10.1007/s00445-015-0965-4.

Caruso, A., S. Colombelli, L. Elia, M. Picozzi, and A. Zollo (2017), An on-site alert level early warning systemfor Italy, *J. Geophys. Res. Solid Earth*, **122**, 2106–2118, doi:10.1002/2016JB013403.

Cesca, S., Rohr A. and T. Dahm, (2013), *Discrimination of induced seismicity by full moment tensor inversion and decomposition*. *J. Seismol*. **17** (1), 147–163, doi: 10.1007/s10950-012-9305-8.

Cheloni, D., De Novellis, V., Albano, M., Antonioli, A., Anzidei, M., Atzori, S., Castaldo, R., Casu, F., Cecere, G., De Luca, C., et al., (2017), Geodetic model of the 2016 Central Italy earthquake sequence inferred from InSAR and GPS data, *Geophys. Res. Lett*., **44**.

Chiaraluce, L., Di Stefano, R., Tinti, E., Scognamiglio, L., Michele, M., Casarotti, M., Cattaneo, M., De Gori, P., Chiarabba, C., et al. (2017), The 2016 Central Italy Seismic Sequence: A First Look at the Mainshocks, Aftershocks, and Source Models, *Seismol. Res. Lett*., **88**, 757–771.

Colombelli, S., and A., Zollo (2015), Fast determination of earthquake magnitude and fault extent from real-time P-wave recordings, *Geophys. J. Int.*, **502**, 1158-1163, doi: 10.1093/gji/ggv217.

Colombelli, S., Zollo, A., Festa, G. and M. Picozzi (2014), Evidence for a difference in rupture initiation between small and large earthquakes, *Nat. Comm.*, **5**, 3958, doi:10.1038/ncomms4958.

Coutant, O. (1990), Programme de Simulation Numérique AXITRA, *Rapport LGIT*, Université Joseph Fourier, Grenoble, France.

e Novellis, V., Carlino, S., Castaldo, R., Tramelli, A., De Luca, C., Pino, N. A., et al. (2018), The 21 August 2017 Ischia (Italy) earthquakesource model inferred from seismological, GPS, and DInSAR measurements. *Geophysical Research Letters*, **45**(5), 2193–2202, https://doi.org/10.1002/2017GL076336.

Del Gaudio C., Aquino I., Ricco C. and M. A. Di Vito, (2019), Ischia volcano: the 30-years-long ground deformation database. PANGAEA, https://doi.org/10.1594/PANGAEA.909710

Del Gaudio, S., Festa, G., and M. Causse (2015), Strong motion numerical simulations using the empirical Green’s function method: Applicationto 2009 L’Aquila earthquake. *Geophysical Journal International*, **203**(1), 720–736.

Devoti, R., De Martino, P., Pietrantonio, G., and M. Dolce, (2018), Coseismic displacements on Ischia Island, real-time GPS positioningconstraints on earthquake source location. *Annals of Geophysics*, **61**(3). https://doi.org/10.4401/ag-7656.

Ellsworth W.L. and G.C. Beroza (1995), Seismic evidence for an earthquake nucleation phase, *Science*, **268**, 851–855.

Emoto K, Sato G and T. Nishimura, (2010), Synthesis of vector wave envelopes on the free surface of a random medium for the vertical incidence of a plane wavelet based on the Markov approximation. *J Geophys Res,* **115**, B08306. doi:10.1029/2009JB006955.

Faenza L. and A. Michelini, (2010), Regression analysis of MCS intensity and ground motion parameters in Italy and its application in ShakeMap. *Geophysical Journal International*, **180**, 1138–1152. doi: 10.1111/j.1365-246X.2009.04467. x.

Faenza L. and A. Michelini, (2011), Regression analysis of MCS intensity and ground motion spectral accelerations (SAs) in Italy, *Geophysical Journal International*, **186** (3), 1415–1430, https://doi.org/10.1111/j.1365-246X.2011.05125.x

Festa, G., A. Zollo, and M. Lancieri (2008), Earthquake magnitude estimation from early radiated energy, *Geophys. Res. Lett*., **35**, L22307, doi:10.1029/2008GL035576.

Font Y., Kao H., Lallemand S., Liu C.-S. and L.-Y. Chiao, (2004), Hypocentre determination offshore of eastern Taiwan using the maximum intersection method, *Geophys. J. Int.*, **158**(2), 655–675.

Frankel, A., and R. W. Clayton, (1986), *Finite-difference Simulations of Seismic Scattering: Implications for Propagation of Short-period Seismic Waves in the Crust and Models of Crustal Heterogeneity*, *J. Geophys. Res*, ***91***, 6465–6489.

Gallovič, F. and J. Brokešová (2004), On strong ground motion synthesis with k^{-2} slip distributions. *Journal of Seismology* **8,** 211–224, https://doi.org/10.1023/B:JOSE.0000021438.79877.58

Gorini et al. (2010), The Italian Strong Motion Network. Bull Earthq Eng, 8: 1075-1090. Guidoboni, E., G. Ferrari, D. Mariotti, A. Comastri, G. Tarabusi and G. Valensise, (2007).

CFTI4Med, Catalogue of Strong Earthquakes in Italy (461 B.C.-1997) and Mediterranean Area (760 B.C.-1500). INGV-SGA. http://storing.ingv.it/cfti4med/.

Graves R, Jordan TH, Callaghan S, Deelman E, Field E, Juve G, Kesselman C, Maechling P, Mehta G, Milner K, Okaya D, Small Pand K. Vahi, (2010), Cybershake: a physics-based seismic hazard model for southern California. *Pure and Appl Geophys* **168,** 367–381. doi:10.1007/s00024-010-0161-6.

Hanks, T. C., and H. Kanamori (1979), A moment magnitude scale, *J. Geophys. Res*., **84**(5), 2348–2350, doi:10.1029/JB084iB05p02348.

Haskell N. A. (1964), Total energy and energy spectral density of elastic wave radiation from propagating faults. *Bulletin of the Seismological Society of America*, **54** (6A): 1811–1841. doi: https://doi.org/.

Haskell N. A. (1966), Part II, A statistical source model, *Bull. deism, doc. Am*. **36**, 125-140.

Haskell N. A. (1969), Elastic displacements in the near field of a propagating fault. *Bulletin of the Seismological Society of America*, **59** (2): 865–908. doi: https://doi.org/.

Heaton, T.H., (1985), A model for a seismic computerized alert network, *Geology, Medicine*, doi:10.1126/science.228.4702.987.

Herrero A. and Bernard P (1994), A kinematic self-similar rupture process for earthquakes, *Bull. seism. Soc. Am.*, **84**, 1216-1228

Herrero, A., & Bernard, P. (1996). Modeling directivity of heterogeneous earthquake ruptures. *Bulletin of Seismological Society of America*, **86**(4), 1149–1160.

Hoshiba, M. (2013), Real-time prediction of ground motion by Kirchhoff-Fresnel boundary integral equation method: Extended front detection method for earthquake early warning. *Journal of Geophysical Research: Solid Earth*, **118**(3):1038-1050.

Hoshiba, M. and Aoki, S. (2015), Numerical shake prediction for earthquake early warning: Data assimilation, real-time shake mapping, and simulation of wave propagation. *Bulletin of the Seismological Society of America*, **105**(3):1324-1338.

Iervolino, I., Convertito, V., Giorgio, M., Manfredi, G., and A. Zollo, (2006), Real-time risk analysis for hybrid earthquake early warning systems. *Journal of Earthquake Engineering*, **10** (06), 867–885.

Imperatori W., and F. Gallovič (2017), Validation of 3D velocity models using earthquakes with shallow slip: Case study of the 2014 MwMw 6.0 South Napa, California, event, *Bull. Seismol. Soc. Am.* **107** (2), 1019-1026.

Joyner, W. B. and D. M. Boore (1981), Peak horizontal acceleration and velocity from strong-motion records including records from the 1979 Imperial Valley, California, earthquake, Bull. Seism. Soc. Am. 71, 2011-2038.

Kanamori, H. (2005), Real-time seismology and earthquake damage mitigation, *Annu. Rev. Earth Planet. Sci*., **33**, 195–214, doi: 10.1146/annurev.earth.33.092203.122626.

Kanamori, H., (1983), Global seismicity, in Earthquakes: Observation, Theory and Interpretation, Proceedings of International School of Physics "Enrico Fermi," course LXXXV, edited by H. Kanamori and E. Boschi, pp. 596-608, North-Holland, Amsterdam.

Kaneko, Y., and P. M. Shearer (2015), Variability of seismic source spectra, estimated stress drop, and radiated energy, derived from cohesive-zone models of symmetrical and asymmetrical circular and elliptical ruptures, *J. Geophys. Res. Solid Earth*, **120**, doi:10.1002/2014JB011642.

Kaneko, Y., and P. M. Shearer (2015), Variability of seismic source spectra,estimated stress drop, and radiatedenergy, derived from cohesive-zonemodels of symmetrical andasymmetrical circular and ellipticalruptures, *J. Geophys. Res.Solid Earth*,**120**, 1053–1079, doi:10.1002/2014JB011642

Keilis-Borok, V. I. (1959), On estimation of the displacement in an earthquake source and of source dimensions, *Ann. Geofis*. *(Rome)* **12**, 205-214.

Kilb, D. and J. Gomberg (1999), The initial subevent of the 1994 Northridge, California, earthquake: Is earthquake size predictable?. *Journal of Seismology* **3,** 409–420, https://doi.org/10.1023/A:1009890329925.

Koketsu, K., Miyake, H., Guo, Y., Kobayashi, H., Masuda, T., Davuluri, S., Bhattarai, M., Adhikari, L. B., and S. N. Sapkota (2016), Widespread ground motion distribution caused by rupture directivity during the 2015 Gorkha, Nepal earthquake, *Sci. Rep*., **6**, 28536, doi: 10.1038/srep28536.

Kuyuk, H. S., and R. M. Allen (2013), A global approach to provide magnitude estimates for earthquake early warning alerts, *Geophys. Res. Lett*., **40**, 6329–6333, doi:10.1002/ 2013GL058580.

Lee, S. J., K. F. Ma, and H. W. Chen (2006), Effect of fault geometry and slip style on near-fault static displacements caused by the 1999 Chi-Chi, Taiwan, Earthquake, *Earth Planet. Sci. Lett*., **241**, 336–350.

Chen P. and E. J. Lee (2015), Full-3D Seismic Waveform Inversion: Theory, Software and Practice, *Springer*, *Berlin*, p. 511.

Lockman, A. B., and R. M. Allen (2007), Magnitude-period scaling relations for Japan and the Pacific Northwest: Implications for earthquake early warning, *Bull. Seismol. Soc. Am.*, **97**(1B), 140– 150.

Lomax A., Virieux J., Volant P., and C. Berge-Thierry (2000), Probabilistic Earthquake Location in 3D and Layered Models. In: Thurber C.H., Rabinowitz N. (eds) Advances in Seismic Event Location. Modern Approaches in Geophysics, vol 18. *Springer*, Dordrecht.

Lomax, A. (2005), A reanalysis of the hypocentral location and related observations for the great 1906 California earthquake, *Bull. Seismol. Soc. Am.*, **95**, 861–877.

Lomax, A., S. Satriano and M. Vassallo, (2012), Automatic picker developments and optimization: FilterPicker - a robust, broadband picker for real-time seismic monitoring and earthquake early-warning, *Seism. Res. Lett.*, **83**, 531-540, doi: 10.1785/gssrl.83.3.531.

Luongo G., Carlino S., Cubellis E., Delizia I., Iannuzzi R. and F. Obrizzo, (2006), Il terremoto di Casamicciola del 1883: una ricostruzione mancata, Alfa Tipografia, Napoli, (in Italian).

Luzi, L., Pacor, F., Puglia, R., Lanzano, G., Felicetta, C., D'amico, M., Michelini, A, Faenza, L., Lauciani, V., Iervolino, I., Baltzopoulos, G., and E., Chioccarelli (2017) The Central Italy seismic sequence between August and December 2016: analysis of strong-motion observations, *Seismol Res Lett*, **88**(5):1219–1231.

Luzi, L., S. Hailemikael, D. Bindi, F. Pacor, F. Mele, F. Sabetta, (2008), ITACA (ITalianACcelerometric Archive): a web portal for the dissemination of Italian strong motion data. *Seismol Res Lett*. doi:10.1785/gssrl.79.5.

Madariaga, R. (1977), Implications of stress-drop models of earthquakes for the inversion of stress drop from seismic observations, *Pure Appl. Geophys*., **115**, 301-316, 1977.

Madariaga, R. (1976), Dynamics of an expanding circular fault, *Bull. Seismol. Soc. Am.*, **66**(3), 639–666.

Maeda T, Iwaki A, Morikawa N, Aoi S and H. Fujiwara (2016), Seismic-hazard analysis of long-period ground motion of megathrust earthquakes in the Nankai Trough based on 3d finite-difference simulation. *Seismol Res Lett*, **87**, 1265–1273. doi:10.1785/0220160093.

Mathews J. and K. Fenk, (2004), Numerical Methods Using MATLAB, 4e (https://www.mathworks.com/matlabcentral/fileexchange/4308-numerical-methods-using-matlab-4e).

Meletti, C., Visini, F., D'Amico, V., and A., Rovida (2016), Seismic hazard in central Italy and the 2016 Amatrice earthquake, *Annals of Geophysics*, **59**, doi: 10.4401/A G-7248.

Melgar, D., et al. (2015), Earthquake magnitude calculation without saturation from the scaling of peak ground displacement, *Geophys. Res. Lett*., **42**, 5197–5205, doi:10.1002/2015GL064278.

Minson S. E., Simons M. and J. L. Beck (2013), Bayesian inversion for finite fault earthquake source models I—theory and algorithm, *Geophysical Journal International*, **194** (3), 1701–1726, https://doi.org/10.1093/gji/ggt180.

Nakamura, Y. (1984), Development of the earthquake early-warning system for the Shinkansen, some recent earthquake engineering research and practical in Japan. The Japanese National Committee of the International Association for Earthquake Engineering, 224–238.

Nakamura, Y. (1988), On the urgent earthquake detection and alarm system (UrEDAS), in Proceedings of Ninth World Conference on Earthquake Engineering, Paper# 13-2-12, vol. VII, pp. 673–678, Tokyo-Kyoto, 2–9 Aug.

Nappi R., G. Alessio, G. Gaudiosi, R. Nave, E. Marotta, V. Siniscalchi, R. Civico, L. Pizzimenti, R. Peluso, P. Belviso, et al. (2018), The 21 August 2017 MD 4.0 Casamicciola earthquake: first evidence of coseismic normal surface faulting at the Ischia volcanic island, Seismol. Res. Lett., 89(4),1323-1334, 10.1785/0220180063.

Nazeri S., Colombelli S. and A. Zollo, (2019), Fast and accurate determination of earthquake moment, rupture length and stress release for the 2016–2017 Central Italy seismic sequence, *Geophysical Journal International*, **217**, 1425–1432, https://doi.org/10.1093/gji/ggz097

Nazeri, S. and Z. H. Shomali (2019), Rapid Estimation of the Epicentral Distance in the Earthquake Early Warning System around the Tehran Region, Iran. *Seismological Research Letters,* **90** (5): 1916–1922. doi: https://doi.org/10.1785/0220180375.

Nazeri, S., Shomali, Z. H., Colombelli, S., Elia, L., & Zollo, A. (2017), Magnitude Estimation Based on Integrated Amplitude and Frequency Content of the Initial P Wave in Earthquake Early Warning Applied to Tehran, Iran, *Bull. Seismol. Soc. Am.*, **107**, No. 3, doi: 10.1785/0120160380.

Ohnaka, M. A., (2000), Physical Scaling Relation Between the Size of an Earthquake and its Nucleation Zone Size. *Pure appl. geophys.* **157,** 2259–2282, https://doi.org/10.1007/PL00001084

Olson, E. L., and R. M. Allen (2005), The deterministic nature of earthquake rupture, *Nature*, **438**, 212– 215.

Pacor, F., R. Paolucci, L. Luzi, F. Sabetta, A. Spinelli, A. Gorini, M. Nicoletti, S. Marcucci, L. Filippi, and M. Dolce (2011), Overview of the Italian strong motion database ITACA 1.0, *Bull Earthquake Eng*, **9**(6), 1723–1739, doi:10.1007/s10518-011-9327-6.

Pacor, F., Spallarossa, D., Oth, A., Luzi, L., Puglia, R., Cantore, L., Mercuri, A., D'Amico, M., and D. Bindi (2016), Spectral models for ground motion prediction in the L'Aquila region (central Italy): Evidence for stress-drop dependence on magnitude and depth, *Geophys. J. Int*., **204**(2), 697–718, doi:10.1093/gji/ggv448.

Piatanesi, A., A. Cirella, P. Spudich, and M. Cocco (2007), A global search inversion for earthquake kinematic rupturehistory: Application to the 2000 western Tottori, Japan earthquake, *J. Geophys. Res.*,**112**, B07314, doi:10.1029/2006JB004821.

Picozzi, M., (2012), An attempt of real-time structural response assessment by an interferometric approach: a tailor-made earthquake early warning for buildings. *Soil Dynamics and Earthquake Engineering*, **38**, 109–118. doi: 10.1016/j.soildyn.2012.02.003.

Picozzi, M., A. Zollo, P. Brondi, S. Colombelli, L. Elia, and C. Martino (2015), Exploring the feasibility of a nationwide earthquake early warning system in Italy. *J. Geophys. Res. Solid Earth*, **120**, 2446–2465. doi: 10.1002/2014JB011669.

Picozzi, M., D. Bindi, P. Brondi, D. Di Giacomo, S. Parolai, and A. Zollo (2017), Rapid determination of P wave-based energy magnitude: In-sights on source parameter scaling of the 2016 central Italy earthquake sequence, *Geophys. Res. Lett*., **44**, doi: 10.1002/2017GL073228.

Pizzi, A., Di Domenica, A., Gallovič, F., Luzi, L., and R. Puglia, (2017). Faultsegmentation as constraint to theoccurrence of the main shocks of the 2016 Central Italy seismic sequence, *Tectonics*, **36**, 2370–2387, https://doi.org/10.1002/2017TC004652

Rydelek, P., C. Wu, and S. Horiuchi (2007), Comment on "Earthquake magnitude estimation from peak amplitudes of very early seismic signals on strong motion records" by Aldo Zollo, Maria Lancieri, and Stefan Nielsen, *Geophys. Res. Lett*., **34**, L20302, doi:10.1029/2007GL029387.

Sato, T., and T. Hirasawa (1973), Body wave spectra from propagating shear cracks, *J. Phys. Earth*, **21**, 415–431.

Satriano, C., Elia L., Martino C., Lancieri M., Zollo A. and G. Iannaccone (2011), PRESTo, the earthquake early warning system for Southern Italy: concepts, capabilities and future perspectives. *Soil Dyn. Earthq. Eng*, **31** (2), 137–153, doi: 10.1016/j.soildyn.2010.06.008.

Satriano, C., Lomax, A., & Zollo, A. (2008), Real-Time Evolutionary Earthquake Location for Seismic Early Warning, *Bull. Seismol. Soc. Am.,* **98**, 1482–1494, doi: 10.1785/0120060159.

Sbrana, A., Fulignati, P., Marianelli, P., Boyce, A. J., and A. Cecchetti, (2009), Exhumation of an active magmatic–hydrothermal system in a resurgent caldera environment: The example of Ischia (Italy). *Journal of the Geological Society*, 166, 1061–1073. doi:10.1144/ 0016-76492009-030

Scala, A., Festa, G., and S. Del Gaudio (2018), Relation between near-faultground motion impulsive signals andsource parameters. *Journal of Geophysical Research: Solid Earth,***123**, 7707–7721. https://doi.org/10.1029/2018JB015635

Schwartz, L. (1966), *Théory des distributions*, Herman, Paris.

Schwartz, L., (1966), Theorie des Distributions, Hermann, Paris.

SeisComP. Seismological Communication Processor, (2016), https://www.seiscomp3.org (last accessed January 2016).

Sen, M. K., and P. L. Stoffa, (1995), Global Optimization Methods in Geophysical Inversion, 281 pp., *Elsevier Sci*., New York.

Shearer, J.M. (1999), *Introduction to seismology*, Cambridge university press, Cambridge, pp 260.

Somerville, P.G., N.F. Smith, R.W. Graves, and N.A. Abrahamson (1997), Modification of empirical strong ground motion attenuation relations to include the amplitude and duration effects of rupture directivity, *Seismological Research Letters,* **68**, 199-222.

Song S.G. and P. Somerville (2010), Physics-based earthquake source characterization and modeling with geostatistics, *Bull. seism. Soc. Am*., **100,** 482-496.

Stankiewicz, J., Bindi, D., Oth, A., Pittore, M. and S. Parolai, (2015), The Use of Spectral Content to Improve Earthquake Early Warning Systems in Central Asia: Case Study of Bishkek, Kyrgyzstan. *Bulletin of the Seismological Society of America*, **105**, 5, p. 2764- 2773.

Steacy S. J. and J. McCloskey (1998), What controls an earthquake's size? Results from a heterogeneous cellular automaton, *Geophysical Journal International*, **133**, F11–F14, https://doi.org/10.1046/j.1365-246X.1998.1331548.x.

Strauss A. J. and R. M. Allen (2016), Benefits and Costs of Earthquake Early Warning. *Seismological Research Letters*; **87** (3): 765–772. doi: https://doi.org/10.1785/0220150149

Supino M., Gaetano F. and A. Zollo, (2019), A probabilistic method for the estimation of earthquake source parameters from spectral inversion: application to the 2016–2017 Central Italy seismic sequence, *Geophysical Journal International*, **218** (2), 988–1007, https://doi.org/10.1093/gji/ggz206.

Tape C., Liu Q., Maggi A. and J. Tromp, (2009), Adjoint tomography of the southern California crust, *Science*, **325**, 988–992.

Tarantino S., Colombelli S., Emolo A. and Aldo Zollo (2019), Quick Determination of the Earthquake Focal Mechanism from the Azimuthal Variation of the Initial *P*-Wave Amplitude. *Seismological Research Letters,* **90** (4): 1642–1649. doi: https://doi.org/10.1785/0220180290.

Teng T., Wu L., Shin T., Tsai Y., W. H. K. Lee (1997), One minute after: Strong-motion map, effective epicenter, and effective magnitude. *Bulletin of the Seismological Society of America,* **87** (5): 1209–1219. doi: https://doi.org/.

Wald, D. J., V. Quitoriano, T.H. Heaton, and H. Kanamori (1999), Relationships between Peak Ground Acceleration, Peak Ground Velocity and Modified Mercalli Intensity in California, *Earthquake Spectra*, **15**, 557-564.

Wells D. L. and K. J. Coppersmith (1994), New empirical relationships among magnitude, rupture length, rupture width, rupture area, and surface displacement. *Bulletin of the Seismological Society of America,* **84** (4): 974–1002. doi: https://doi.org/.

Wolfe, C. J. (2006), On the properties of predominant-period estimators for earthquake early warning, *Bull. Seismol. Soc. Am.*, **96**(5), 1961–1965.

Wu, Y. M., Shin, T. C. and Y. B. Tsai (1998), Quick and reliable determination of magnitude for seismic early warning. *Bull. Seism. Soc. Am.*, 88, 1254-1259.

Wu, Y. M. and T. L. Teng, (2002), A virtual sub-network approach to earthquake early warning. *Bull. Seism. Soc. Am*, **92**, 2008–2018.

Wu, Y. M., and H. Kanamori (2005), Rapid assessment of damaging potential of earthquakes in Taiwan from the beginning of P waves, *Bull. Seismol. Soc. Am.*, **95**, 1181–1185.

Wu, Y. M., and L. Zhao (2006), Magnitude estimation using the first three seconds P-wave amplitude in earthquake early warning, *Geophys. Res. Lett.*, **33**, L16312, doi:10.1029/2006GL026871.

Wu, Y. M., H. Y. Yen, L. Zhao, B. S. Huang, and W. T. Liang (2006), Magnitude determination using initial P waves: A single-station approach. *Geophys. Res. Lett*., **33,** L05306, doi: 10.1029/2005GL025395.

Wu, Y.M. and H. Kanamori (2008), Development of an earthquake early warning system using real-time strong motion signals, Sensors 8, 1-9.

Wurman, G., R. M. Allen, and P. Lombard (2007), Toward earthquake early warning in northern California, *J. Geophys. Res*., **112**, B08311, doi: 10.1029/2006JB004830.

Xu., G., Xu., C., Wen, Y., and G., Jiang (2017), Source Parameters of the 2016–2017 Central Italy Earthquake Sequence from the Sentinel-1, ALOS-2 and GPS Data, *remote sensing*, **9**, 1182, doi: 10.3390/rs9111182.

Yamamoto, S., Noda, S., & Korenaga, M. (2012), An estimation method of epicentral distance based on characteristics of P-wave initial envelope, *RTRI Report*, **26**, 5-10 (inJapanease).

Ziv, A. (2014), New frequency-based real-time magnitude proxy for earthquake early warning, *Geophys. Res. Lett*., **41**, 7035–7040.

Zollo, A., (2018), Seismology, Short-Course, 18th Iranian Geophysical Conference, Tehran, Iran.

Zollo, A., A. Orefice, and V. Convertito (2014), Source parameter scaling and radiation efficiency of microearthquakes along the Irpinia fault zone in southern Apennines, Italy, *J. Geophys. Res. Solid Earth*, **119**, 3256–3275, doi:10.1002/2013JB010116.

Zollo, A., and A. Emolo, (2011), A., Terremoti e onde. Metodi e pratica della sismologia moderna, Liguori, Italy, (in Italian).

Zollo, A., et al. (2009), Earthquake early warning system in southern Italy: Methodologies and performance evaluation, *Geophys. Res. Lett*., **36**, L00B07, doi:10.1029/2008GL03668.

Zollo, A., et al. (2012), An integrated regional and on-site Earthquake Early Warning System for Southern Italy: concepts, methodologies and performances, in “Early Warning for Geological Disasters - Scientific Methods and Current Practice”, *Springer*, ISBN: 978-3-642-12232-3, 2014, doi: 10.1007/978-3-642-12233-0.

Zollo, A., Lancieri, M., and S., Nielsen (2006), Earthquake magnitude estimation from peak amplitudes of very early seismic signals on strong motion records, *Geophys. Res. Lett.* **33**, L23312, doi: 10.1029/2006GL027795.

Zollo, A., Lancieri, M., and S., Nielsen (2007), Reply to comment by P. Rydelek et al. on ‘‘Earthquake magnitude estimation from peak amplitudes of very early seismic signals on strong motion records’’, *Geophys. Res. Lett.*, **34**, L20303, doi:10.1029/2007GL030560.

Zollo, A., O. Amoroso, M. Lancieri, Y. M. Wu, and H. Kanamori (2010), A threshold-based earthquake early warning using dense accelerometer networks, *Geophys. J. Int.*, **183**, 963–974.

Zollo, A., S. Colombelli, L. Elia, A. Emolo, G. Festa, G. Iannaccone, C. Martino, and P. Gasparini (2014), An integrated regional and on-site Earthquake Early Warning System for Southern Italy: Concepts, methodologies and performances, in Early Warning for Geological Disasters Scientific Methods and Current Practices, edited by F. Wenzel and J. Zschau, pp. 117–137, *Springer*, Berlin.